Title	Accurate patient dosimetry in modern computed tomography systems
Author(s)	Albngali, Ahmad
Publication Date	2020-10-21
Publisher	NUI Galway
Item record	http://hdl.handle.net/10379/16225

Accurate patient dosimetry in modern computed tomography systems

A THESIS

Submitted by

AHMAD ALBNGALI

in partial fulfilment of the requirements for the degree of

DOCTOR OF PHILOSOPHY

Medical Physics Research Cluster

School of Physics

College of Science

National University of Ireland Galway

Academic Supervisor:

Dr. Niall Colgan

Prof. Andy Shearer

October 2019

Table of Contents

Declaration of Authorship

I, Ahmad Albngali, declare that this thesis titled, "Accurate patient dosimetry in modern computed tomography systems" and the work presented in it are my own, and that appropriate credit has been given to the work of others. The work in this thesis has not been submitted elsewhere for any other degree or qualification.

Signed: **Ahmad Albngali**

Date: 1 / 8 /2020

NATIONAL UNIVERSITY OF IRELAND GALWAY

Abstract

School of Physics

College of Science

Doctor of Philosophy

by AHMAD ALBNGALI

The most common parameter used to estimate and minimise patient dose in computed tomography (CT) is the CT dose index (CTDI). The CTDI is the average absorbed dose from a series of contiguous irradiations along the long axis. However, it has limitations. For instance, the 14-cm length of the body CTDI phantom does not provide a sufficiently long scatter path relative to the typical length of a human torso; hence, the patient dose may be underestimated depending on imaging parameters. The American Association of Physicists in Medicine (AAPM) task group 111 proposed the new method Equilibrium Dose (D_{Eq}) to estimate the dose from the CT scanner by using a small volume ionization chamber positioned in a phantom long

enough to establish dose equilibrium at the location of the chamber. In this thesis, a novel phantom was designed and validated using three separate anatomical clinical sequences (head, chest and abdomen), and the equilibrium dose was determined and compared to CTDI dose estimations using a standard pencil chamber. This methodology allowed measurement of the accumulated dose for any clinical scan length and measurement of the equilibrium dose. In addition, D_{Eq} and conventional CTDI methods were used to estimated organ dose values, and the output was compared with human phantom embedded the thermoluminescent dosimeter (TLD). Furthermore, the annual reported CTDI volumes of 20 patients were corrected to D_{Eq}, and the effective organ dose was estimated. In conclusion, the thesis demonstrates the D_{Eq} method provides a closer approximation of dose in modern clinical CT systems, and the CTDI method underestimates dose .

Acknowledgements

and specifically for me to continue my PhD study. They are a great inspiration to me.

I thank my family to the whole I own a great deal. To my sister Afnan and my brother Mohammed, thank you for everything, you were always there when I need you. Thanks for all my relative and my friends who always supported me.

Finally, I would like to thank my lovely wife, Rawdah. Thank you for being so kind, patient, loving and understanding. You carried me when I could barely stand, and I honestly don't know where I would be without you. To my angel, my princes, my daughter, Malak, it was always good to see your lovely smile after a long day at the university. Thanks to my son Abdul and my daughter Menna who I wish were still here to see me, but I am sure that they can see me from up there.

Dissemination of Research

Publication

Ahmad Albngali, Andy Shearer, Wil van der Putten, Brendan Tuohy, Niall Colgan. CT output dose performance-conventional approach Versus the dose equilibrium method. Int J Med Phys Clin Eng Radiat Oncol. 2018;7(1):15-26. (*journal paper, published*)

Ahmad Albngali, Andy Shearer, Margaret Moore, Brendan Tuohy, Niall Colgan. Comparison of the Dixon and CTDI dose quantification techniques. Phys Med. IAPM 2016,Volume 42, October 2017.(*published*)

Ahmad Albngali, Andy Shearer, Wil Van Der Putten, Brendan Tuohy, Niall Colgan. Does CTDI provide an accurate measure of CT dose and what are the implications for organ dose estimation. IAPM Making Waves, Summer 2019.(*published*)

Ahmad Albngali, Joshua Deslongchamps, James Blackwell, Andy Shearer, Brendan Tuohy, Niall Colgan. Comparison of planer dose equilibrium and computed tomography dose index and implications for reported patient dose information.OJMI.2019 (journal paper, *published*)

Communication

Ahmad Albngali, Andy Shearer, Margaret Moore, Brendan Tuohy, Niall Colgan. Comparison of the Dixon and CTDI dose quantification techniques. 6th postgraduate research day 2016, NUI Galway. (*poster presentation*)

Ahmad Albngali, Andy Shearer, Margaret Moore, Brendan Tuohy, Niall Colgan. Adult thoracic and abdominopelvic CT: Does equilibrium assessment provide more sensitive organ dose estimation than conventional CTDI?. World congress on medical physics and biomedical engineering, June 3-8, 2018, Prague, Czech republic. (*poster presentation*)

Ahmad Albngali, Andy Shearer, Brendan Tuohy, Niall Colgan. AAPM TG 111 dose estimation method compared to CTDI and clinical implication. Special interest groups workshop in ionisation imaging, IAPM workshop on CT. (*oral presentation*)

Ahmad Albngali, Andy Shearer, Margaret Moore, Brendan Tuohy, Niall Colgan. Dose equilibrium and CTDI quality assurance in CT and the implications for the effective dose estimation in patients. IAPM 2019, Annual Scientific Meeting. (*poster presentation*)

Awards

Award a full academic scholarship to study abroad from the ministry of higher education in Saudi Arabia in 2014.

List of Figures

List of Tables

Abbreviations

ART   Algebraic Reconstruction Technique

SIRT   Simultaneous Iterative Reconstruction Technique

ILST   Iterative Least Squares Technique

CTDI   Computed Tomography Dose Index

CI   Couch Increment

ST   Slice Thickness

MSAD   Multislice Average Dose

$CTDI_{100}$ Computed Tomography Dose Index 100

$CTDI_{w}$ Computed Tomography Dose Index Weighted

CTDvol   Computed Tomography Dose Index Volume

DLP   Dose Length Product

D_{Eq} Dose Equilibrium

TLD   Thermoluminescent Dosimeter

PMMA   Poly(methyl methacrylate)

D(0)   Accumulated Dose

D_{Eq} Planer Average Equilibrium Dose

FDA   Food and Drug Administration

AAPM   American Association of Physicists in Medicine

ICRP   International Commission on Radiological Protection

NRPB   National Radiological Protection Board

IAEA   International Atomic Energy Agency

$D_{Eq.air}$ Dose Equilibrium Free in Air

$CTDI_{air}$ Computed Tomography Dose Index Free in Air

WT   Tissue Weighting Factors

Chapter 1

1.1 Introduction

Exposure to ionizing radiation from medical treatments and other activities using radioactive materials can increase the risk of cancer and pass mutations to offspring. For this reason, radiation exposure is monitored and controlled[1].

Medical X-ray examinations are common sources of human-made radiation exposure. To control the exposure, both the system design and the use must be considered.

According to the National Council on Radiation Protection & Management (NCRP), there has been a 72 % increase on average in the radiation doses in the US over the past 30 years. Much of the increase is due to more extensive use of computed tomography (CT) scans [2,3].
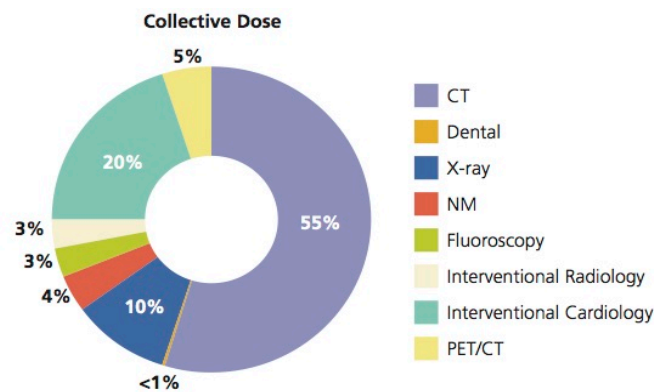
Figure 1. 1: Distribution of collective dose from diagnostic medical imaging in Ireland 2009–2012 [4]

In Ireland, a study by the Radiological Protection Institute found that artificial sources such as medical ionizing radiation were the greatest contributors to exposure, particularly diagnostic X rays above 90%; moreover, one of the largest contributors to the collective dose is CT, which

contributes up to 55%, as shown in figure1.1[4].

This increase is likely due to the capabilities of modern CT scanners. Therefore, it is necessary to take advantage of dosimetry tools and other metrics that would provide accurate CT dose estimations and use them to guide medical practice.

However, these CT dose estimations are dependent on the specific objective of the medical procedure being used. Both deterministic effects, which are tissue reactions, and stochastic effects must be considered. Examples of deterministic effects are erythema or disruption of implanted devices like pacemakers. At the same time, evaluating stochastic effects may require different procedures than when evaluating deterministic effects. For example, stochastic effects of radiation are usually measured in internal organs, while deterministic effects are usually measured in the skin or lens of the eye [3].

Furthermore, CT dosimetry procedures are affected by morphology, weight and height of the patient, such as adults of different genders, and paediatric patients, due to their smaller size, growing tissues, and longevity.

The main aims of patient dosimetry for CT used in medical imaging are the establishment, use and assessment of guidance levels or diagnostic reference levels and the measurement of the dosimetric parameters of the equipment performance. Furthermore, the accurate determination of individual radiation dose to the patient in CT allows a better estimate of the procedural risk.

1.2 Problem Description (Beyond CTDI)

The current method of CT dosimetry is based on the computed tomography dose index (CTDI) concept, which represents a single rotation of the x-ray source. Typically CTDI is applied to represent absorbed dose along an axis of a cylindrical phantom. It is measured with a 100 mm long pencil ionization chamber (CTDI100) placed in a cylindrical Polymethyl methacrylate (PMMA) phantom representing the head and body.

Even though CTDI is used to represent CT dosimetry, many believe the CTDI index is not an accurate patient dosimetry metric [5,6].

Many improvements in CT technology have been implemented since the introduction of CTDI, including new and better clinical procedures and widespread use of CT. These improvements encompass new methods of operation that did not originally rely on CTDI, e.g., helical scanning and cone-beam irradiation geometries. CTDI is designed for axial scanning; therefore, using it to characterise dose in helical scanning is outside its scope. Furthermore, wider longitudinal (z)-axis collimations and scanning lengths can limit the appropriateness of $CTDI_{100}$ parameters representing CT dose [7].

Moreover, using a 100mm pencil chamber produces a significant error in the dose profiles because radiation scattered beyond the relatively short (100-mm) range of integration along the z-axis is excluded, which then underestimates the cumulative dose at z = 0 (Figure 1. 2) [8,9]. This error is mostly the result of over-beaming in multi slice CT when the z-axis collimation of the source radiation is broadened to produce uniform umbra incidence across the detectors (Figure 1. 3).

The resulting underestimation occurs with both narrow and wide beams and slowly becomes larger with increases in the z-axis collimation width [8].

In addition, the phantoms used for CTDI measurements are shorter than an adult torso and so do not produce as much scattered radiation as would occur in a typical adult. This means that the average dose (e.g., MSAD) that would occur in the much longer typical-sized adult torso is underestimated with CTDI measurements in the 14 cm-long body CTDI phantom.

With the prevalence of both multi-slice CT scanners and wider collimated beams, CTDI has come under increasing scrutiny as to whether it can properly reflect patient doses in CT [6].
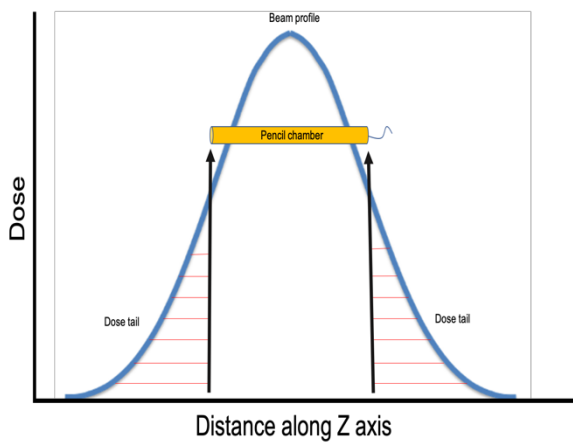
Figure 1. 2: Diagram of profile beam with pencil ion chamber
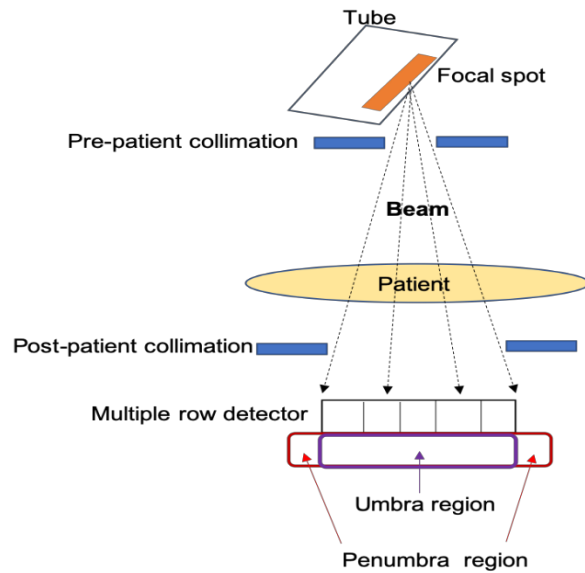
Figure 1. 3: Diagram of umbra and penumbra region

1.3 Aim and Structure of the Thesis

Currently CT dosimetry uses a single slice profile with a 10 cm long ion chamber (CTDI100); however, this method may not be adequate as the measurement underestimates the equilibrium dose and dose line integral. While it is possible to make the ion chamber longer so as to collect the broad scatter tails, a better alternative to the current method could utilise a small volume ion chamber and scan a length of phantom long enough to establish dose equilibrium at the location of the chamber. Modern CT scanners can cover a scan length in 15 seconds or less using helical or axial series; therefore, this method is not more time consuming in practice than using a long chamber. Moreover, this alternative method was proposed in the American Association of Physicists in Medicine (AAPM) TG111 report[10].

The aim of the current research is to determine the implementation, robustness and versatility of this proposed alternative method (the equilibrium dose method) by estimating accumulative dose and organ dose for patients from CT scanning based on the AAPM TG111 report [10].

The current research is organised in such a manner so that Chapter 2 and Chapter 3 provide a summary of the theoretical background of the CT scanner, covering the development of CT, the principles of CT scanning, image reconstruction and patient dose, with particular emphasis on key concepts of CTDI. In addition, an explanation of how the equilibrium dose method can be used to measure the absorbed dose is discussed.

Chapter 4 describes construction and characterization of a novel phantom based on the AAPM TG 111 report[10]. The chapter further describes measurement of the accumulated dose and the planar average equilibrium dose (D_{Eq}) using a Farmer chamber as well as the dose estimation of the current CTDI standard and D_{Eq}, as independently verified with TLD measurements.

The work in Chapter 5 uses the D_{Eq} and CTDI methods to estimate organ dose values indirectly

and uses the Alderson Rando phantom embedded with TLD to directly estimate organ dose. Both indirect methods are compared against the direct method.

In Chapter 6, The D_{Eq} correction based on the Toshiba system output of CTDI is retrospectively applied to an anonymous patient group for radiation effective dose estimations. Twenty patient recordings of CTDI are corrected with D_{Eq} estimates over the course of the measured dose to determine the possible effect that variations in dose measurement may have on individual patient effective dose measurements.

Chapter 7 summarises the work carried out in this thesis and discusses future work.

Chapter 2

CT Acquisition Background Theories

Chapter 2 describes the background theories of CT acquisition as they pertain to CT dosimetry. The initial focus is on describing the X-ray beam spectrum that provides the means of attenuation measurement, followed by the measurement process and image reconstruction method. Chapter 3 will then elaborate on the patient dose with a focus on the main concepts of CTDI. Additionally, the chapter will further explain the AAPM TG111 method used to measure absorbed dose.

2.1 Design of computed tomography scanner

A CT scanner is made of a gantry, a computer and an operating console, all of which have various subcomponents. The gantry, which is the largest, comprises the patient equipment including the patient support, positioning couch, mechanical supports and scanner housing as well as the x-ray tube generator and x-ray detectors.

2.2 Production of x-rays
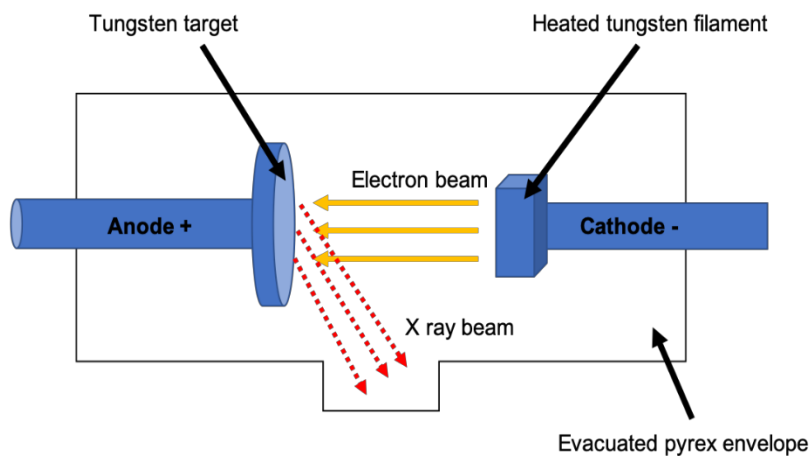
Figure 2. 1: Diagram of the simple X-ray tube

An x-ray tube is a high vacuum glass envelope. A negative cathode (e-) and a positive anode (e+) are sealed in the tube at opposite ends. The cathode is a filament made of tungsten, which undergoes thermionic emission when heated, i.e., it emits electrons. A thick copper rod with a small tungsten target on its end comprises the anode. Electrons are emitted from the cathode and travel at high velocities to strike the anode target when high voltage is applied [11].

When the tube current (mA) increases, the filament temperature increases, which produces more electrons. Fractions of a second are used to measure the time in which x-rays leave the x-ray tube. The number of x-rays produced by the anode depends on the electrons available and the time period set for their release. Therefore, the product of the mAs and time determines the number of x-rays produced.

The anode is designed so the x-rays are directed down toward the film through a window in the metal x-ray tube housing.

2.3 X-ray production at the anode

Several interactions can occur between the electrons and the target atoms to produce x-ray photons, i.e.,

- Outer shell interaction: low energy (Electromagnetic) released and quickly converted into heat energy

- Inner shell interaction: produces characteristic radiation

- Nucleus field interaction: Bremsstrahlung

2.3.1 Characteristic radiation
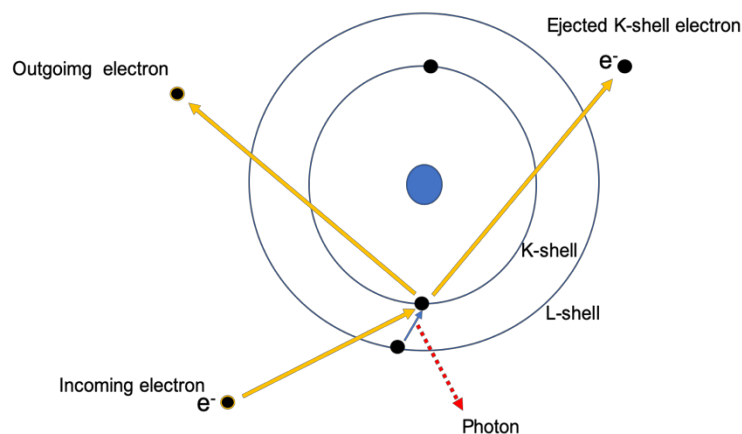
Figure 2. 2: Formation of characteristic radiation

If an electron travelling at high speed collides with an electron in the K-shell and has more energy than that which binds the K-shell electron, a 'hole' will be left in the K-shell as its electron will be ejected. Electrons from the outer shells, e.g., from the L-shell or M-shell, will move into the K-shell hole and emit a single x-ray photon, which is known as characteristic radiation. Its energy level is equal to the difference in energy between the outer and inner shell electrons participating in process [12].

2.3.2 Bremsstrahlung
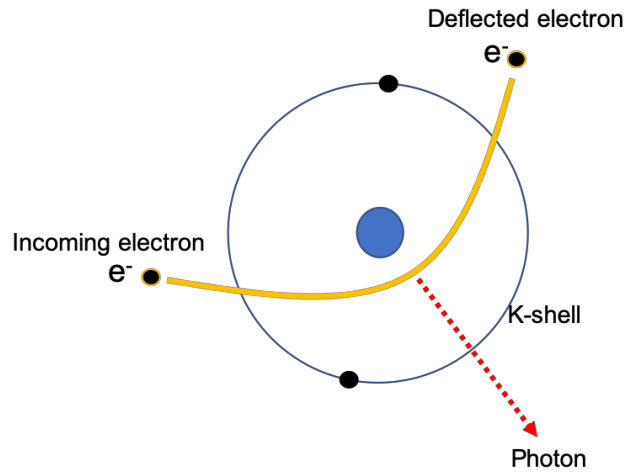
Figure 2. 3: Formation of bremsstrahung

A bremsstrahlung interaction occurs when a high-speed electron and a nucleus collide. As it nears the nucleus, the electron may be deflected due to Coulomb forces and lose energy as bremsstrahlung radiation [11].

2.4 X-ray interaction with matter

2.4.1 Photoelectric effect
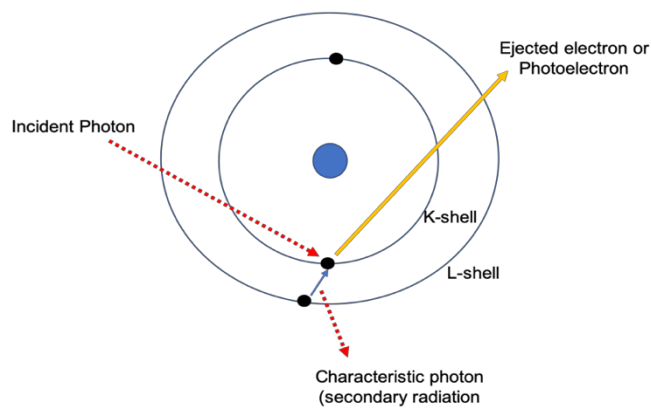
Figure 2. 4: Formation of the photoelectric effect

When photons interact with matter causing electrons to be rejected due to absorption of the x-ray photon, which is known as photoelectric (PE) absorption, it is referred to as the PE effect. The PE effect thus ionizes (i.e., charges) the atom, which can then lose this charge when emitting an x-ray. PE absorption primarily occurs up to energies of approximately 500 KeV and for atoms with high atomic numbers.

The photoelectric effect not only produces characteristic x-rays in the x-ray tube, but also is important to consider when x-rays interact with matter. An x-ray photon transfers its energy to an orbital electron, which is then dislodged and exits the atom at high speed. Kinetic energy is produced when an x-ray photon transfers energy to an orbital electron, which then leaves the atom under high velocity [13]. This kinetic energy is determined as:

$$KE = hv - (BE) \qquad (2.1)$$

where KE is the kinetic energy of the photoelectron, hv is the energy of the incident X-ray photon and BE is the energy required to remove the electron.

2.4.2 Compton Effect
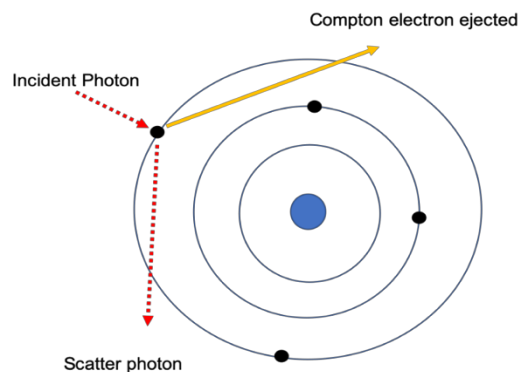
Figure 2. 5: Formation of the Compton effect

The Compton effect, also referred to as Compton scattering (C) or incoherent scattering, takes place if an x-ray photon causes an electron to be released by an atom while a lower energy x-ray photon is scattered. In this process, energy and momentum are conserved. At the same time, because the x-ray photon that is scattered has less energy, it exhibits a longer wavelength than the originating photon. Elements with low atomic numbers largely experience the Compton effect; moreover, when energies are 100 keV, it is the Compton effect that produces radiation absorption.

Even if x-ray energy is relatively low, the Compton effect will be produced when using targets of low atomic weight. During the process, photons are scattered by atomic electrons. During Compton scattering, the incident X-ray will change direction and transmit energy to an electron, thus referred to as a Compton electron. A Compton electron continues the process by interacting with subsequent atoms, which results in secondary ionization. As the electrons are low energy, the resulting x-rays will also be low energy.

The maximum possible energy, E, of a Compton electron (recoil electron) is equal to:

$$E = h v / 1 + 4\, h v \qquad (2.2)$$

where hv is the energy of the incident photon. Qualitatively, it is easy to see that the Compton electrons will be significantly less energetic than photoelectrons for an equal value of hv[13].

2.4.3 Coherent Effect
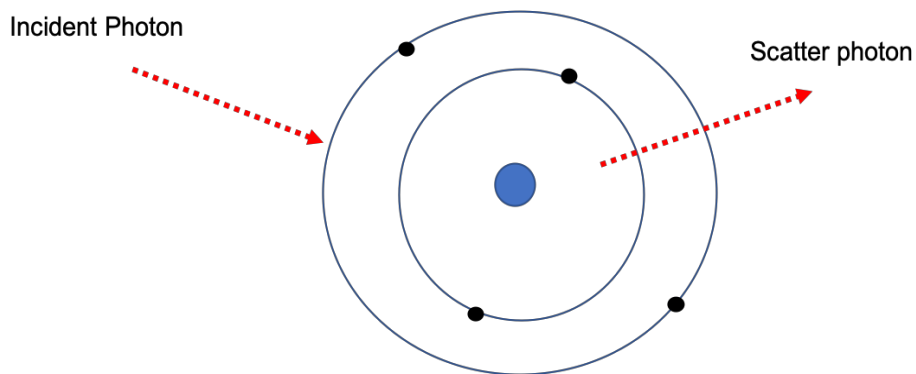
Figure 2. 6: Formation of the coherent effect

In coherent scattering, or classical scattering, a photon interacts with an atom's orbital electron and changes direction. As the photon has low energy, usually less than 10 keV, it will not likely remove the orbital electron from its shell. The atom will instead absorb the photon energy, which excites the atom, and energy, equal to the incident photon, is then released in a different direction, producing a scatter photon. Most scatter photons, due to their low energy, are absorbed in the body and contribute little to the image while adding slightly to patient dose. [13]

2.4.4 Conclusion

The most common types of CT interactions at CT energies are the Compton effect and the photoelectric effect. These effects are important to consider when using CT scanners as they influence how photons are absorbed by anatomical structures. A greater number of Compton and photoelectric effects are produced in hard tissues as compared to soft tissues; therefore, more photons depart from the patient when passing through soft tissues. This characteristic

then allows for imaging of both hard and soft tissues.

2.5 Principle of computed tomographic imaging

The early generation of CT imaging devices scanned a narrow x-ray beam across the patient simultaneously with a radiation detector on the opposite side. For a monoenergetic beam, the transmission through the patient is determined by the Lambert-Beer law ($I = I_0 \, e^{-\mu x}$), with the patient represented as a homogeneous medium, as shown in Figure 2.7.
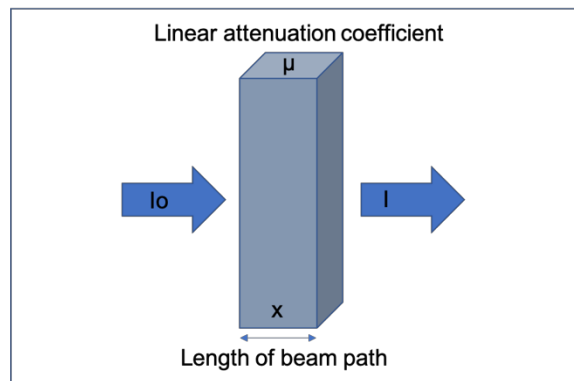
Figure 2. 7: CT X-ray measured for a homogeneous object.

When an x-ray beam is intercepted by two regions having attenuation coefficients $\mu1$ and $\mu2$ and thicknesses x1 and x2, as shown in Figure 2.8, the x-ray transmission is determined as:

$$I = I_0 \, e^{-(\mu1x1+\mu2x2)} \qquad (2.3)$$
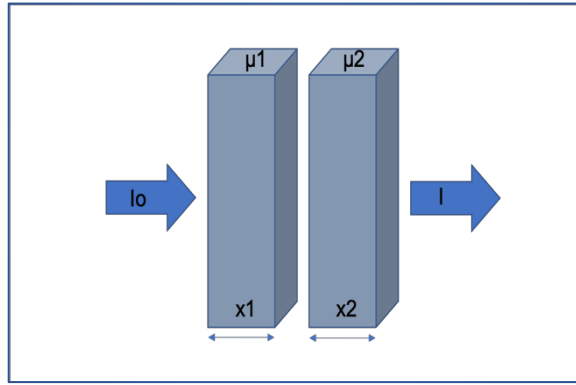
Figure 2. 8: CT X-ray measured for an inhomogeneous object.

When there are many (n) regions having different linear attenuation coefficients along the path of x-rays, the transmission is determined as :

$$I = I_0 \, e^{-\sum_{i=1}^{n} \mu_i x_i} \qquad\qquad (2.4)$$

$$-\sum_{i=1}^{n} \mu_i x_i = (\mu_1 x_1 + \mu_2 x_2 + \cdots + \mu_n x_n) \qquad\qquad (2.5)$$

where I/I0 is

$$e^{-\sum_{i=1}^{n} \mu_i x_i} \qquad\qquad (2.6)$$

 In a single transmission measurement, it is not possible to determine separate attenuation coefficients as too many unknown values of μ_i exist in the equation. On the other hand, when multiple transmission measurements are taken in the same plane but with different x-ray source and detector angles, the coefficients can be separated, yielding a cross-sectional display of attenuation coefficients. A gray-scale image can be produced by assigning gray levels for the various attenuation coefficient ranges, which then represent patient structures with different x-ray attenuation characteristics.

After readings from the detector are stored in the computer, the tube is moved to another angle for a new projection profile. Once a complete rotation is performed, the patient's table is moved a small distance for the next slice measurement.[14] Using data from profiles through all voxels in a slice for sufficient numbers of projections, one can then calculate the average linear attenuation coefficient for each voxel, which is called reconstruction. Each μ value is assigned a grey scale value on the display monitor and is presented in a pixel of the image [14].
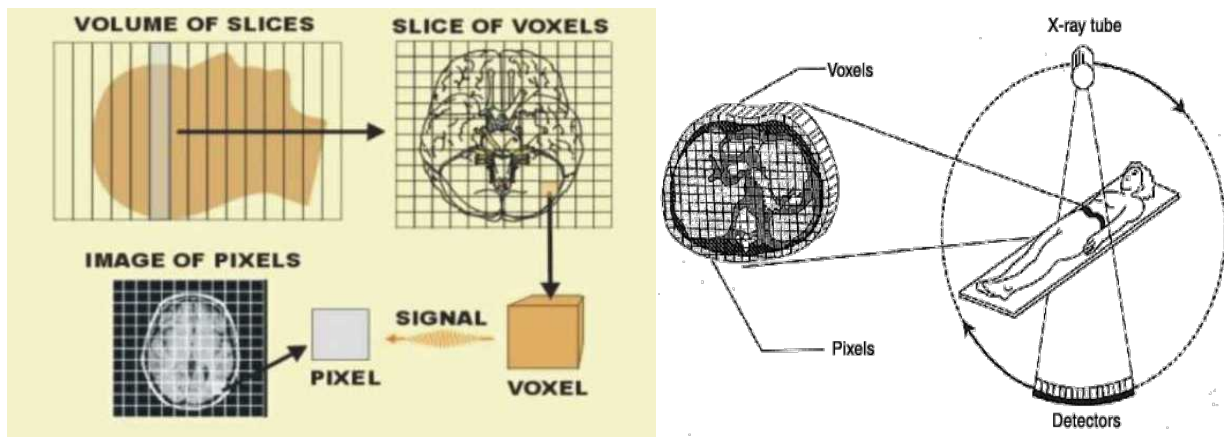
Figure 2. 9: Stages of the formation of the computed tomography image [15,16]

Figure 2.9 shows the formation of the computed tomography image. Typically, an anatomical region is divided into slices. The slices are divided into a matrix (array) of tissue voxels (volume elements). The digital image of the slice is formed as a matrix of pixels (picture elements). The brightness of colour displayed in each pixel represents some physical characteristic of the tissue in the voxel.

2.6 Image reconstruction

Four approaches, known as CT reconstruction algorithms, are used to calculate the slice image based on its views.

The first method is not practical but provides an understanding of the concept. It solves many linear equations simultaneously using one each measurement. In this approach, a certain sample in a certain profile is the sum of a certain group of image pixels [17]. However, this method of CT reconstruction is too time consuming to be feasible as it has to solve hundreds of thousands of linear equations simultaneously.

The second method of CT reconstruction employs iterative techniques to produce the final image. Variations of these techniques are the Algebraic Reconstruction Technique (ART), the Simultaneous Iterative Reconstruction Technique (SIRT) and the Iterative Least Squares Technique (ILST). They differ by the correction methods they use which are ray by ray, pixel by pixel or the entire data set, respectively [17].

A third method is filtered back projection, which is an advanced variation of simple back projection.
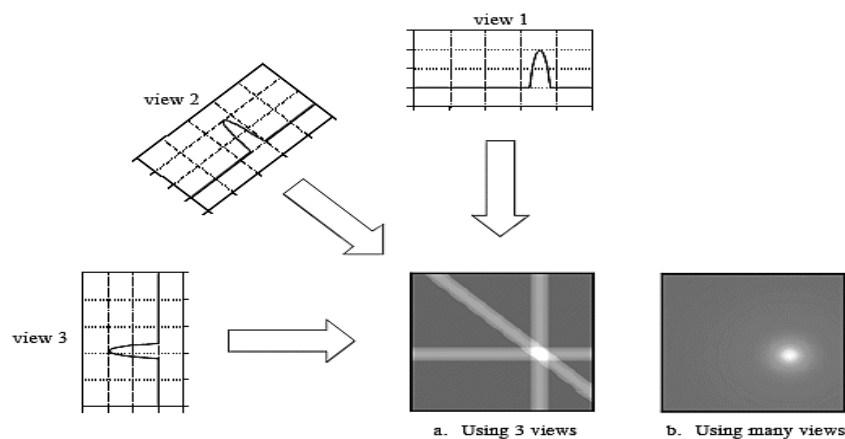
Figure 2. 10: Back projection reconstructs an image[18]

by taking each view and smearing it along the path it was originally acquired. The resulting image is blurry of the correct image.

 Simple back projection is logical but not highly technical. As shown in figuren2.10, a sample is back projected when all the pixels are sent a ray pointing to the same value of the sample. In other words, a back projection is formed when each view travels back through the image in its

original direction [17,19]. For a given image, the reconstructed density is the sum of all ray projections that pass through it. For this reason, back projection is sometimes referred to as the summation method or the method of linear superposition. The mathematical equation describing the back projection is:

$$\hat{f}(x,y) = \sum_j p(x \cos \phi_j + y \sin \phi_j, \phi_j) \Delta\phi_j \quad (2.7)$$

where the integral of $\hat{f}(x,y)$ along the ray is called the ray sum or ray projection p and where the summation extends over all projection angles (ϕ_j). The method ($x \cos \phi_j + y \sin \phi_j$) selects only those rays that pass through the point (x,y), while the ($\Delta\phi_j$) factor represents the angular distance between adjacent projections [14]. Even though back projection is a simple concept, it does not adequately solve the problem as the image is very blurry.
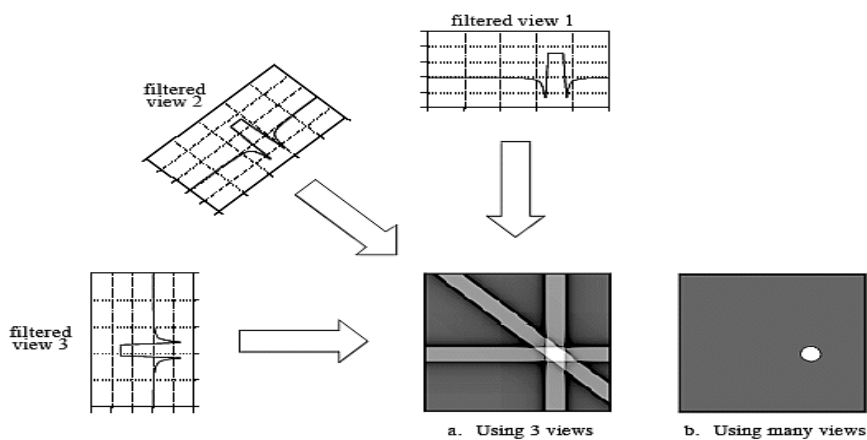
Figure 2. 11: Filtered back projection reconstructs an image[18]

Filtering each view before back projection removes the blurring and results in a mathematically exact reconstruction of the image.

Filtered back projection is preferred as it corrects the blurring produced when using simple back projection. As shown in Figure 2.11, each view is filtered before back projection, which eliminates blurring. The filter involves convolving each one-dimensional view using a one-dimensional filter kernel. The filtered views are then back projected to reconstruct the image,

which is close to the "correct" image, especially when using an infinite number of views and points per view. The method was first developed by Bracewell and Riddle [20], who derived the formula:

$$p^*(x') = k_m\, p(x') - \int_{-R}^{R} p(x'') \frac{\sin^2\left(\pi k_m(x'-x'')\right)}{\pi^2(x'-x'')^2} dx'' \qquad (2.8)$$

where $p(x')$ is the measured profile, $p^*(x')$ is the modified profile, p^* is the projection p after being filtered, R is the maximum radius of the object and km is the greatest spatial frequency (wavenumber) present in the projection [19].

The fourth method is called Fourier reconstruction. In this method, any function of space or time can be represented as a sum of sine and cosine waves (harmonics) of different frequencies, and the amplitude of each harmonic is called the Fourier coefficient. This means any two-dimensional density function f(x,y) can be expressed as a sum of sine and cosine waves. The amplitudes of the sinusoidal waves are denoted by the Fourier coefficients [17,19].

The basis of Fourier reconstruction is that the Fourier coefficients of the image are related to the Fourier coefficients of the projections [14]. In fact, the amplitudes of waves propagating at an angle are simply equal to the Fourier coefficients of the projection at the same angle. The Fourier coefficients of the image can easily be obtained from those of the projections, and the picture can be resynthesized.

2.7 Iterative reconstruction
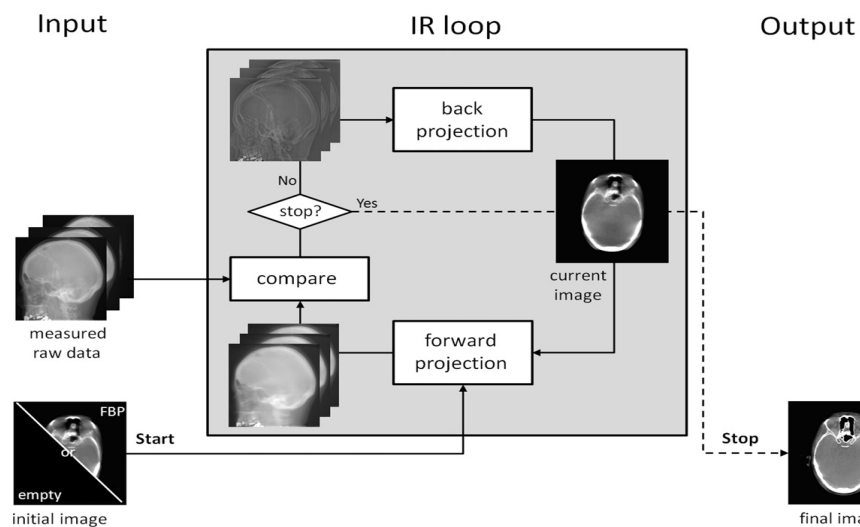
Figure 2. 12: Schematic view of the iterative reconstruction process[21]

Iterative reconstruction methods include three steps that are repeated, as shown in Figure 2.12.

In the first step, a forward projection of the volumetric object estimate produces artificial raw data. Next, the artificial and actual raw data are compared to compute an updated image. Lastly, the correction term is back projected onto the volumetric object estimate. The volume estimate begins with either an empty image or with prior information, along with an filtered back projection reconstruction. The process is complete when a fixed number of iterations is reached, the update is considered small enough or a predefined quality is met [22].

Three different techniques of iterative reconstruction, which differ according to the sequence used for corrections, include ART, SIRT and ILST.

ART, one of the simplest forms of iterative reconstruction, was used for image reconstruction in the first CT systems. It is based on Kaczmarz' method [23] of solving linear equations:

Ax= b

where x is the voxels of the volume to be reconstructed, A is the system matrix used to produce raw data and b are the measured raw data pixels. Matrix A corresponds to rays from the source through the volume to the detector pixels; for example, the line integral of the linear attenuation coefficient [24,25].

In ILST, all projections are calculated at the beginning of the iteration, and all corrections are made simultaneously. However, this leads to an overcorrection as each cell is recorrected for every ray passing through it, causing the iterations to oscillate about the correct solution.[26]

SIRT has each iteration beginning with a particular point, which is corrected for all rays that pass through it. Other points are then treated the same, except that corrections made during the iteration are embodied in succeeding calculations [27].

2.8 Development of computed tomography scanning

CT scanners were introduced in 1971 and have gone through several generations of design since that time. These include:

- Translate-rotate, pencil beam and one detector (first generation)
- Translate-rotate, fan beam and multiple detectors (second generation)
- Rotate-rotate (third generation)
- Rotate-fixed (fourth generation)

The primary reason to introduce a new configuration is to reduce the scan time, which is generally accomplished by reducing or simplifying the movement of the system. For example, the first two generations had a stop-start motion, but more recent versions use continuous rotation.

2.8.1 First generation
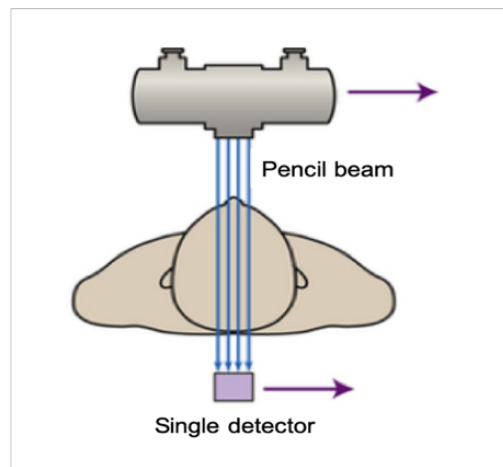
Figure 2. 13: First generation of computed tomography[28]

Early CT scanners had a translate-rotate system and used a pencil beam, which was a single x-ray beam based on parallel beam geometry. They used pinhole collimators to produce single x-ray beams to scan patients.

These units also operated with only a single detector placed opposite the x-ray tube. In this manner, the single detector measured the amount that passed through the patient for a certain slice of a body part. As multiple slices were required, the x-ray tube and detectors had to be moved and then the x-ray tube had to be rotated to obtain images from different angles [29].

The primary shortcoming of first-generation CT scanners was the extended time needed to acquire the data and reconstruct the computerized images. For example, producing five images to examine the head took about 25 to 30 minutes.

2.8.2 Second generation
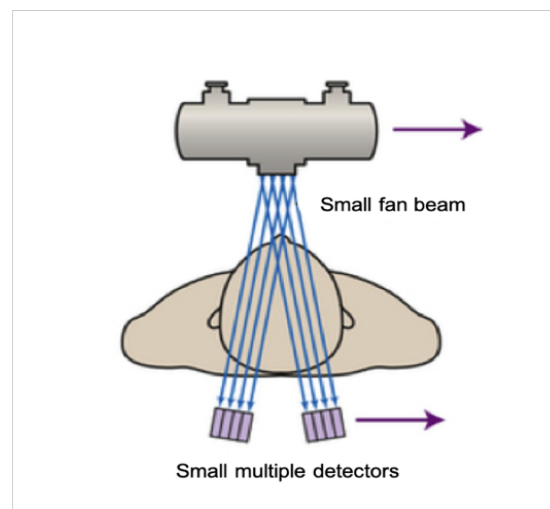
Figure 2. 14: Second generation of computed tomography[28]

Second generation CT scanners used a narrow fan x-ray beam at an angle of about 10 degrees along with a linear array of 30 detectors. This arrangement provided a significant decrease in acquisition time from that of the first generation. Even though the fan beam angle was small and still required linear movement of the x-ray tube and detectors, the level of linear displacement needed was substantially reduced. For example, the acquisition time needed for a head scan dropped by two to three minutes per slice. As a result, the second-generation CT scanners were fifteen times faster than the first generation, which was quite an improvement[30].

However, even though the acquisition time improved for the second generation, the measuring field was still small. These CT scanners still relied on rotation and translation of the x-ray tube and detectors, which added wasted time to the imaging protocol [29].

2.8.3 Third generation
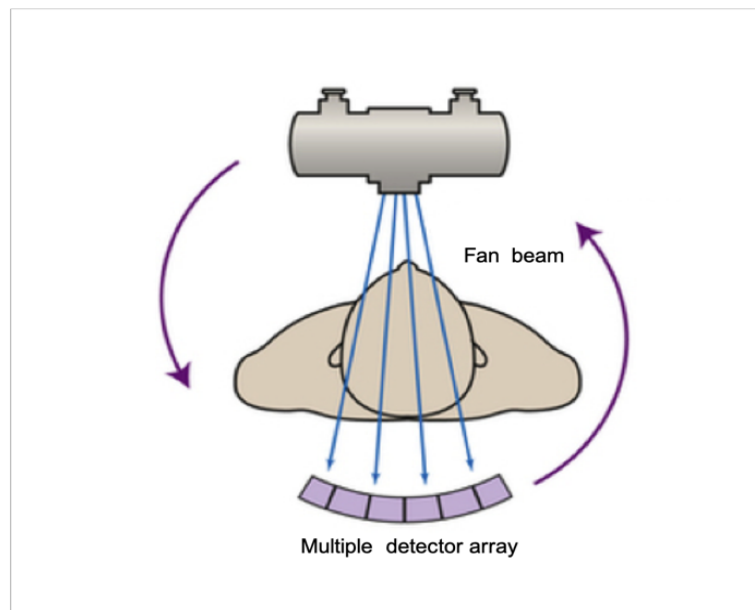
Figure 2. 15: Third generation of computed tomography[28]

Third-generation CT scanners use a wide aperture fan beam, allowing the entire patient to be scanned at one time. This design enabled the x-ray tube and detectors to freely rotate through the projection angles with no need to stop and collect multiple slices per angle [30].

Moreover, the third-generation scanners use an angle from 40 to 60 degrees, which further requires a linear detector array consisting of 400 to 1000 detectors. To synchronise the x-ray tube and the detector rotations, they are joined together, which produces faster acquisition time[30].

The primary advantage of third-generation CT scanners is once again diminishing the time it takes to complete a scan, with some systems producing scans in less than five seconds per projection angle. Third-generation CT scanners are still in use, with most operating at scan times at a fraction of a second. However, they do have a drawback as they produce a characteristic ring artifact due to the number of detectors and their common lack of calibration.

2.8.4 Fourth generation
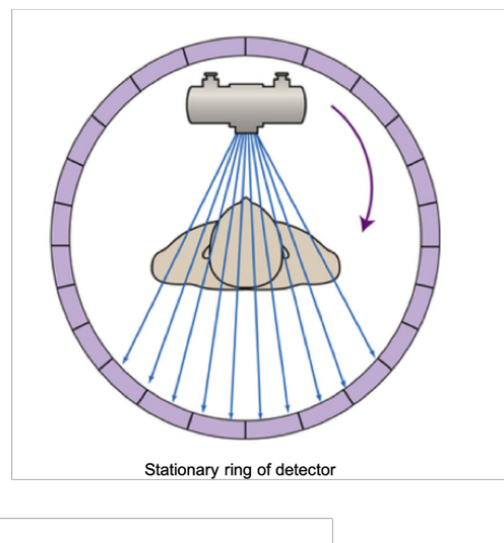
Figure 2. 16: Fourth generation of computed tomography[28]

Fourth-generation scanners use detectors formed into a ring encircling the patient. Instead of the detectors moving, the x-ray tube rotates inside the detector ring, with the x-ray beam collimated to form a fan. Some fourth-generation models use more than 2000 detectors. Exposed detectors are read when the x-ray tube is at the prescribed angles. Projections are commonly taken at over 1000 angles during the x-ray tube rotation. In this way, one CT scan is comprised of many projections, each at a slightly different angle, which is an advantage of this type of continuous-on x-ray design.

Third-generation and fourth-generation CT scanners both provide excellent results, with neither having an obvious advantage over the other. A fan beam and multiple detectors produce speed as they can collect data faster than can a single detector; however, a major disadvantage of a fan beam is an increase in scattered radiation. As CT is usually performed at 120 kVp, Compton scattering is common. Even though the Compton reaction is almost identical for pencil beam and fan beam scanners, scattered photons are more apt to be detected when using a fan beam. Figure 2.17 illustrates a comparison between the two types of scanners.
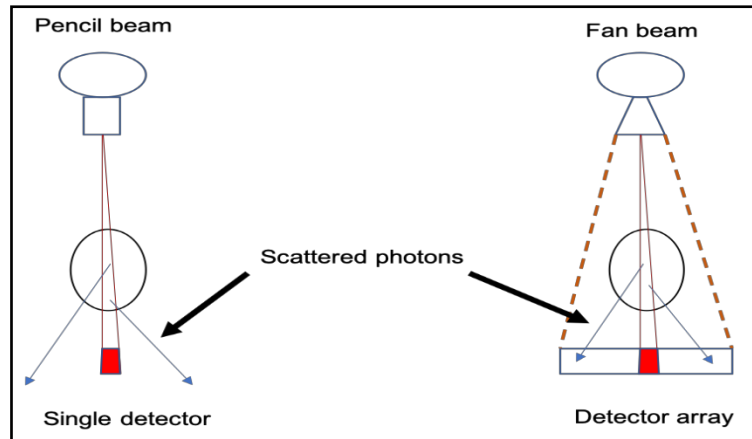
Figure 2. 17: Diagram of the scatter radiation between fan beam and pencil beam

In Figure 2.17, two scattered photons are generated by the pencil beam, but both miss the detector and go unrecognized. On the other hand, with the fan beam scanner, two scattered photons, generated from the same volume of tissue, strike a detector and are recorded as an artefact (noise).

2.9 Spiral computed tomography scanning
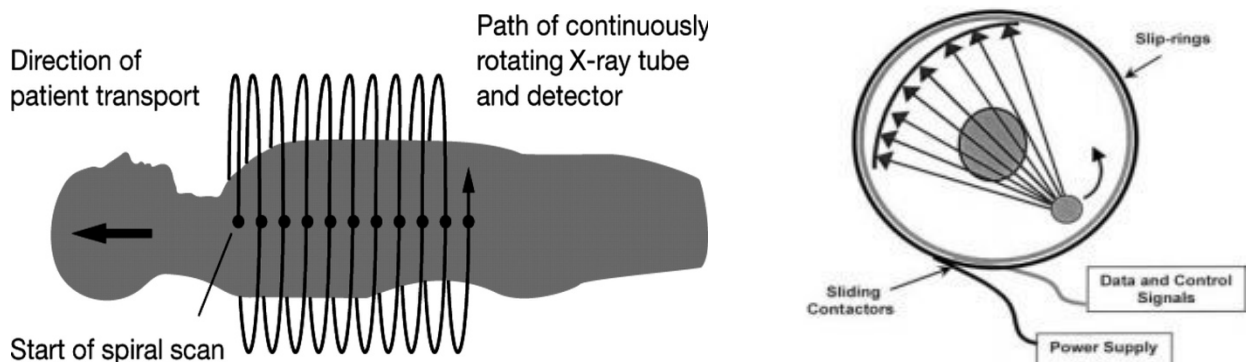
Figure 2. 18: Principle of spiral computed tomography scanning[31]

Most third- and fourth generation CT scanning utilises spiral CT scanning, which was first introduced in 1989. Image acquisition time is reduced as the tube voltage cables are connected by a sliding contact called a slip ring that is supported by the rotating gantry. This setup allows the x-ray tube to rotate in a spiral pattern while the patient continuously moves through the gantry. As a result, the spiral CT technique can reduce patient motion and increase patient throughput [32]. At the same time, more of the patient may be scanned during contrast media passage, which can reduce the volume of contrast needed. Moreover, as there is greater continuity of data along the patient axis, the three-dimensional reconstruction is improved [33].

Pitch is defined as the patient couch movement per rotation divided by the slice thickness for single-slice CT scanning; however, while in multislice CT, the patient couch movement per rotation is divided by the beam width. Low pitch, which can be achieved by small increments of couch movement, improves spatial resolution along the patient's long axis; however, this results in increased patient doses and imaging times. When the pitch is greater than unity, the patient dose is less, but data must be interpolated to preserve resolution along the long axis [34].

Older scanners providing spiral computed tomography may be problematic as the continuous tube operation requires a lower radiation dose per rotation, often producing a significant increase in image noise. However, modern scanners have improved tube technology, which eliminates this problem.

Even though scan duration is shorter with spiral computed tomography, more sections must be processed, which may increase the time needed for image reconstruction. This increase is especially noted when overlapping sections are used for imaging. However, new scanners have resolved this issue as they yield rapid reconstruction, often at a rate of just one second per image. If an increased number of images need processing, this may also increase time [34].

2.10 Focal Spot

The point where the electron beam strikes the tube anode, causing x-rays to be emitted, is the focal spot. Its size and shape are determined by the size and shape of the electron beam as it strikes.

Furthermore, the size and shape of the electron beam are determined by:

- The tungsten filament coil dimensions
- The focusing cup construction
- The filament position in the focusing cup
- The electric field that exists between the cathode and anode: the focal spot enlarges when the current increases due to the repulsion of adjacent electrons, known as the blooming effect.

Conventional CT x-ray tubes often include both small and large focal spots. The small spot provides more detail and improves geometric sharpness by narrowing the penumbra of the x-ray beams on the detectors (Figure 2. 19). Therefore, a small focal spot is used when spatial resolution is important. On the other hand, a large focal spot is used when a short exposure time is important [35,36].
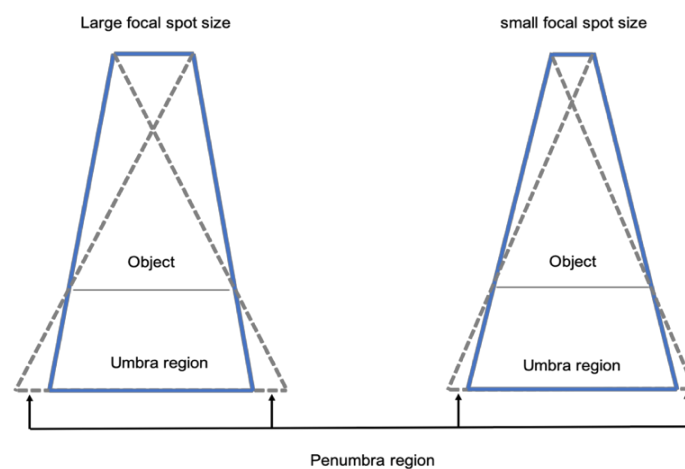
Figure 2. 19: Diagram illustrates the effects of focal spot size on the penumbra

The small focal spot use is limited on most current CT scanners as thermal damage to the anode within the conventional x-ray tube occurs when producing high-resolution images over long distances. Moreover, a small focal spot size limits the number of photons detected, which increases the noise. However, newer models are equipped with advanced x-ray tube cooling systems to prevent overheating. At the same time, a bigger generator coupled with the cooling system allows more photons to be detected when using the small focal spot [36,37].

2.11 Collimation, umbra and penumbra regions
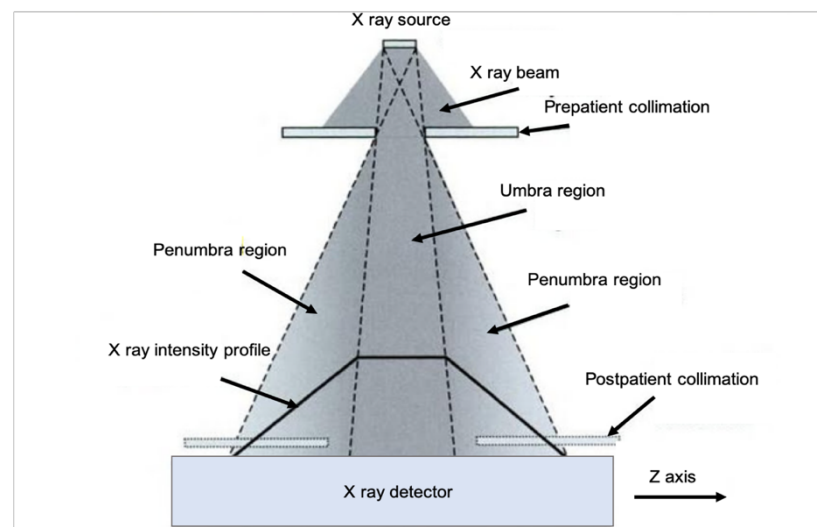
Figure 2. 20: Illustration of prepatient – postpatient collimation and umbra – penumbra regions[38]

CT collimation is used to (1) reduce unnecessary patient radiation, and (2) provide good image quality. There are two types of collimators, pre-patient and post-patient. A pre-patient collimator is placed between the x-ray source and the patient. Since x-ray photons emitted cover a wide range along the z-axis, the pre-patient collimator restricts the beam to a narrow

region of the patient, as shown in Figure 2.20. When using a single slice CT, the collimator reduces the patient dose and defines the slice thickness of the imaging plane. However, when using a multi-slice CT, the slice thickness is defined by the detector aperture.

Due to geometric limitations, after passing through the pre-patient collimator, the x-ray beam has both an umbra region, and a penumbra region along the z-axis. Moreover, the x-ray beam is homogeneous in the umbra region because the source is not blocked by the collimator at any point: the entire x-ray focal spot can be seen anywhere inside the region. On the other hand, the penumbra is a nonhomogeneous region as the x-ray focal spot is always partially blocked by the collimator.

In single slice CT, the slice thickness is based on the full width at half maximum (FWHM) and the full width at one-tenth maximum (FWTM) of the complete umbra and penumbra region. In multislice CT, the sizes of the umbra and penumbra relative to each other are important in the scanner dose utilization. Most commercial multi-slice CT scanners use just the umbra to formulate CT images as that is where the active detector cells are located. The penumbra represents the unused patient dose. Therefore, the dose efficiency can be improved by reducing unused x-ray photons.

The second type of collimator is post patient, which is used to reject scattered photons. It is located in front of the detector and focuses on the x-ray source. The scattered radiation usually deviates from the original photon trajectory, and post patient collimation blocks them from striking the detector [38].

2.12 Filters

X-ray photons cover a wide spectrum, including many low energy rays that are mainly absorbed by the patient rather than contributing to the detected signal. Removing these low energy x-rays reduces the patient dose, which can be achieved through the use of filters [38].

Two commonly used filters are the flat filter and the bowtie filter. The flat filter, usually composed of aluminium or copper, is placed between the x-ray source and the patient, thereby uniformly modifying the spectrum across the field of view.

 However, a patient cross-section is generally oval in shape, so some systems use a bowtie filter to reduce the beam intensity inside the field of view, which then reduces the dose to the patient, as shown in Figure 2.21.
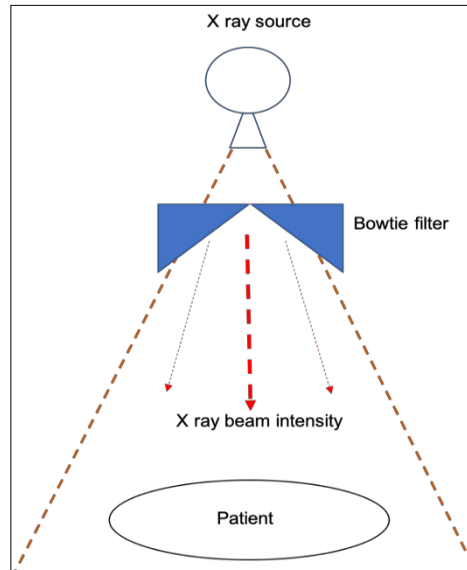
Figure 2. 21: Illustration of a bowtie filter

2.13 CT scan detectors

The latest generations of CT radiation detectors are much improved as compared to earlier models. Detector dose efficiency, comprised of three parameters, determines maximum tube loading and controls the patient dose. One is capture efficiency, which is based on the detectors receiving photons and is controlled by the size of the detectors as well as the distance between them. The second is absorption efficiency, which is based on the detectors converting incoming photons and is determined by the materials used as well as the detector size and thickness. The third is conversion efficiency, which is based on how well the detector converts the photon information to a digital signal.

Additionally, CT detectors should be highly stable, respond quickly and exhibit a wide dynamic range [39]. Two types of detectors are used. The gas filled detectors contain pressurized xenon to improve detection efficiency, while solid state detectors include NaI (T1), CaF, and CsI scintillation crystals; ceramic materials made of rare-earth oxides as well as bismuth germanate (BGO) and cadmium tungstate [Cd WO4].

The solid state detectors cannot be tightly packed but exhibit almost 100% detection efficiency, while gas filled detectors can be tightly packed with fewer interspace septa. Solid state detectors can receive primary beams from a moving tube; however, gas filled detectors are highly directional, which does not provide efficient reception of primary beams [39].

Multiple detector arrays are found in the latest generation of CT scanners. They allow multi-slice CT (MSCT), which provides advantages over single slice CT (SSCT). The MSCT scanners not only have multiple rows of detectors, but they also have a wider x-ray beam in the z-axis, allowing the beam to function more effectively. In this setup, data can be collected for more than one slice simultaneously [40].

The main difference between SSCT and MSCT is the detector arrays (Figure 2.22). SSCT uses detectors that form a one-dimensional array, while MSCT is divided into several smaller detectors along the z-axis, forming a two-dimensional array. The CT scanners currently used in hospitals have at least 64 rows of detectors that provide a very high resolution [40].
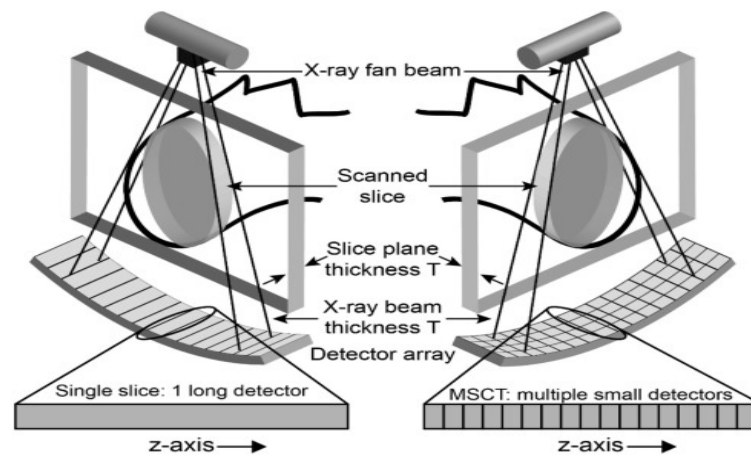
Figure 2. 22: Single slice CT (left) versus multiple slice CT (right)[41]

2.14 Quality assurance and quality control

CT-scan quality assurance aims to assure safe and accurate operation of the entire CT scanning process. Quality assurance protocol should include tests that will assure an accurate target, critical structure localization and accurate placement of treatment beams for a volumetric CT scan. Specifically, quality assurance tests should include [42,43]:

- Physical parameter measurements of the radiation generators and imaging devices when commissioned and periodically through their service.

- Verification of the appropriate physical and clinical factors for patient diagnosis or therapy.

- Procedures and result records, including outlines of the individual QC tests, performed.

- Verification of calibration and conditions of operation for dosimetry and monitoring equipment.

Several electronic components and a significant amount of data processing are needed to produce a CT image. Imaging system problems are hard to detect merely by observing an image as a gap exists between data acquisition and image display. Due to the system's complexity, prospective monitoring and testing of its components is the only way to assure image quality.

For overall system performance with standard phantoms, measurements should be correlated with patient dose, so variables that affect contrast, spatial resolution, image noise and patient radiation dose are properly balanced.

Fundamental system performance indicators are CT number, resolution, noise and patient dose. The CT number accuracy is measured by scanning a water-filled phantom at least once a month. The CT number for water over a 20 cm diameter phantom should be zero, with a variation of less than 1. Deviation from the expected CT number can be adjusted by applying a correction factor for the pixel value. Value constancy should be monitored daily [39,44].

Measurement of physical and mechanical factors such as couch positioning and indexing should be part of a comprehensive quality control program. Hard-copy device and system monitor performance should be checked for distortion, brightness and contrast adjustment. Image analysis features such as distance and bone density measurements should be independently evaluated [39,44].

Chapter 3

3.1 Patient dose

The radiation dose from a CT scan is higher than that used for an equivalent Xray radiographic image. For the head, a CT image requires a dose of about 10 to 20 mGy, while an abdominal CT image requires a dose of about 30 to 50 mGy. To improve the contrast and spatial resolution, these doses would have to be increased significantly. The relationship between dose and resolution can be determined as [44]:

$$D = a\left(\frac{s^2}{e^3 b}\right) \qquad (3.1)$$

where D is the patient dose, s is the signal/noise ratio, e is the spatial resolution, b is the slice thickness and a is a constant [44].

The CTDI is the patient dose in multislice CT. When the couch increment (CI) is equal to the slice thickness (ST), the CTDI equals the multislice average dose (MSAD). When the couch increment is lower than the slice thickness, the MSAD is the CTDI multiplied by the ratio of the slice thickness to the couch increment; that is

$$MSAD = CTDI\left[\frac{ST}{CI}\right] \qquad (3.2)$$

Outside the slice, patient dose significantly decreases. A conservative rule of thumb estimates the dose at 1% of the in-slice dose at a distance of 10 cm from the slice [44].

3.2 Computed Tomography Dose Index (CTDI)

CTDI is the average absorbed dose from a series of contiguous irradiations along the long axis. It is measured from one axial CT scan and is determined by dividing the integrated absorbed dose by the nominal total beam collimation.

It represents the primary dose measurement in CT:

$$\text{CTDI} = \frac{1}{NT} \int_{-\infty}^{\infty} D(Z) dz \qquad (3.3)$$

where $D(Z)$ is the radiation dose profile along the z-axis, N the number of tomographic sections imaged in a single axial scan and T the number of data channels used in a particular scan.

3.2.1 Computed Tomography Dose Index 100

The CTDI was proposed and established in the late 1970s by the US Food and Drug Administration (FDA). It is measured using a PMMA cylinders15 cm long with diameters of 16 and 32 cm, representing a standard head and body section, respectively. The cylinder has one central and four peripheral bore holes used to insert a 100 mm long ionization chamber [45].

It is determined as:

$$\text{CTDI}_{100} = \frac{1}{NT} \int_{-50mm}^{50mm} D(Z) dz \qquad (3.4)$$

where N is the number of slices, T the slice thickness and $D(Z)$ the dose profile along the z-axis of rotation.

The pencil chamber length (L) is not really measuring exposure (X) or air kerma, but instead

the integral of the single rotation dose profile D(z). The exposure meter may convert the charge collected into an apparent exposure reading in roentgens (R) or air kerma, expressed in milligray (mGy); however, the meter reading actually represents average exposure or air kerma over L, as:

$$\text{Meter reading} = \frac{1}{l}\int_{-l/2}^{l/2} X(z)dz = \frac{1}{fl}\int_{-l/2}^{l/2} D(z)dz \tag{3.5}$$

where f is the f-factor (exposure to dose conversion factor, $D = f \cdot X$).

Considering the above definition of CTDI 100 (L = 100 mm),

 it is clear that

$$\text{CTDI} = \frac{f\left(\frac{mGy}{mGy}\right).100mm \,.\, \text{meter reading(mGy)}}{NT(mm)} \tag{3.6}$$

Thus,

$$\text{CTDI}_{100}(mGy) = \frac{C \,.\, f\left(\frac{mGy}{mGy}\right).100mm \,.\, \text{meter reading(mGy)}}{NT(mm)} \tag{3.7}$$

where C is the unit less the chamber calibration factor (typically near 1.0) [45] .

3.2.2 Computed Tomography Dose Index weighted

The Weighted CTDI (CTDI$_w$) is the average CTDI across the field of view (FOV):

$$\text{CTDI}_W = \frac{1}{3}\text{CTDI}_{100,CENTER} + \frac{2}{3}\text{CTDI}_{100,EDGE} \tag{3.8}$$

where the values of 1/3 and 2/3 represent the approximate relative areas of the center and edge values, respectively [46]. $CTDI_w$ can be used to represent scanner radiation output for a specific kVp and mAs.

3.2.3 Computed Tomography Dose Index volume

To represent a dose for a specific series of scans, protocol requires taking into account any gaps or overlaps between the x-ray beams. This can be done with a dose descriptor called the Volume CTDI (CTD_{vol}):

$$CTDI_{vol} = \frac{NT}{I} \cdot CTDI_W \qquad (3.9)$$

where I is the table increment per axial scan

Pitch is defined as the ratio of table travel per rotation (I) to the total nominal beam width (N x T)

so:

$$Pitch = \frac{I}{NT} \qquad (3.10)$$

thus, (CTDI $_{vol}$) can be expressed as:

$$CTDI_{vol} = \frac{1}{Pitch} \cdot CTDI_W \qquad (3.11)$$

where $CTDI_w$ represents the average absorbed radiation dose over the x and y directions from a series of axial scans and $CTDI_{vol}$ represents the average absorbed radiation dose over the x,

y and z directions.

3.2.4 Dose Length Product (DLP)

To improve the representation of the overall energy delivered by a scan protocol, the absorbed dose can be integrated along the scan length to compute the Dose Length Product (DLP) [47]:

$$DLP \ (mGy.\,cm) = CTDI_{vol} \ . \ Scan \ Length \qquad (3.12)$$

Therefore, dose length product (DLP) is obtained by multiplying the $CTDI_{vol}$ by the scan length.

The DLP does not provide a dose value as is evident from its unit (mGy.cm). However, it is useful because it serves as a surrogate for patient dose, especially when comparing dose levels; moreover, it can establish diagnostic reference levels (DRL).

Both $CTDI_{vol}$ in mGy and DLP in mGy.cm can only provide rough estimates of the patient dose levels involved as they are determined for cylindrical phantoms, which do not match the patient situation well [46].

3.3 A new look at CT dose measurement

Dixon[9] conducted a study to analyze the limitations of the CTDI method for dose measurement and suggested a new method involving a small ionization chamber for dose accumulation. The researcher suggested the small ion chamber has higher efficacy than a conventional long

chamber for dose measurement. To produce the collected dose distributions, some equations were derived for helical computed tomography scanning. The dose line integral was evaluated using these equations in a cylindrical dosimetry phantom. The study found that the current methodology is not more valid for the conditions in which radiation beam widths get wider for multi-slice scanners. A 10 cm long ion chamber ($CTDI_{100)}$ for measuring the integral of the single slice profile is not an efficient route. The authors recommended that in a multi-slice scanner, a long ion chamber measurement can underestimate the integral of dose line and the equilibrium dose by 20% in the middle of the body phantom, while in the middle of the head phantom, the measurement can be underestimated by about 10% for a 20 mm nominal beam width. It was suggested that rather than using a long ion chamber, a small volume ion chamber can be used for accumulating the broad scatter tails of the single slice. Dixon demonstrated that a small volume ion chamber is an alternative to the CTDI method and can scan a phantom of enough length to create equilibrium dose at any position of the chamber. It has been found that with a helical or axial series, the time for scanning would be less than or equal to 15 seconds with a modern CT scanner. Therefore, the small volume ion chamber method would be a less time-consuming approach than the long chamber technique.

Dixon and Ballard[48] performed research based on the experimental demonstration and authentication of a versatile system of CTDI. The authors also utilized a short conventional ion chamber. They demonstrated that a small ion chamber is more effective than a long pencil chamber, and it is more versatile than the latter. The accumulated dose value can be efficiently and correctly estimated by $CTDI_{100}$ for a single total scan length, i.e. 100 mm, and the limiting equilibrium dose is underestimated by this method for longer body scan lengths. The wide-ranging set of measurements was performed by Dixon and Ballard to prove that effectiveness and adaptability of a small ion chamber method. They discovered that a small ion chamber could be used with any desired scan length (L) to accurately predict accumulated dose and

CTDI$_L$ values and that the limiting equilibrium dose D$_{Eq}$ can be measured for any value of desired scan length with accuracy.

In comparison, the values of CTDI$_L$ were found to be in agreement with the values estimated by a pencil chamber of any length. It was determined that a small ion chamber method had no hidden drawbacks. Only a scatter-induced current was encountered in the electrometer because of the improper location and the conveyance and control of the 400 mm long phantom. For any scan length, the accumulated dose can be measured at a desired location in the phantom. Another benefit of a small ion chamber method is that it can measure accumulated dose at any point instead of just the middle point of the scan length, which is the limitation of using a pencil chamber measurement.

Descamps[49] et al. followed the AAPM TG111[10] guidelines for measuring the accumulated doses while using common CT protocols. They also compared the accumulated doses with the measured doses derived by the end of each CT scanning. Descamps et al. suggested that the efficacy of a long ion chamber (pencil chamber) is low due to the unaccountability of the radiation integration, which is scattered beyond 100 mm along the z-axis. They suggested that the CTDI index observed with a 10 cm long ionization chamber using a Perspex phantom (i.e. 14 cm long PMMA), which is typically used for estimating the CT doses, is no longer versatile for the new era CT scanners. Following the AAPM TG111 report[10], they proposed that a small volume ionization chamber is a novel measurement modality that allows using a phantom of enough length for creating dose equilibrium at any desired position of the chamber. They also evaluated the minimum scanning length required for the accumulation of dose equilibrium. The value of dose equilibrium was measured and compared to the values of CT index produced by the CT scanner, and TLD measurements were used to confirm the dose values. Descamps et al. observed a difference of less than 1% between values of dose cumulated using TLD and

with small ion chamber, and a difference of 0.4% in reproducible measurement setup. The results demonstrated that scanning lengths of 450 mm and 380 mm are required for obtaining the cumulated dose equilibrium for the central and peripheral axes, correspondingly, which validates the phantom length. For the relevant clinical profiles, the equilibrium doses were measured as 30% higher than the doses reported by the CT scanner. For CT systems having wide longitudinal detectors, the present CTDI methods are no longer acceptable as the reported CT index tends to underestimate the value of dose delivered. Descamps et al. suggested that the AAPM TG111[10] methodology should be followed to evaluate the dose. A methodical underestimation in the range of 30%–35% has been reported by researchers regarding the doses transported during CT scans to the patient. The doses informed by the CT scanner at the end of the exams are still based on the CTDI paradigm. It has been found that for new cone-beam innovation, it is critical to consider CT radiation dose using a small active volume ionization chamber informed by the AAPM report[10], which is usually utilized in radiotherapy administrations for CT beam quality. The TLD estimations approved the right estimations setup and the AAPM system.

Campeloa[50] et al. demonstrated that at the gantry center, the $CTDI_{100}$ estimations would undervalue the accumulated dosage for CT. An improved metrics was informed by the AAPM TG 111 report[10] for CT dose measurements, primarily for helical and wide beam scanning. For this study, the authors applied a TG 111 methodology for assessing the CT dose using a small ionization chamber. For different protocols and pitch values, they measured the dose profiles and Equilibrium dose free-in-air ($D_{Eq,air}$). The findings demonstrated that when pitch is reduced, the $D_{Eq,air}$ is increased. They observed a 30-37% difference in Planar Average D_{Eq} and $CTDI_{vol}$ estimations using a 450 mm CT phantom. In this technique, the dose profile tail contribution is not included in the $CTDI_{vol}$ because of the scattering in phantom, particularly when wide beam widths are used. Interestingly, the findings of Campeloa et al. are in close

agreement with that of Descamps et al., who worked with a Siemens CT scanner, and that of Dixon and Ballard, who worked with two GE scanners. Dixon and Ballard (2007)[48], Dixon (2003)[9], Campeloa et al. (2016)[50], and Descamps et al. (2012)[49], have validated the efficiency of using small ionization chamber for CT dose estimation as compared to CTDI with long chamber.

According to McCollough[46] et al., the CTDI method has been criticised on two primary estimations. Firstly, a 100mm pencil ionization chamber for collecting the dose is not sufficient to include all ends of the scattered dose distribution. Secondly, in comparison to an adult torso, the phantoms utilized for CTDI estimations are shorter and, therefore, they cannot produce enough of the required scattered radiation as would be occurring in an adult. The authors found that a 14 cm CTDI phantom would underestimate by up to 40% the average dose in an adult torso. They concluded that a small ion chamber method is an imperative alternative that efficiently measures the output radiation of a CT scanner. This criterion is met by the $CTDI_{vol}$ as it provides accurate information about how the equipment was worked, and it tends to be utilized relative to data concerning size and anatomy for the estimation of CT dose. The CTDI measurements are not, in any case, dose values. In a CT scanner, the CTDI is the tachometer, not the speedometer. McCollough et al. suggested that the individual patient risk estimation and epidemiologic investigations evaluating potential impact of ionizing radiation must utilize understanding of patient size based dose values (the scanner output, i.e. $CTDI_{vol}$ or DLP, cannot be used alone). Using the known exponential comparison between patient size and patient absorbed dose can enable estimations of size-based dose values using CT scan system output.

3.4 CT scanners used in the study

Two different CT scanners were used in this study. In Chapter 4, a Philips AQsim CT scanner with three different protocols (head, chest and abdomen) was used, while a Toshiba Aquilion CT scanner was used in Chapter 5 with two different protocols (thoracic and abdominopelvic). A Toshiba Aquilion scanner was also used in Chapter 6.

3.5 Thermoluminescent dosimeter used in the experiment

A thermoluminescent dosimeter (TLD) is comprised of a thermoluminescent (TL) crystalline material such as lithium fluoride (LiF) or calcium fluoride (CaF). When a TLD is exposed to radiation, all or part of the incident energy is deposited in the crystal. Some of the crystal atoms become ionized, yielding free electrons and gaps called electron holes. Any imperfection in the crystal lattice structure can trap and immobilize free electrons[51,52].

When the crystal is heated, the crystal lattice vibrates and releases the trapped electrons, which return to the ground state and release energy as light. This light is counted with photomultiplier tubes and is proportional to the amount of radiation striking the crystal [51,52].

When the amount of light released versus heating of the thermoluminescent material is measured, the glow curve produced is then related to the radiation exposure; furthermore, the process can be repeated several times[51,52]. A model of this process is shown in Figure 3.1.
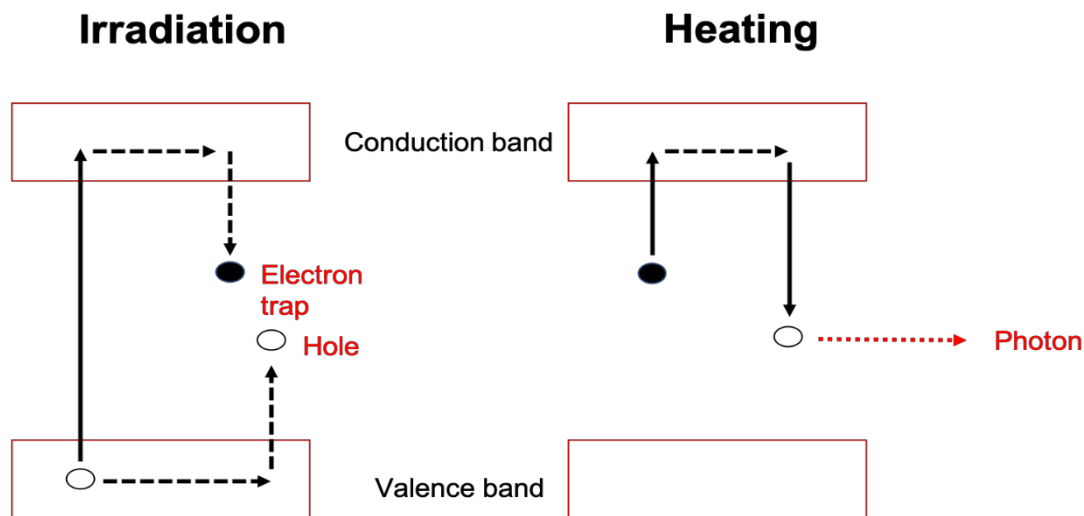
Figure 3. 1: Simplified representation of the thermoluminescent process

The TLD used in this thesis is TLD-100H, a promising thermoluminescent material that consists of a lithium fluoride matrix with magnesium, copper and phosphorus (LiF:Mg,Cu,P). The key advantages that account for its current popularity are high sensitivity, good tissue equivalence, an almost flat energy response, a linear dose response, stability at ambient temperatures and short annealing procedures[53]. From the time LiF:Mg,Cu,P was developed at the Solid Dosimetric Detector and Method Laboratory (DML) [54], the features of the material have been refined [53]. However, LiF:Mg,Cu,P drawbacks include loss of TL sensitivity at temperatures above 240 °C and a high residual signal [55,56]. Nonetheless, Horowitz and Moscovitch[57] reported that the only real problem is that temperatures above 240 °C can permanently damage LiF:Mg,Cu,P, while maximum temperatures below 240 °C increase the residual signal.

Twenty chips of TLD-100H were calibrated with diagnostic X-ray device (100 kV and 100 mAs at 1m, standard beam size 10x10cm) and compared against a pencil ionization chamber.

The luminescent signals were measured by an automated TLD reader (Model 3500, Harshaw)

3.6 Phantom used in the study

This thesis describes a new CT dosimetry system that replies on radiation absorption and scattering phantoms using a sufficiently long (450 mm) phantom to accommodate scanning length relative to cumulative dose equilibrium.

Initially, a 450 mm long, 320 mm diameter (three sections of 150 mm phantoms are joined together) polymethyl methacrylate (PMMA) phantom was proposed; however, difficulties were encountered. Three companies were contacted to build it, but they all responded that it would be very difficult to connect the three 150 mm phantoms, and there would be a gap between each part. Another problem was that it would be heavy and very difficult to move throughout the hospital and place on a patient's table.

Subsequently, a water phantom was designed. It was determined that a water-filled, 320 mm diameter phantom, 500 mm long would correspond to the attenuation and absorption of the average sized adult body, as shown in Figure 3.2. The phantom was designed to be transported empty and once placed on the table, it could be quickly filled or emptied in one minute with a small pump connected to a room sink. The material needed for the phantom was obtained online, and the device was built in the lab at (NUIG). The material composition of the phantom was based on IAEA TRS 277 [58].
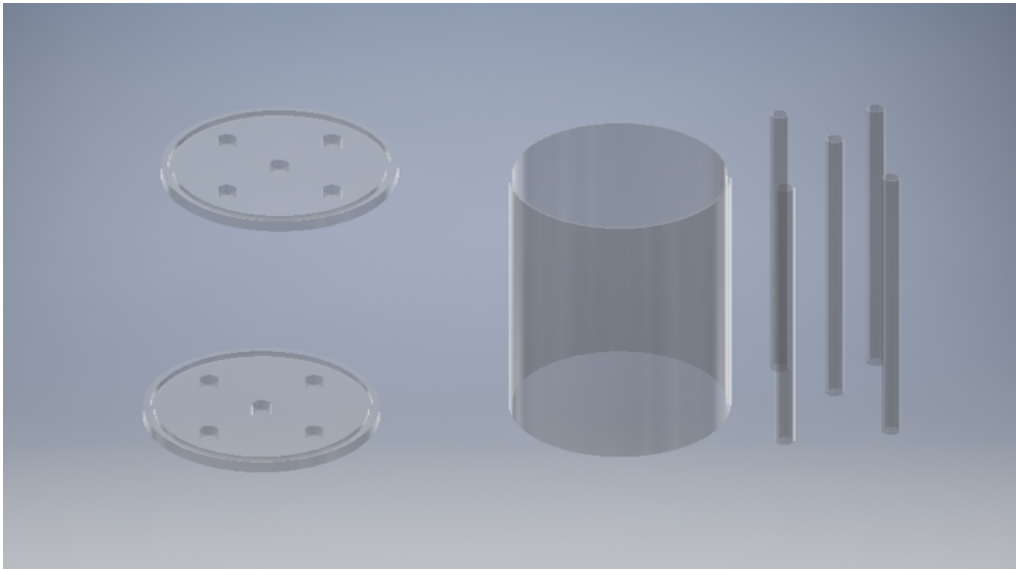
Figure 3. 2: Schematic image of all parts of the D_{Eq} phantom separately

Chapter 4 (CT output dose performance – conventional approach versus the dose equilibrium method)

4.1 Introduction

The current CT dosimetry method is based on the CTDI concept using a single axial rotation of the X-ray tube in a phantom. Measurement involves a $CTDI_{100}$ inserted in a cylindrical PMMA phantom to represent the head and body. Modern CT scanners with helical scanning modes, dose modulation, array detectors and multiple slice planes or cone-beam irradiation geometries make CTDI unsuitable [59,60]. The CTDI method is based on two major limitations. Firstly, the pencil ionization chamber, which is 100-mm-long and used to collect the dose, is not sufficiently long enough to measure the tails of the scattered dose distribution[61]. Secondly, the CTDI phantoms are 14-cm-long, much shorter than the average adult torso, and cannot replicate the scattered radiation that would occur in a typical adult [62]. The AAPM TG111[10] described a new measurement method that would take into account the scatter of modern CT scanners. The report recommended using a small volume ion chamber and a phantom length that allows for dose equilibrium at the location of the chamber [10]. As this type of phantom is not commercially available, the aim of this thesis was to construct and characterise a phantom based on the AAPM TG 111 report and then measure the accumulated dose and equilibrium dose using a Farmer chamber. A second objective was to compare the dose estimation of the current CTDI standard and independently verify the dose measurements with TLDs. The hypothesis of the study is that the D_{Eq} method correctly estimates the true patient dose.

4.2 Materials

4.2.1. Dose Equilibrium Phantom

An in-house water-based phantom was developed based on the work of Dixon et al.,[10,63] referred to from this point as the D_{Eq} phantom. The D_{Eq} phantom was designed and constructed at NUI Galway (Figure 4.1). It is 320 mm in diameter and 500 mm in length. The D_{Eq} phantom is constructed with a center hole and four peripheral holes. The holes are filled with blanks when not in use. It is designed to be transported empty, and once placed on the table, it can be quickly filled or emptied with a small pump operating from a room sink as a reservoir. This phantom size was chosen in order to represent the attenuation and absorption characteristics of the average size adult body. The material composition of the phantom was based on IAEA TRS 277 [58].
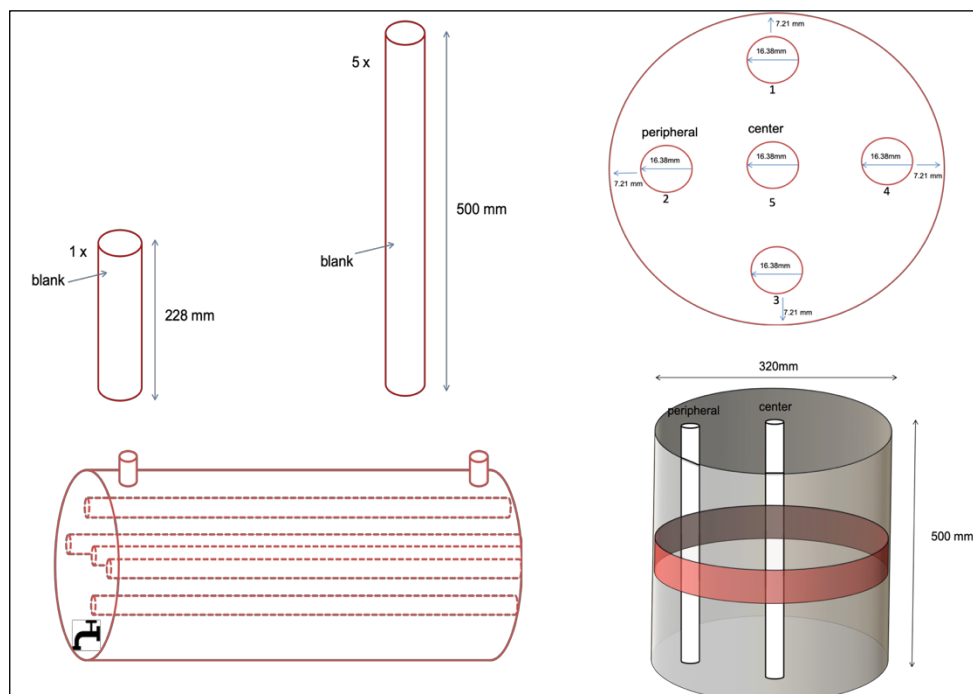
Figure 4. 1: Diagram of D_{Eq} phantom
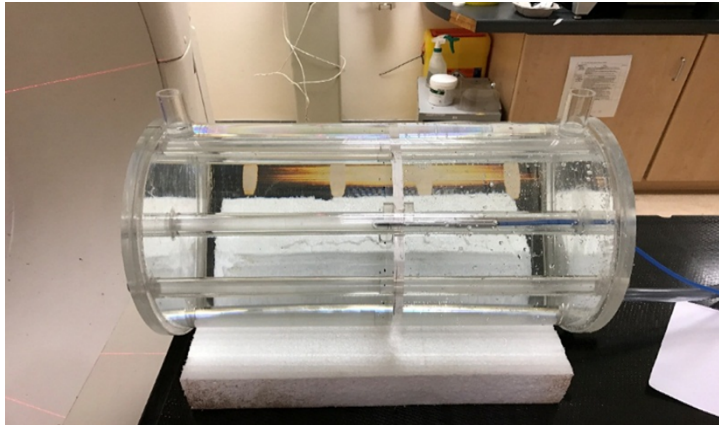
Figure 4. 2: D$_{Eq}$ phantom with ion chamber fitted in the center

4.2.2. Perspex Phantom

The CTDI phantom was a commercial product obtained from West Physics. It consisted of two PMMA cylinders: one cylinder represented the head (160 mm diameter), and the other represented the body (320 mm diameter). The length of each cylinder was 140 mm. Each cylinder contained holes large enough to accept a pencil chamber and were filled with Perspex blanks when not in use.

4.2.3. Computed Tomography Scan, Ionization Chambers and TLDs

A Philips, AcQsim CT was used for the measurements. Dose measurements were taken using the Farmer chamber (PTW type 30013), as shown in Figure 4.3, and a pencil chamber (Unfors xitm). Both are ionization-based chambers. The Farmer chamber collection volume is 0.6 cm^3. It was calibrated by the National Standards of the German National Laboratory. A PC electrometer from Sun Nuclear was used for the Farmer chamber, configured with a cable long enough to allow the electrometer to operate outside the scatter-radiation field in order to avoid inducing extraneous currents in the electrometer. A PC electrometer provided a bias voltage of ±300 Volts, having a sensitivity and a leakage current consistent with the Farmer ionization

chamber volume and dose rate[64].

The pencil chamber was 10 cm long and was calibrated by Unfors RaySafe. Dose verification was performed independently using thermoluminescent dosimeters (TLDs-100H), as shown in Figure 4.4, which were independently checked for accuracy.
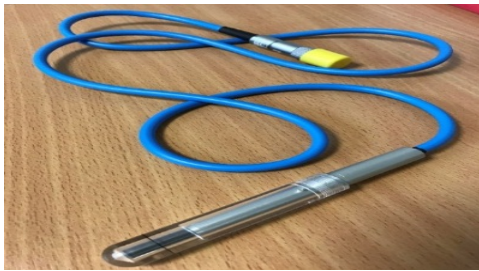
Figure 4. 3: PTW Farmer chamber
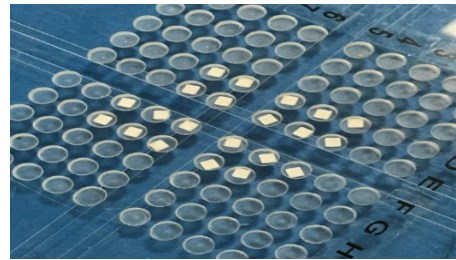
Figure 4. 4: TLD-100H chip.

4.3 Methods

4.3.1 Beam Attenuation in the D_{Eq} Phantom and CTDI Phantom

The dose output from one single slice in the middle of the D_{Eq} phantom and Perspex phantom by using the pencil chamber was used to validate the dose attenuation from D_{Eq} phantom. For this work, the sequences were: axial scanning mode, kV = 130 kVp, 100 mA, N = 1 mm (number of slice) and T = 5 mm (tomographic section nominal width).

4.3.2 Using the Farmer Ionization Chamber

4.3.2.1 Accumulated dose

Scanning a D_{Eq} phantom moving along the z-axis through a rotating x-ray produces an accumulated dose that can be envisaged as a dose amassed by super positioning stationary,

longitudinally displaced single-scan dose profiles.

With the small ion chamber method, the accumulated dose is directly measured by integrating the current from an ion chamber located at a fixed point in the phantom at the mid-point of the scanned length[65] (Figure 4.5), while the D_{Eq} phantom central axis was aligned with the CT rotation axis. The Farmer chamber was placed in the phantom in order to center the charge collection volume. The electrometer, which was placed outside the scan room, was connected to the Farmer chamber using a cable that reduced the extra chamber current. The charge collected in the ion chamber qh (nC) was converted to accumulated dose D(0) as follows[48]:

$$D_{(0)} = N_k * q_h * (\mu_{(en)}/\rho)_{air}^{water} \qquad (4.1)$$

where q_h (nC) is the total charge collected by the ionization chamber during scanning over the length L, N_k (mGy/nC) is the ionization chamber calibration factor supplied by national standards of the German national laboratory, $N_k = 535 * 10^5$ Gy/C and $\left(\left(\frac{\mu_{(en)}}{\rho}\right)_{air}^{water}\right)$ is the ratio of the mass-energy absorption coefficient for water to air. This ratio will vary somewhat with kVp, when the phantom is between the central and peripheral axes and even as the ionization chamber moves along the z-axis. However, the variation is less than 3% [10,66]. By following the IAEA TRS-277[58], the energy absorption coefficient ratio water to air was 1.036.

The accumulated doses in the center and peripheral locations were measured for frequently used clinical protocols [49]. The parameters of each protocol are detailed in Table 4.1. Protocol 1 was used for the head, protocol 2 for the chest and protocol 3 for the abdomen.
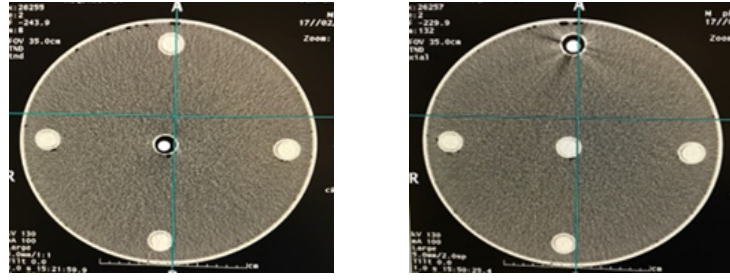
Figure 4. 5: Farmer chamber position (center and peripheral)

Protocol	Protocol 1 Head	Protocol 2 Chest	Protocol 3 Abdomen
Scanning mode	Axial	Axial	Axial
kV	130	120	130
mA	100	100	100
N (mm)	2	2	2
T (mm)	5	5	4
Pitch factor=b/nT	1	1	1
Time per tube rotation	1s	1s	1s
Scan length	250	450	450

Table 4. 1: Details for the sequence of the protocols used.

(n= slice number, T= slice width, b = table increment in a sequence of axial scanning or continuous table advance per rotation during helical scanning).

4.3.2.2 Equilibrium dose

The D_{Eq} is based on an upper limiting value that is derived from the relationship of the scanning length and cumulative dose. When the scanning length (L) increases, the cumulative dose at z = 0 increases, along with accumulating contributions from the scatter tail outlying scan sections, toward an upper limiting value in which the source of scatter radiation only makes negligibly small additional contributions. The D_{Eq} is given by [10,50] :

$$D_{Eq} = \frac{D_{(0)}}{h_{(L)}} \qquad (4.2)$$

63

The h(L) is an approach to equilibrium function, where h(L) = 1 when L becomes large enough to yield scatter equilibrium at z = 0. h(L) has an approximate form as a constant plus an exponentially dependent term leading to saturation [36]. The D_{Eq} was determined for both the centre and peripheral axes for three protocols (Table 4.1), then the planar average equilibrium dose[10,49] was determined by Equation 4.3 and compared with the CTDI volume. [15,14]

$$D_{Eq} = \frac{1}{2} D_{Eq,center} + \frac{1}{2} D_{Eq,peripheral} \qquad (4.3)$$

4.3.3. Using pencil ionization chamber

CT dose index concepts are well documented, and it is currently the primary dose measurement in CT scan [67,68]. The CTDI represents the average absorbed dose along the z-axis from a series of contiguous irradiations. It is measured from one axial CT scan and is calculated by dividing the integrated absorbed dose by the nominal total beam collimation [67–70] as:

$$CTDI = \frac{1}{NT} \int_{-\infty}^{\infty} D(Z) dz \qquad (4.4)$$

where D(Z) is the radiation dose profile along the z-axis, N the number of tomographic sections imaged in a single axial scan and T the number of data channels.

The CTDI was proposed and established in the United States by the Food and Drug Administration (FDA) [45,71]. It is measured by using a 100 mm long ionization chamber and determined by [67,70,72]:

$$CTDI_{100}(Gy) = \frac{100mm.meter\ reading(Gy)}{NT(mm)} \qquad (4.5)$$

The $CTDI_{100}$ was determined for central and peripheral axes for the three protocols using the Perspex phantom. To make a comparison between the CTDI approach and the D_{Eq} method, the

CTDI was obtained by taking the dose from the pencil chamber for one slice, multipling by 100 and then dividing by the number of slices and the thickness (NT) of the beam (Equation 4.5) to determine the dose profile over the whole chamber. This allowed assessment of CTDI volume and comparison with the planer average D_{Eq}.

4.3.4. Using TLD-100H

Dose measurements were also performed in the D_{Eq} phantom using TLD-100Hs for the verification of the dose calculation by the Farmer chamber (D_{Eq} method). TLD-100H chips have a high sensitivity, and they are commonly used in diagnostic radiology. However, they have different annealing and reading requirements than other TLDs. TLD-100H chips must not exceed a temperature of 240℃, and the recommended annealing cycle for TLD-100H chips are 240℃ for 10 minutes [57,73].

Twenty TLD-100H chips were calibrated with a diagnostic X-ray system. The luminescent signals were measured by an automated TLD reader (Model 3500, Harshaw), and the calibration factor for the TLDs was determined using the signal integration of the last two peaks[58], which was 0.00385 mGy/nC. Three of TLDs chips were excluded as they were found to be two standard deviations away from the mean.

Four TLD chips (Figure 4.6) were placed in the center of the D_{Eq} phantom for each protocol, and the average of four readings for each protocol was reported and compared with dose values obtained from the Farmer chamber.
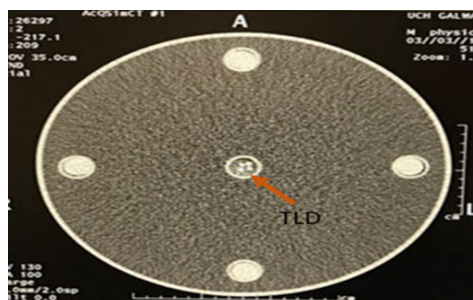
Figure 4. 6: TLD chips in the center of D_{Eq} phantom

4.4 Results and Discussion

4.4.1 Beam Attenuation in the D_{Eq} Phantom and CTDI Phantom

The dose outputs from the D_{Eq} phantom and the Perspex phantom were 0.34 ±0.01 mGy and 0.33 ±0.01 mGy respectively, as shown in Table 4.2. Thus, the dose attenuation in the D_{Eq} phantom is equivalent to the dose attenuation in any standard CTDI phantom.

Phantom	First reading	Second reading	Third reading	Average
Water phantom	0.33	0.35	0.34	0.34±0.01
Perspex phantom	0.33	0.34	0.33	0.33±0.01

Table 4. 2: Single slice dose output at the center of D_{Eq} and Perspex phantoms

4.4.2 The Planar Average Equilibrium Dose

The planar average D_{Eq} was obtained using Equation 4.3. The centre and periphery were measured for three protocols to find the planer average D_{Eq}, which is listed in Table 4.3. The planar average D_{Eq} was 12.14 mGy for all protocols.

Protocols	Center (mGy)	Average±SD	Peripheral (mean) (mGy)	Average±SD	D_{Eq} (mGy)	Average±SD
Head	11.99		14.31		13.15	
	12.22	12.13±0.1	14.24	14.34±0.1	13.22	13.24±0.1
	12.17		14.49		13.33	
Chest	10.45		12.55		11.51	
	10.64	10.58±0.1	12.41	12.53±0.1	11.52	11.56±0.1
	10.65		12.65		11.65	
Abdomen	10.12	10.04±0.1	13.31		11.71	
	10.10		13.22	13.22±0.1	11.66	11.63±0.1
	9.91		13.15		11.53	
Average	11.08		13.56		12.14	

Table 4. 3: Planar average equilibrium dose.

4.4.3 CTDI Volume Measurements and Comparison with the Planar Average D_{Eq}

The CTDI volume was measured by a Perspex phantom for all protocols and compared to the planar average D_{Eq} for head, chest and abdomen, resulting in an underestimation of 28%, 35% and 25%, respectively, across the three protocols. This data is presented in Table 4.4. Additionally, the measured single slice dose profile at the center of the D_{Eq} phantom (Figure 4.7) indicated that the scan length of 100 mm was not long enough to measure all the tails of the scattered dose distribution, confirming that the CTDI methodology is no longer adequate to accurately characterise CT dose performance.

Protocols	D_{Eq} (mGy)	average±SD	CTDI volume (mGy)	average±SD	Variation
Head	13.15		10.4		
	13.22	13.24±0.1	10.37	10.38±0.01	28%
	13.33		10.39		
Chest	11.51		8.57		
	11.52	11.56±0.1	8.49	8.54±0.03	35%
	11.65		8.57		
Abdomen	11.71		9.26		
	11.66	11.63±0.1	9.20	9.25±0.03	25%
	11.53		9.29		

Table 4. 4: CTDI volume compared with planar average equilibrium dose
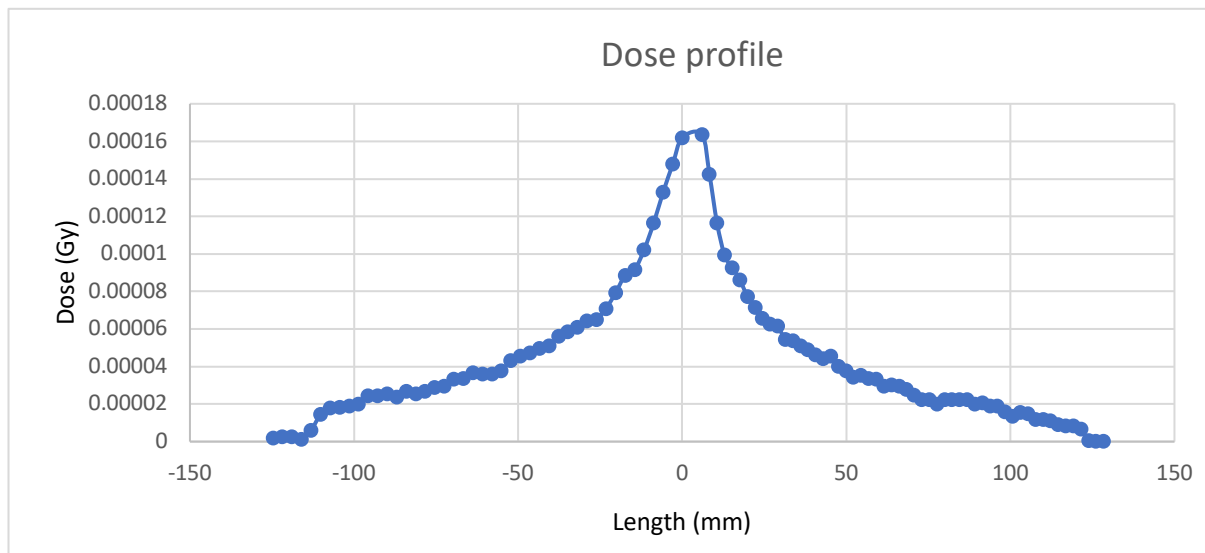
Figure 4. 7: Single slice dose profile at the center

4.4.4 TLD Measurement and Comparison with Equilibrium Dose

The comparison between the TLD in the centre (Figure 4.6) and dose equilibrium in the centre is shown in Table 4.5. The variation between the TLD and D_{Eq} for all protocols was less than 6%; therefore, TLD confirmed the accuracy of the D_{Eq} methodology.

Protocols	D$_{Eq}$ Center (mGy)	average±SD	TLD center	average±SD	Variation
Head	11.99	12.13±0.1	12.86	12.93±0.5	5%
	12.22		13.68		
	12.17		12.36		
			12.84		
Chest	10.45	10.58±0.1	10.20	11.04±0.5	4%
	10.64		11.42		
	10.65		11.54		
			11.01		
Abdomen	10.1	10.04±0.1	9.73	10.42±0.5	3%
	10.1		10.89		
	9.91		10.99		
			10.08		

Table 4. 5: TLD compared with D$_{Eq}$

4.5 Conclusions

Organ and tissue radiation dose prior to a CT scan is currently estimated in Ireland's health service using IMPACT software[74], and other healthcare systems use similar estimates. These estimates are based on detailed system-specific Monte Carlo simulations and a mathematical model of human phantoms [63].

The organ dose and accumulative dose are based on CTDI, which has been shown to underestimate the dose. As can be seen in Table 4.4, the 10 cm chamber measurement underestimated the actual dose by 25% to 35%.

Descamps et al.[49] determined the planar D_{Eq} for chest, prostate and metastasis protocols to be 12.3 mGy, 12.3 mGy and 12.5 mGy, respectively. This was compared to the CTDI volumes for the same three protocols, which were 9.1 mGy, 9.3 mGy and 9.3 mGy, respectively. The authors reported underestimation of 30% to 35% in dose as measured by CTDI. Furthermore, Dixon et al.[9] found that the current methodology based on the measurement of the integral of the single slice profile using a 10 cm long ion chamber underestimated the D_{Eq} and dose line integral by about 20%. Thus the two studies are in good agreement with the current findings.

The 100-mm pencil chamber was too short, and it underestimated the limiting D_{Eq} for any scan length above 100 mm. As a result, the organ dose obtained from IMPACT software may underestimate the radiation dose absorbed by the organs, increasing patient risk.

Alternately, using a small ion chamber and a phantom long enough to establish D_{Eq} in the centre can provide a more realistic dose estimate. In addition, a measurement of an accumulated dose can be determined at any point in the phantom, not just at the centre of the scan length, which is the only location at which the pencil chamber in CTDI can measure accumulative dose to formalize a dose prediction. The D_{Eq} method is more flexible and not significantly more time consuming than the current method that uses a long chamber.

Chapter 5 (Adult thoracic and abdominopelvic CT: Does equilibrium dose assessment provide more sensitive organ dose estimation than conventional CTDI?)

5.1 Introduction

The high dosage of radiation due to increased use of CT is of concern as it could result in negative health outcomes [75,76]. Superficial organs sensitive to radiation, such as the breast, thyroid, and the lens of the eye are particularly susceptible because they receive nondiagnostic radiation doses during X-ray imaging procedures of the chest, cervical spine, and head respectively [77–79]. As the radio sensitivity of each organ differs, it is paramount to accurately quantify the doses delivered to individual organs.

Both direct and indirect methods are used during CT examinations to determine the level of radiation absorbed by the tissues and organs. An evaluation of the patient dose by the indirect method was performed through measurement of the CTDI and published conversion factors that normalised to CTDI [80–82]. Estimating CT doses using simulation programs incorporates the parameters of $CTDI_{,air}$, tube current, tube rotation time and pitch values. $CTDI_{100}$, expressed as the ratio of absorbed dose to air (mGy), can be measured using a 100 mm active length pencil ionization chamber [83] located free-in-air and parallel with the scanner's axis of rotation. The effective dose requires tissue weighting factor input. The tissue weighting factor options include ICRP 26, ICRP 60 and ICRP 103, published in 1977, 1991 and 2007, respectively [84,85].

Various dose estimation programs like IMPACT [86], CT Imaging and CT-EXPO [87] are used to estimate a priori patient dose in CT applications [88]. IMPACT calculates organ dose based on

the NRPB conversion factors [86]. The tissue weighting factors used are based on either ICRP 103 or ICRP 60 software [84,85]. IMPACT organ doses are based on 23 Monte Carlo datasets from NRPB's SR250 report and a simulated hermaphroditic patient (MIRD-5 phantom) with organs and tissues that are modelled mathematically [[86],[89]].

All dose estimation programs (e.g. IMPACT [86], CT Imaging and CT-EXPO [87]) use the CTDI dosimetry method for CT dose assessment. CTDI has been shown to be less accurate in modern wide beam systems because the CTDI method cannot account for all of the scatter radiation using a 10 cm pencil ionization chamber, which could result in underestimation of the organ dose [9,49,90]. To correctly estimate dose, AAPM task group 111 proposed a new measurement paradigm for dose calculation, the planer D_{Eq} [10,62].

Another evaluation of patient dose is the direct method, which uses a humanoid phantom (Alderson Rando phantom) with small devices such as TLDs.

The aim of this chapter is to use the AAPM D_{Eq} method [10,62] to estimate organ dose values, and then compare the organ dose values of both indirect methods (D_{Eq} and CTDI) and a direct method (TLD) . A summary of the entire process involved in this chapter is shown as a flow chart in Figure 5.1.
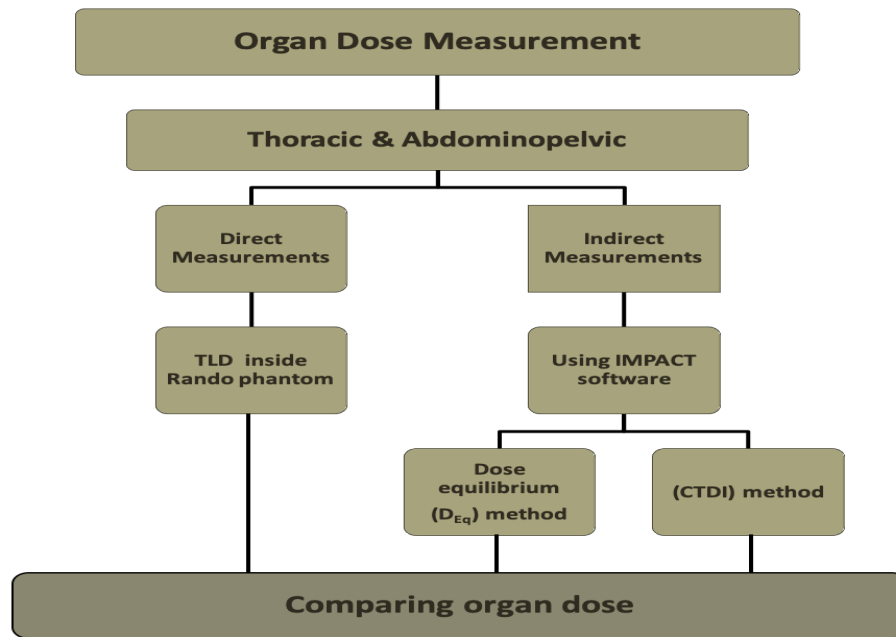
Figure 5. 1:Summary of the entire process involved in this study

5.2 Materials and Methods

This study used a Toshiba Aquilion 16, a third-generation multi-slice helical CT scanner, a 60-kW generator and a 7.5 MHU tube.

An Alderson Rando phantom (Alderson Research Laboratories, USA)[91] was also used in this study. The phantom is a natural human skeleton embedded in a synthetic isocyanate rubber that is tissue-equivalent over the required range of energies. It is sliced horizontally into 32 segments, each 2.5 cm thick, along with removable blanks to accommodate TLD chips [92].

Thoracic and abdominopelvic regions of the Rando phantom were scanned using typical clinical protocols. Table 5.1 provides the scan parameters for kV, mA, rotation time, slice thickness and pitch used in this study, while the scan length for each protocol was 450 mm. The thoracic organs scanned were the thyroid, lung, heart and liver. The abdominopelvic organs scanned were the kidney, bladder, prostate and testis. The scan length for each scanning

protocol and the organs for each region are shown in Figure 5.2.

Region	Scan Mode	kV	mA	Rotation/Sec	Thickness(mm)	Number of Slice	Pitch
Thoracic	helical	135	150	1	4	4	0.6
Abdominopelvic	helical	120	100	1	4	4	1

Table 5. 1: Summary of scan parameters used for the examination of thoracic and abdominopelvic regions.
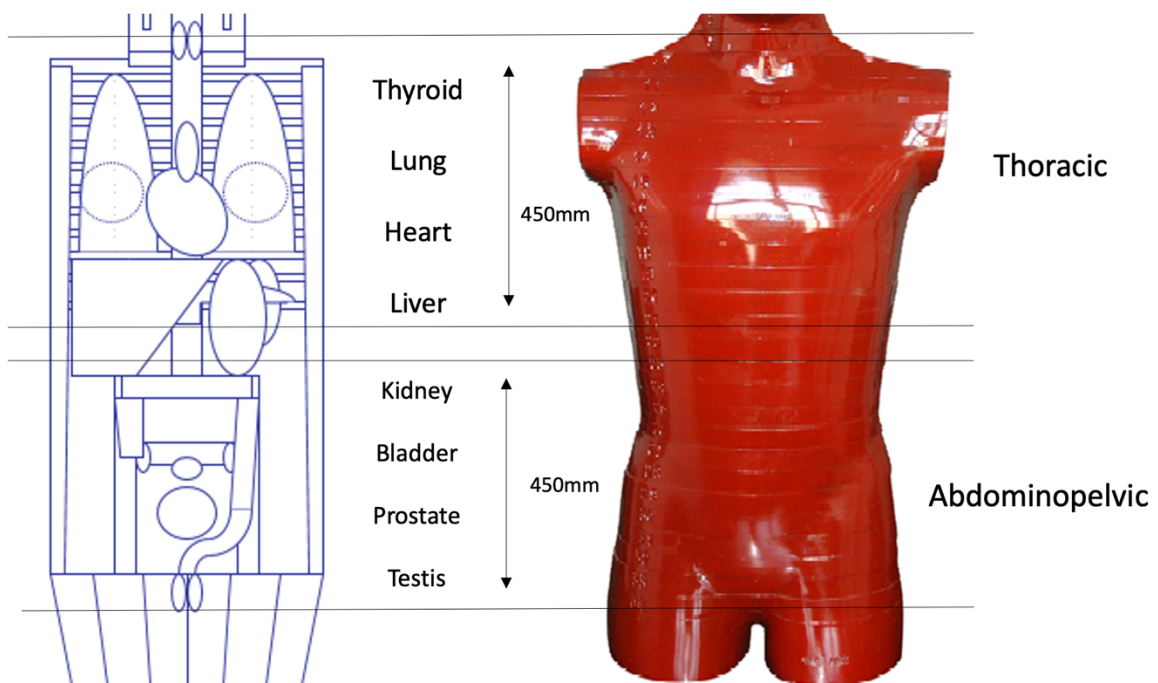
Figure 5. 2: Scan region and its length for two examinations shown on Alderson Rando Phantom (right) and MIRD-5 phantom (left)

5.2.1 The planar average D_{Eq} measurement and comparison with CTDI value measurement

A detailed D_{Eq} phantom characterisation and comparison to CTDI has previously been discussed in Chapter 4 [90]. The D_{Eq} method uses an upper limiting value based on the scanning

length (L) and the cumulative dose ($D_{(0)}$). There is a direct relationship between the scanning length (L) and the cumulative dose at z = 0, along with accumulating contributions from the outlying scan sections, until an upper limiting value is reached and the scatter radiation produces negligible contributions [10,59,90]. In this chapter, the D_{Eq} was determined for the centre and the peripheral axes for the two protocols (Table 5.1), with the planar average D_{Eq} then determined using Equation 5.1 [50,78,90]:

$$D_{Eq} = \frac{1}{2} D_{Eq,center} + \frac{1}{2} D_{Eq,peripheral} \qquad (5.1)$$

The D_{Eq} was compared to CTDI values that were obtained from the readout of the CT scanner. CTDI uses a pencil-type ionization chamber that has a 100 mm active length and is inserted into the phantom holes to measure the dose by taking a single rotation without table movement. This allows the assessment of the weighted CTDI ($CTDI_w$) and the volumetric CTDI ($CTDI_{vol}$)[69,71,83]

5.2.2 Organ dose measurement using direct measurement

TLDs and a rando phantom were used in the direct measurement method to obtain organ doses.TLD-100H was used for point dose measurements. lithium fluoride matrix with magnesium, copper and phosphorus, consists of solid pellets 4.5 mm in diameter and 0.9 mm thick. TLD chips with sensitivities within ±5%[52,90] were first tested. Four of the chips were placed in a selected hole per organ representing the thyroid, heart, lungs, liver, kidney, bladder, prostate and testis. The TLDs were placed within the phantom based on a human anatomy CT atlas. A bolus was placed on the skin to produce dose equilibrium on the testis.

After exposing the TLDs during the CT examination protocols, the preread heating process was conducted. The recommended annealing cycle for TLD-100H chips is 10 minutes at 240˚C

[52,57,73], a temperature the chips did not exceed. An automated TLD reader (Model 3500, Harshaw) was used to count luminescent signals[73].

5.2.3 Organ dose measurement using indirect measurement

IMPACT pre-calculates CTDI measurements in free air ($CTDI_{100}$), centre ($CTDI_{100}$, C) and peripheries ($CTDI_{100}$, P) measured in a standard Perspex head and body dosimetry phantom, using the 10 cm pencil ionization chamber. These measurements were used to calculate CTDI weighted ($CTDI_w$), CTDI volume ($CTDI_{vol}$), DLP and other dose parameters.

Doses to the thyroid, lung, heart, liver, kidney, bladder, prostate and testis were determined using the $CTDI_{air}$ and organ dose conversion coefficients normalised to CTDI [89]. The $CTDI_{air}$ values were then converted to CTDI tissue values based on the mass-energy absorption coefficients ($\mu en/\rho$) ratio of tissue to air [93–95]:

$$CTDI_{tissue} = \left(\left(\frac{\mu_{(en)}}{\rho} \right)^{tissue}_{air} \right) * CTDI_{air} \qquad (5.2)$$

The ratio of the mass-energy absorption coefficient of soft tissue to air is used at a constant value of 1.07 [86,94,95], for normal spectra produced by the CT, even though it depends on photon energy. Using the scanner-specific organ dose conversion coefficient allows the typical average organ dose ($D_{org,T}$) for individual examination to be estimated as [78,93,96]:

$$D_{org,T} = CTDI_{tissue} \sum_{Z1}^{Z2} f(organ, Z) \text{normalised to CTDI} \qquad (5.3)$$

where $f(organ, Z)$ is the organ dose conversion factor and Z1 and Z2 the start and end points of the scanned region, respectively. CT scanner manufacturer and model along with typical scanning parameters such as kV, mA, exposure time, pitch, slice thickness, gender and start/end

positions were used to estimate organ dose [86,89,94].

The CTDI$_{air}$ was obtained from the dose measurement along the z-axis at the gantry isocentre in a 10 cm pencil ion chamber (Unfors xitm™) connected to an electrometer [76]. The organ dose for each CT examination using the parameters in Table 5.1 and equation 5.3 was determined, and the organ dose results by CTDI method were derived by CTDI$_{air}$ and CTDI$_{vol}$ in IMPACT software, as well as using organ dose conversion factor normalised to CTDI.

Using a D$_{Eq}$ phantom [10,62], a small ion chamber and by scanning the length of the phantom, dose equilibrium was established at the centre of the phantom. The D$_{Eq}$ phantom was built in-house [90] using a water-filled phantom based on the work of Dixon and Ballard [48,49]. It is 320 mm in diameter and 500 mm in length, with a centre hole and four peripheral holes. Perspex blanks were placed in the holes when not in use. This chosen phantom size represents the attenuation and absorption characteristics for an average adult. The material composition of the phantom was based on IAEA TRS 277 [58]. With the small ion chamber (Farmer chamber PTW type 30013), the equilibrium dose was directly measured by integrating the current from an ion chamber located at the fixed mid-point point in the phantom for the scanned length.

The dose equilibrium free in air ($D_{Eq.air}$) was obtain based on AAPM TG111 [10]:

$$D_{org,T} = D_{Eq.air} * \left(\left(\frac{\mu_{(en)}}{\rho} \right)^{tissue}_{air} \right) * \sum_{Z1}^{Z2} f(organ, Z) \text{ normalised to } D_{Eq} \qquad (5.4)$$

Organs dose estimations using the parameters in Table 5.1 and equation 5.4 were determined, and the organ dose results by D$_{Eq}$ method were derived by using D$_{Eq.air}$ and D$_{Eq}$ with IMPACT software , as well as using an organ dose conversion factor normalised to D$_{Eq}$.

5.3 Results and discussion

5.3.1 Comparison between planar average D_{Eq} and $CTDI_{vol}$

The D_{Eq} measurement was compared to the $CTDI_{vol}$ measurement for both the thoracic and the abdominopelvic protocols, as shown in Table 5.2. The D_{Eq} for the thoracic protocol was 54.7 mGy, while the $CTDI_{vol}$ was 42.5 mGy. The difference in these measurements represents a variation of 29%. For the abdominopelvic protocol, the D_{Eq} measurement was 15.7 mGy, while the $CTDI_{vol}$ was only 12.1 mGy. The difference in these measurements represents a variation of 30%, which is similar to the percentage variation seen in the thoracic dose measurements. These results indicate that in both cases, the dose delivered was underestimated when using the CTDI method[9,49].

Method	Thoracic (mGy)	Abdominopelvic (mGy)
D_{Eq}	54.7	15.7
$CTDI_{vol}$	42.5	12.1
Variation	29 %	30 %

Table 5. 2: Planer average D_{Eq} measurement compared with CTDI

5.3.2 Direct measurement

5.3.2.1 Organ dose measurements in Rando phantom using TLDs (Thoracic region)

Table 5.3 lists the direct measurements of patient dose grouped by organs associated with the thoracic region, i.e. the thyroid, lung, heart, and liver. The highest average dose (the average

of four separate measurements) was observed for the thyroid (116.0 mGy), followed by the

lung (84.4 mGy), then the heart (82.4 mGy). The lowest dosage in this organ group was

recorded for the liver (45.4 mGy). Of these results, the variability between a grouping of 4

TLD chip measurements was low (as indicated by standard deviations between 0.1-0.7 mGy).

Organs	Dose mGy	Mean mGy ± SD
Thyroid	116.8	116.0±0.7
	116.1	
	114.8	
	116.4	
Lung	85.1	84.4±0.5
	84.3	
	83.8	
	84.5	
Heart	82.4	82.4±0.2
	82.5	
	82.1	
	82.1	
Liver	45.3	45.5±0.1
	45.5	
	45.6	
	45.6	

Table 5. 3: Direct measurement TLD (Thoracic)

5.3.2.2 Organ dose measurements in Rando phantom using TLDs (Abdominopelvic region)

Table 5.4 illustrates the direct measurement of organ absorbed doses using TLD for the kidney,

bladder, prostate and testis in the abdominopelvic region. The highest absorbed dose average

(± SD) was for the testis (29.5±0.3 mGy) as opposed to the kidney, which was the lowest

(22.8±0.3 mGy). The average (± SD) absorbed doses for the prostate was 27.6±0.5 mGy, and
the bladder was 25.7±0.7 mGy.

Organs	Dose mGy	Mean mGy ± SD
Kidney	23.1	22.8±0.3
	22.4	
	22.9	
	22.8	
Bladder	24.9	25.7±0.7
	26.8	
	25.9	
	25.1	
Prostate	28.1	27.6±0.5
	27.4	
	28.0	
	26.8	
Testis	29.1	29.5±0.3
	29.5	
	29.8	
	29.5	

Table 5. 4: Direct measurement TLD (Abdominopelvic)

5.3.3 Direct measurement versus indirect measurement

5.3.3.1 Comparison between direct and indirect measurement approaches for the thoracic region organ groups

Table 5.5 illustrates the comparison of the average absorbed organ doses between the direct

measurement method TLD and the indirect CTDI and D_{Eq} methods for the thyroid, lung, heart and liver of the thoracic region. For the thyroid, the TLD was 116 mGy, the CTDI was 88 mGy, and the D_{Eq} was 111 mGy, which shows a difference of 24 % between TLD and CTDI, but a difference of only 4 % between TLD and D_{Eq}. The averages for the lung were 84 mGy (TLD), 64 mGy (CTDI) and 82 mGy (D_{Eq}), yielding a difference of 23 % between TLD and CTDI, but a difference of the only 2 % between TLD and D_{Eq}. The heart average absorbed doses were 82 mGy (TLD), 62 mGy (CTDI) and 81 mGy (D_{Eq}), yielding a difference of 24 % between TLD and CTDI, but a difference of only 1 % between TLD and D_{Eq}. The liver average absorbed doses were 46 mGy (TLD), 31 mGy (CTDI) and 43 mGy (D_{Eq}), yielding a difference of 32 % between TLD and CTDI, but a difference of only 7 % between TLD and D_{Eq}. For all organs tested, the differences between TLD and CTDI ranged between 23 % and 32 %, which were higher than the differences between TLD and D_{Eq}, which ranged between just 1 % and 7 %.

| Organs | Indirect | | Direct | | |
	CTDI mGy	D_{Eq} mGy	TLD mGy	Diff (TLD & CTDI)	Diff (TLD & D_{Eq})
Thyroid	88	111	116	24%	4%
Lung	64	82	84	23%	2%
Heart	62	81	82	24%	1%
Liver	31	43	46	32%	7%
				Aver 26%	Aver 4%

Table 5. 5: Patient dose comparison between direct measurement and indirect measurements for the thoracic region

5.3.3.2 Comparison between direct and indirect measurement approaches for the abdominopelvic region organs

Table 5.6 provides comparison between direct and indirect measurement approaches for the abdominopelvic region organs. Similarly, the observed difference between TLD and D_{Eq} is lower in all cases (7% on average) than TLD and CTDI (29% on average). The maximum

differences are also consistent with this trend, as 9% was observed for D_{Eq} vs. TLD, and 35% for CTDI vs. TLD (both for the kidney).

Organs	Indirect		Direct		
	CTDI mGy	D_{Eq} mGy	TLD mGy	Diff (TLD & CTDI)	Diff (TLD & D_{Eq})
Kidney	15	21	23	35%	9%
Bladder	20	24	26	23%	8%
Prostate	20	26	28	28%	7%
Testis	21	28	29	28%	3%
				Aver 29%	Aver 7%

Table 5. 6: Patient dose comparison between direct measurement and indirect measurements for abdominopelvic region

5.4 Conclusions

With the new generation of CT scanners utilising helical scanning mode and increased beam width and depth with associated increased detector size, the use of CTDI is no longer appropriate. The continued use of CTDI in dose estimation presents a greater risk to patient safety.

The two different techniques for indirect dose measurement, CTDI and D_{Eq}, when compared to direct measurements using the Rando phantom further reinforces the AAPM TG111 report. The indirect method for both CTDI and D_{Eq} techniques varied; in the thoracic region by 26% and 4%, respectively, and in the abdominopelvic region by 29% and 7%, respectively.

Direct dose measuring values using the Rando phantom were higher than the indirect dose values[65,80] in accordance with the previous underestimations by CTDI techniques as compared to TLD measurements. Moreover, the direct measurements of CT dose in a Rando phantom can be 40% higher than the results using the indirect technique [97].

From the experimental results, which display some variance, the measurements observed using the D_{Eq} approach were much closer to the direct TLD measurements than the CTDI indirect measurements, which were significantly lower in all cases. If the direct measurement is considered to represent the truest dose, then the findings of this study suggest that the CTDI technique results in gross underestimates of the actual dose present in organs, while D_{Eq} represents a more accurate estimate, falling only slightly short of the direct value in many cases.

In conclusion, it can be seen from the results that the characterization of dose through the use of CTDI is insufficient and inaccurate for modern CT machines. The results exhibited significant error in the characterisation of dose profiles, and implementing the new method outlined by the AAPM Task group report No. 111 [10] is key to more accurately characterising the dose profile from modern CT scanners. This method is relatively simple to follow and can be adapted to different phantom designs for determination of D_{Eq}. The D_{Eq} method, therefore, is a simple, standardised measure of the dose output of the CT scanner that can be used for quality assurance.

Chapter 6 (Dose equilibrium correction of past patient data to estimata effective annual dose in patient population)

6.1 Introduction

The use of CT is probably one of the most important advancements seen in diagnostic radiology. However, CT involves much higher doses of radiation when compared to standard radiography, which results in an increase in radiation exposure[98]. While CT scans provide significant medical benefits, their increased use has led to concerns about possible radiation induced cancer risks [99].

The effective dose is the most important CT quantity used to assess the risk of cancer from a procedure. It provides a means to compare risks for partial and whole-body exposures while integrating the various organ sensitivities to radiation[100].

Several factors affect the risk of cancer resulting from radiation exposure, such as the patient's age and gender, as well as the body part exposed. A conservative approach to radiation protection, called the linear non-threshold model, assumes that the risk for detrimental cancer is proportional to the radiation dose absorbed, although no amount of radiation is entirely risk-free[101].

It is important to estimate the quantity of patient dose accurately as any increase also increases the probability of inducing future cancers [102]. Therefore, patient CT dosimetry was established to establish guidance or diagnostic reference levels along with dosimetry parameters for the equipment.

CT dosimetry usually utilises an ionization chamber that is 100 mm long. However, it underestimates the equilibrium dose that is approached for clinically relevant body scan lengths of 250 mm or more[48]. This limitation occurs because the integration length of a 100 mm pencil chamber is too short to enclose the axial dose profile as it has scatter tails that extend beyond the CTDI phantom. The AAPM [10] suggested using a helical scan to transverse a phantom greater than 250 mm with a short ion chamber through the CT beam plane. This alternative method would collect the same integral as that of a pencil chamber by integrating over its arbitrary length.

In this chapter, the AAPM [10] D_{Eq} method and the CTDI method were applied to estimate organ dose and effective dose values and retrospectively corrected the annual effective patient dose for a random sample of twenty patients.

6.2 CTDI$_{vol}$ versus D$_{Eq}$ with different kV, mAs and scanning lengths

Twenty anonymous patients were randomly sampled to obtain CTDI$_{vol}$ procedural and rescan annual reports. Each patient specific CTDI$_{vol}$ was retrospectively corrected to planar average D_{Eq} using Tables 6.1, 6.2, 6.3 and Figure 6.1, all of which characterise the specific CT system of this study.

The planar average D_{Eq} and CTDI$_{vol}$ at various clinically relevant kV and mA ranges, as well as the different scanning lengths shown in Tables 6.1, 6.2 and 6.3, were measured to obtain these corrections. The D_{Eq}, CTDI$_{vol}$ and scanning lengths were plotted relative to each other using in-house MATLAB software. The MATLAB software was also used to procure a standard fit to estimate D_{Eq} measurements for any given CTDI$_{vol}$ in the system within a clinically relevant range, as shown in Figure 6.1.

The MATLAB software can be used to estimate the D_{Eq} for a given $CTDI_{vol}$ within the standard CT range for the CT system, while allowing for the retrospective correction of reported patient $CTDI_{vol}$.

Scan Length	250 mm	
kV, mA	$CTDI_{vol}$ (mGy)	D_{Eq} ±SD (mGy)
kV 80, mA 50	2.6	3.4±0.05
kV 80, mA 100	5.2	6.6±0.05
kV 100, mA 150	14	16.9±0.05
kV 100 mA 250	23.3	27.6±0.1
kV 120, mA 200	28.3	33.5±0.1

Table 6. 1:CTDI$_{vol}$ and D$_{Eq}$ based on different kV and mA at 250 mm scan length

Scan Length	350 mm	
kV, mA	$CTDI_{vol}$ (mGy)	D_{Eq} ±SD (mGy)
kV 80, mA 50	2.6	3.5±0.05
kV 80, mA 100	5.2	6.8±0.05
kV 100, mA 150	14	17.5±0.05
kV 100 mA 250	23.3	28.7±0.1
kV 120, mA 200	28.3	34.8±0.1

Table 6. 2: CTDI$_{vol}$ and D$_{Eq}$ based on different kV and mA at 350 mm scan length

Scan Length	450 mm	
kV, mA	$CTDI_{vol}$ (mGy)	D_{Eq} ±SD (mGy)
kV 80, mA 50	2.6	3.5±0.05
kV 80, mA 100	5.2	6.9±0.05

kV 100, mA 150	14	17.7±0.05
kV 100 mA 250	23.3	29.1±0.1
kV 120, mA 200	28.3	35.2±0.05

Table 6. 3: CTDI$_{vol}$ and D$_{Eq}$ based on different kV and mA at 450 mm scan length
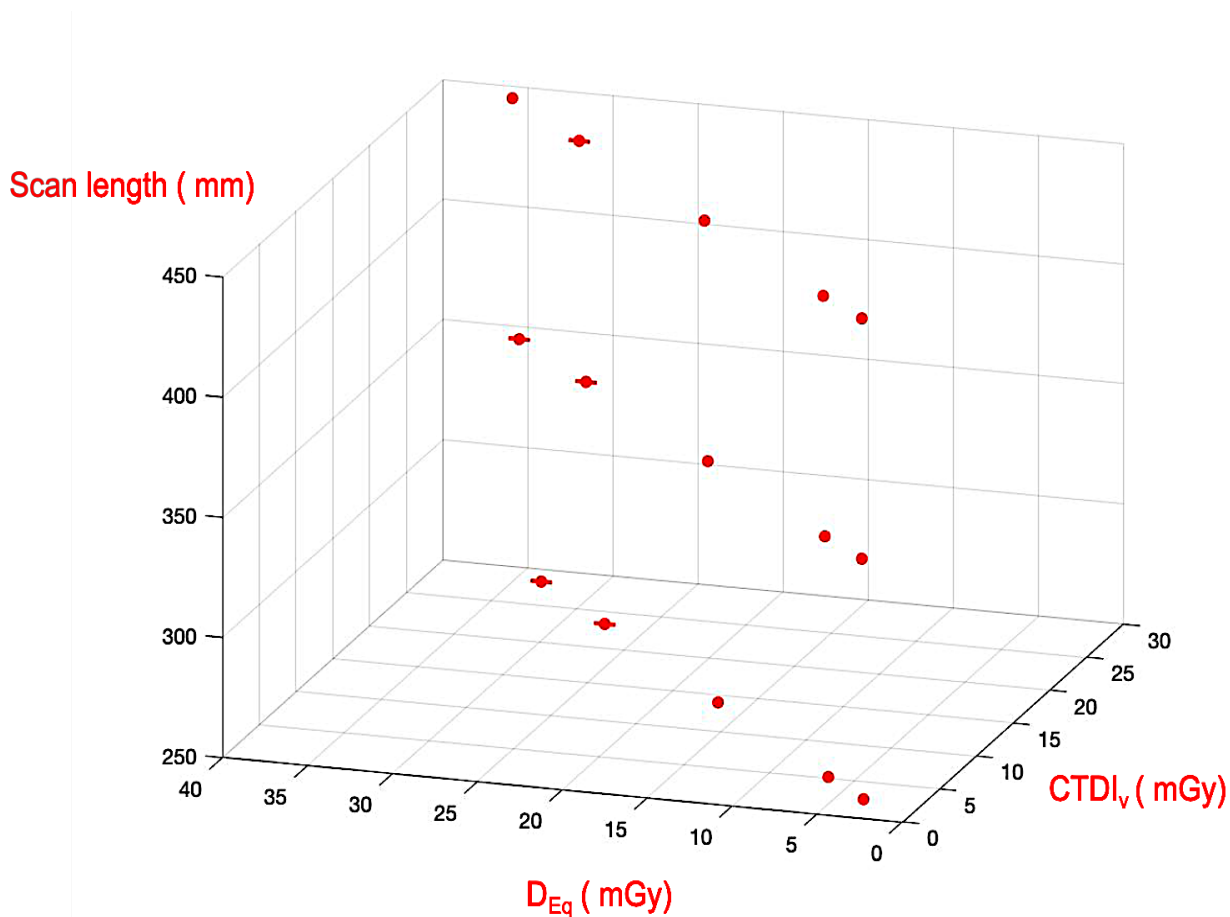
Figure 6. 1: Relationship of D$_{Eq}$, CTDIvol and scanning length with standard deviation

6.3 Correcting Past Patient Data to Dose Equilibrium

The MATLAB software was used to estimate D$_{Eq}$ for the performed procedure (Table 6.1, Table 6.2, Table 6.3 and Figure 6.1). This revealed that, over the course of several scans, the

random patient sample received an absorbed dose anywhere from 4 mGy to 12 mGy greater than previously estimated by CTDI$_{vol}$.

Table 6.4 includes the 20 patients who were used to compare estimations of absorbed doses from CTDI and D$_{Eq}$ over a period of one year. The study consisted of 9 female and 11 male patients. Two patients received one scan, twelve received two scans, three received three scans and three received four scans. The CTDI volume estimates ranged from a low of 14.9 mGy to a high of 49.3 mGy, while the D$_{Eq}$ estimates ranged from a low of 19.0 mGy to a high of 61.5 mGy. The differences between the two methods ranged from 4 mGy to 12.2 mGy, with the D$_{Eq}$ estimates being consistently higher than the CTDI volume estimates. Furthermore, when expressed as a percentage, the D$_{Eq}$ estimates were 22% to 28% higher in all cases.

Patient number	Number of scans	CTDI volume (mGy)	D$_{Eq}$ (mGy)	Absolute difference (mGy)	Percentage difference
Patient 1	3	26.4	33.5	7.1	27%
Patient 2	2	49.3	61.5	12.2	25%
Patient 3	2	16	20.4	4.4	28%
Patient 4	4	43.6	54.8	11.2	26%
Patient 5	2	14.9	19	4.1	28%
Patient 6	2	27	33	6	22%
Patient 7	2	32.1	40.2	8.1	25%
Patient 8	2	19	24.1	5.1	27%
Patient 9	1	15.8	19.8	4	25%
Patient 10	2	39.6	49.5	9.9	25%
Patient 11	2	18	23	5	28%
Patient 12	4	25.7	32.8	7.1	28%
Patient 13	2	14.9	19	4.1	28%
Patient 14	3	36.3	45.4	9.1	25%
Patient 15	3	39.4	48	8.6	22%
Patient 16	4	25.1	32.2	7.1	28%
Patient 17	2	18.8	23.9	5.1	27%
Patient 18	2	16.8	21.4	4.6	27%
Patient 19	2	29.4	36.8	7.4	25%
Patient 20	1	18.2	22.8	4.6	25%

Table 6. 4:Patient data set with updated estimated absorbed doses

An example of an individual male patient undergoing prostate imaging is shown in Table 6.5, broken down by each scan as well as summed over all scans performed throughout the year. This process was performed for all patients among the sample whose scan protocol was torso or pelvic.

MATLAB software was used to estimate the D_{Eq} for the four scans received by Patient 4. In scan 1 for Patient 4, the $CTDI_{vol}$ was estimated at 2.9 mGy, while the D_{Eq} was estimated as 3.8 mGy, a difference of 31%. The procedure to measure the D_{Eq} for all patient scans is shown in Appendix 1 (Second Code) as exemplified with the four scans for Patient 4. In scan 2, the $CTDI_{vol}$ was estimated at 6.2 mGy while the D_{Eq} was estimated at 7.8 mGy, a difference of 26%. Scan 3 measurements produced a difference of 24%, with the $CTDI_{vol}$ and D_{Eq} at 24.1 mGy and 29.9 mGy, respectively. An identical difference of 28% was calculated for Scan 4, with the $CTDI_{vol}$ and D_{Eq} at 10.4 mGy and 13.3 mGy, respectively. For all four scans, 43.6 mGy was the total for the $CTDI_{vol}$, and 54.8 mGy was the total for the D_{Eq}. In all instances, the CTDI values underestimated the dose as compared to the D_{Eq} measurement. The total of all four scans was in the same range at 26 %. Figure 6. 2 illustrates the planar average equilibrium doses in four scans for Patient 4. Similar results were obtained for the other 19 patients analysed in this study. The scans for these patients can be found in Appendix 2 (Absorbed Dose for all patients**)**
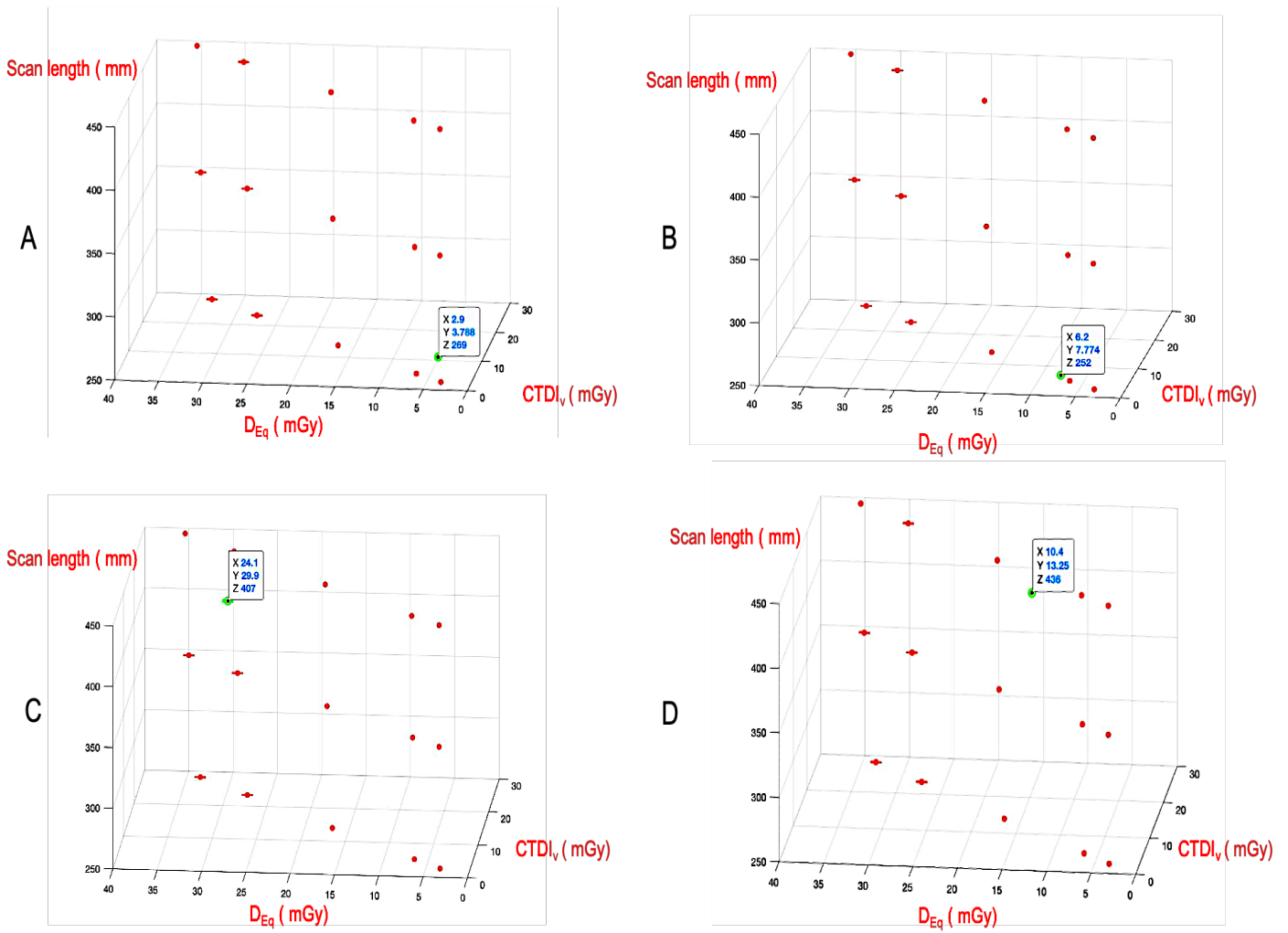
Figure 6. 2: A) D_{Eq} in first scan for Patient 4, B) D_{Eq} in second scan for Patient 4, C) D_{Eq} in third scan for Patient 4, D) D_{Eq} in fourth scan for Patient 4

Patient number	Scan	Scan length (mm)	CTDI volume (mGy)	D_{Eq} (mGy)	Percentage difference
Patient 4	1	269	2.9	3.8	31%
	2	252	6.2	7.8	26%
	3	407	24.1	29.9	24%
	4	436	10.4	13.3	28%
Total			43.6	54.8	26%

Table 6. 5: Patient 4 updated absorbed dose

90

6.4 Effective dose comparison between D_{Eq} and CTDI method for patients

The organ doses for both methods were obtained from IMPACT software, which uses CTDI and D_{Eq} values as described in Chapter 4. In addition, tissue weighting factors were used to calculate effective dose of affected organs for both modalities, and the sums over all scans were compared. The calculations were done according to ICRP 103 [85].

Table 6.6 illustrates the total of 20 patients from UHG that were used to compare estimations of effective doses using the CTDI and D_{Eq} methods. The CTDI estimates ranged from a low of 3.2 mSv to a high of 22.8 mSv, while the D_{Eq} estimates ranged from a low of 4.2 to a high of 28.5 mSv. The differences between the two methods ranged from 1 mSv to 5.7 mSv, with the D_{Eq} estimates being consistently higher than the CTDI estimates. Furthermore, when expressed as a percentage, the D_{Eq} estimate was 24% to 31% higher in all cases. Therefore, the CTDI method underestimated the effective dose when compared to the D_{Eq} method for all patients. This updated data set reflected that the effective dose to patients was as much as 6 mSv greater than previously estimated through CTDI.

Patient number	Scan No.	Effective dose (CTDI) mSv	Effective dose (D_{Eq}) mSv	Absolute difference (mSv)	Percentage difference
Patient 1	3	7.6	9.8	2.2	28%
Patient 2	2	17.6	21.8	4.2	24%
Patient 3	2	9	11.4	2.4	27%
Patient 4	4	13.4	16.7	3.3	25%
Patient 5	2	8.9	11.4	2.5	28%
Patient 6	2	5.9	7.4	1.5	25%
Patient 7	2	10.7	13.3	2.6	24%
Patient 8	2	10.1	12.8	2.7	27%
Patient 9	1	8.3	10.6	2.3	28%
Patient 10	2	22.8	28.5	5.7	25%
Patient 11	2	3.2	4.2	1	31%
Patient 12	4	6.9	9	2.1	30%

Patient 13	2	8.5	10.8	2.3	27%
Patient 14	3	10.7	13.7	3	28%
Patient 15	3	8.7	10.9	2.2	25%
Patient 16	4	7.9	10.1	2.2	28%
Patient 17	2	5.8	7.5	1.7	29%
Patient 18	2	9.7	12.5	2.8	28%
Patient 19	2	14.7	18.3	3.6	25%
Patient 20	1	11.4	14.2	2.8	25%

Table 6. 6: Patient data set with updated effective doses estimations

An example of an individual male patient undergoing prostate imaging treatments is shown in Table 6.7, broken down by organs affected as well as summed over all scans performed throughout the year. This process was performed for all patients among the sample whose scan protocol was torso or pelvic.

Patient 4, one of the 20 patients from UHG received four prostate scans over a period of one year and can be used as an example to demonstrate the differences in estimations when using the CTDI and D_{Eq} methods for effective doses

Organs	WT	Organ dose (CTDI)	Contribution to Effective Dose (CTDI)	Organ dose (D_{Eq})	Contribution to Effective Dose (D_{Eq})
Scan 1 (269 mm)					
Gonads	0.08	2.9	0.2	3.7	0.3
Bladder	0.04	4	0.2	5.2	0.2
Prostate	0.00923	4	0.04	5.2	0.1
Colon	0.12	1	0.1	1.3	0.2
Spleen	0.00923	0.0068	0.0001	0.0088	0.0001
Kidney	0.00923	0.017	0.0002	0.022	0.0002
Pancreas	0.00923	0.0081	0.0001	0.011	0.0001
Effective dose			**0.5**		**0.8**
Scan 2 (252 mm)					
Gonads	0.08	5.8	0.5	7.3	0.6
Bladder	0.04	7.1	0.3	8.9	0.4
Prostate	0.00923	7.1	0.1	8.9	0.1
Colon	0.12	1.8	0.2	2.2	0.3

Organ					
Spleen	0.00923	0.0091	0.0001	0.011	0.0001
Kidney	0.00923	0.023	0.0002	0.03	0.0003
Pancreas	0.00923	0.011	0.0001	0.014	0.0001
Effective dose			**1.1**		**1.4**
Scan 3 (407 mm)					
Gonads	0.08	35	2.8	44	3.5
Bladder	0.04	39	1.6	48	1.9
Prostate	0.00923	39	0.4	48	0.44
Colon	0.12	27	3.2	33	3.9
Spleen	0.00923	1.2	0.01	1.5	0.01
Kidney	0.00923	2.9	0.03	3.6	0.03
Pancreas	0.00923	1.2	0.01	1.5	0.01
Effective dose			**8.1**		**9.8**
Scan 4 (436 mm)					
Gonads	0.08	15	1.2	20	1.6
Bladder	0.04	17	0.7	22	0.9
Prostate	0.00923	17	0.2	22	0.2
Colon	0.12	13	1.6	17	2
Spleen	0.00923	1	0.01	1.3	0.01
Kidney	0.00923	3.3	0.03	4.2	0.04
Pancreas	0.00923	1	0.01	1.3	0.01
Effective dose			**3.7**		**4.7**
Total of Effective dose in 4 scans			**13.4**		**16.7**

Table 6. 7: Patient 4 updated effective doses

In the first scan, the contribution to effective dose for the gonads was the highest of any of the organs at 0.2 mSv using the CTDI method and at 0.3 mSv using the D_{Eq} method. The next highest effective dose estimation was for the bladder at 0.2 mSv for both the CTDI method and the D_{Eq} method. The colon was estimated to receive slightly lower effective doses for these same tests at 0.1 mSv and 0.2 mSv, respectively. Taking into consideration all organs, which further include the spleen, kidney and pancreas, they contributed 0.5 mSv and 0.8 mSv to the total effective dose based on the CTDI method and the D_{Eq} method, respectively.

Contribution to effective doses estimated for the organs during the first prostate scan were also estimated for the second prostate scan of patient 4. In the second scan, the gonad's contribution

to effective dose estimations varied between the two methods, being 0.5 mSv for the CTDI method and 0.6 mSv for the D_{Eq} method. In addition, the bladder had estimates for the CTDI method at 0.3 mSv and for D_{Eq} at 0.4. All organs affected by Scan 2 contributed 1.1 mSv and 1.4 mSv to the total effective dose using the CTDI method and the D_{Eq} method, respectively.

Patient 4 received a third scan in which the estimated of contribution to effective dose for the colon and the gonads were 3.2 mSv and 2.8 mSv using the CTDI method and 3.9 mSv and 3.5 mSv using the D_{Eq} method, respectively.

Patient 4 received a final scan of the prostate, in which the contribution to effective dose estimated for the colon and the gonads was 1.6 mSv and 1.2 mSv using the CTDI method and 2.0 mSv and 1.6 mSv using the D_{Eq} method, respectively. The bladder had an estimated effective dose of 0.7 mSv for the CTDI method and 0.9 mSv for the D_{Eq} method, while the prostate had an estimated effective dose of 0.2 mSv for both methods, respectively. All organs affected by scan 4 contributed 3.7 mSv and 4.7 mSv to the total effective dose using the CTDI method and the D_{Eq} method, respectively.

Taking all four scans of the prostate into consideration for patient 4, he was estimated to have received a total contribution to the effective dose of 13.4 mSv using the CTDI method, and 16.7 mSv using the D_{Eq} method. Therefore, the CTDI method underestimated the contribution to the effective dose as compared to the D_{Eq} method. Similar results were obtained for the other 19 patients analysed in this study. The scans for these patients can be found in Appendix 2 (Effective Dose for all patients)

6.5 The relation between the dose and the scanning length

A scan length of 250 or greater produced a small difference in the estimation of the planar average D_{Eq} of the phantom as shown in Tables 6.1, 6.2, 6.3 and Figure 6.3. In this study, the doses at kV 80, mA 50, was 3.4 mGy for a 250 mm scanning length and 3.5 mGy for both a 350 mm and a 450 mm scanning length. At kV 80, mA100, the dose was 6.6 mGy for a 250 mm scanning length, 6.8 mGy for a 350 mm scanning length, and 6.9 mGy for a 450 mm scanning length. Results at kV 100, mA 150 were 16.9 mGy for a 250 mm scanning length, 17.5 mGy for a 350 mm scanning length, and 17.7 mGy for a scan length of 450 mm. At kV 100, mA 250, the dose was 27.6 mGy at a scanning length of 250 mm, 28.7 mGy at 350 mm, and 29.1 mGy at 450 mm. Finally, at kV 120, mA 200, the dose was 33.5 mGy at a length of 250 mm, 34.8 mGy at 350 mm, and 35.2 mGy at 450 mm. The difference in dose between 250 mm and 450 mm was 3% for kV 80, mA 50, 5% for both kV 80, mA 100 and kV 100, mA 150 and 6% for both kV 100, mA 250 and kV 120, mA 200.
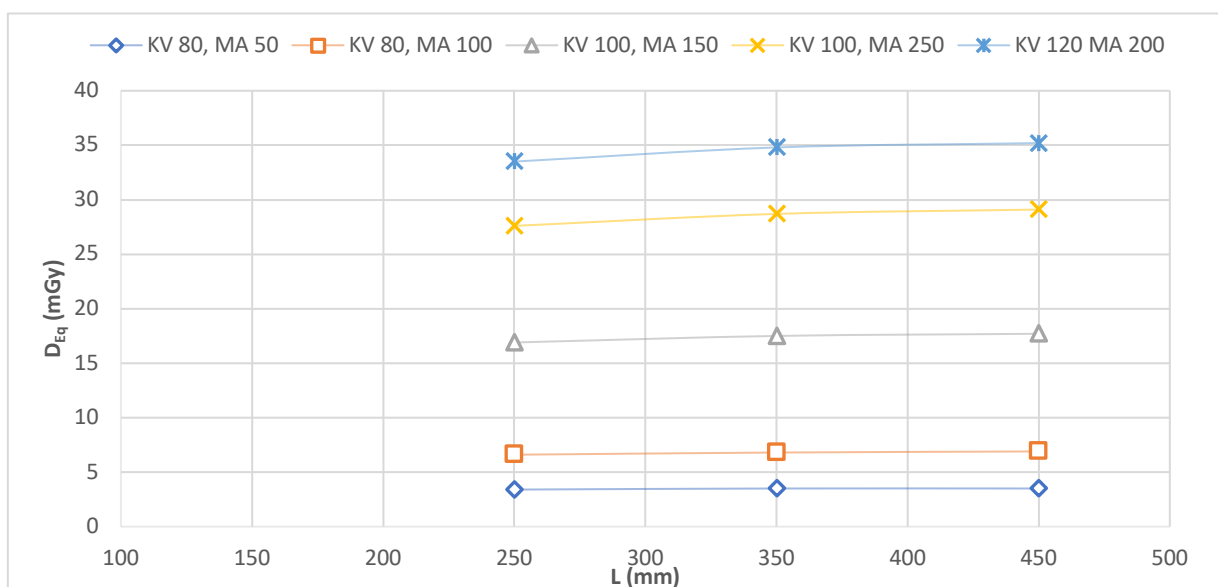
Figure 6. 3: Relationship between the planar average equilibrium dose and scanning length

Additionally, three different studies were in a good agreement with these results regarding the relationship between the equilibrium dose and scanning length. The three graphs shown in Figures 6.4 are from different studies. All three graphs depict the relationship between dose and scanning length when measuring the dose in the centre and the periphery of the phantom against a scanning length.

Figure 6.4 (A) is a graph from a study conducted by Campeloa, Silvab and Terinic (2016) [50]. As shown in the figure, for the phantom centre, the dose at a 250 mm scanning length was approximately 23 mGy and at a 450 mm scanning length was almost 25 mGy. For the periphery of the phantom, the dose at a 250 mm scanning length was almost 35.9 mGy and at a 450 mm scanning length was approximately 37.9 mGy. There was no great disparity between the doses at a 250 mm scan length and a 450 mm scan length as they differed by only 8% for the phantom centre and 5% for the phantom periphery. Regarding the planar average D_{Eq} of the phantom centre and periphery assessed together, the difference in dose between 250 mm and 450 mm was 6%.
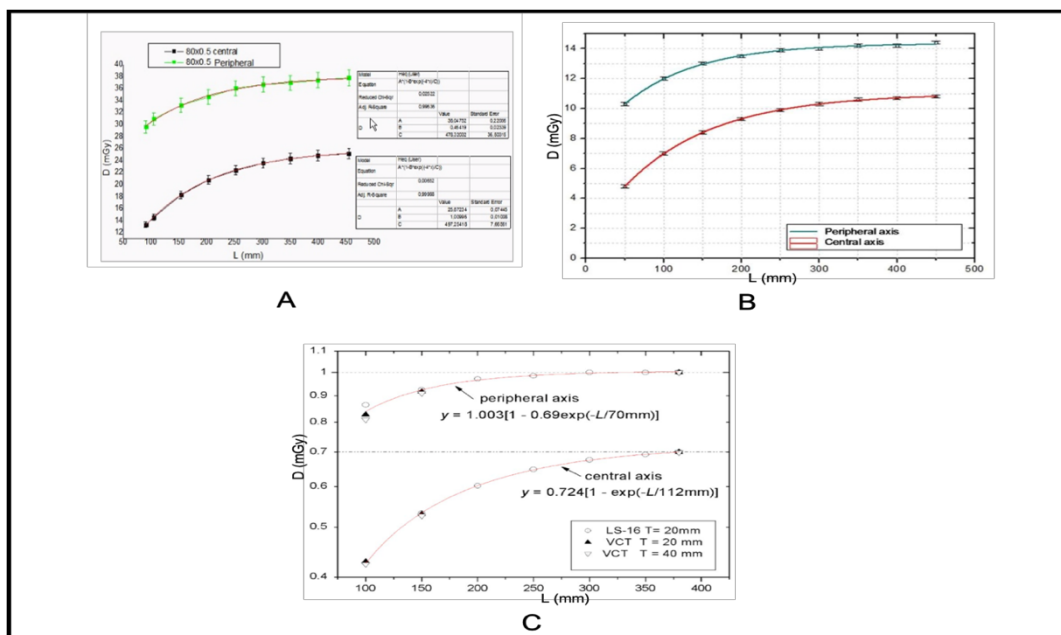
Figure 6. 4: Approach to equilibrium of Cumulative Dose in central and peripheral axis. A) Study by Campeloa, Silvab and Terinic (2016) [50], B)Study by by Descamps et al. (2012) [49], C) Study by Robert L. Dixon and Adam C. Ballard (2007) [48]

Figure 6.4 (B) is a graph from a study conducted by Descamps et al. (2012) [49], which also shows the dose relative to the scanning length. For the centre scans, the dose at a scan length of 250 mm was almost 9.9 mGy, while the dose at a scan length of 450 mm was approximately 10.9 mGy. For the peripheral scans, the dose at a scan length of 250 mm was almost 13.9 mGy, while the dose at a scan length of 450mm was approximately 14.8 mGy. There was no great disparity between the doses at a 250 mm scan length and a 450 mm scan length as they differed by only 9% for the phantom centre and 6% for the phantom periphery. Regarding the planar average D_{Eq} of the centre and periphery together, the difference in dose between 250 mm and 450 mm was 7%.

Figure 6.4 (C) shows the results of another study, which was conducted by Dixon and Ballard (2007) [48]. Their findings also showed there was just a small difference between scans at 250 mm and beyond. For the phantom centre, the dose at a 250 mm scanning length was approximately 0.65 mGy and at a 450 mm scanning length was almost 0.7 mGy. For the periphery of the phantom, the dose at a 250 mm scanning length was almost 0.98 mGy and at a 450 mm scanning length was approximately 1 mGy. The difference between the doses at a 250 mm scan length and a 450 mm scan length was only 7% for the phantom centre and 2% for the phantom periphery. Regarding the planar average D_{Eq} of the centre and periphery together, the difference in dose between 250 mm and 450 mm was 4%.

From these three studies, there were no significant differences between the 250 mm and 450 mm scan lengths. Therefore, for a finite scanning length of 250 mm or greater, a longer range produces a negligibly small difference in the estimation of dose equilibrium.

6.6 Conclusion

The CTDI absorbed dose as determined by the CT scanner was underestimated by 22% to 28% when compared to the D_{Eq} method. Moreover, the effective doses by CTDI for patients sampled at UHG was similarly underestimated by 24% to 31% when compared to the D_{Eq} method. The data, therefore, revealed that patients who underwent several scans in a single year would receive an effective dose up to 6 mSv greater than the CTDI estimate.

Chapter 7

Chapter 7 provides a summary of the work presented in this thesis, the results obtained , the clinical implication and the future work.

7.1 Conclusions

The Organization for Economic Co-operation and Development (OECD) reported that in the United States, more than 73 million CT scans were performed in 2017. As CT scans account for half of all medical radiation exposure in the United States [103], strictly monitored and accurate estimations of absorbed doses are essential.

Both absorbed and effective doses result from primary radiation as well as scattered radiation received from nearby tissues. Moreover, CTDI is used to determine CT quality assurance (QA) measurements and dose measurements, being the absorbed dose along the longitudinal axis (z-axis) during a single X-ray source rotation [104]. This measurement is usually conducted in a cylindrical phantom using a 100 mm ionization chamber. However, the chamber is responsible for significant error in the dose profiles as it does not take into account some of the radiation scattered beyond the relatively short (100-mm) range of integration along the z-axis[8,9]. This error is mostly due to over-beaming in multi slice CT where the z collimation of the source radiation is broadened to achieve umbra-region incidence uniformly across detectors.

Due to the increase of the detection system size along the z-axis, CT beams became larger, and much of the radiation not utilized by the detectors is incident on the patient. The more recent generations of CT scanners provide helical scanning mode or cone-beam irradiation

geometries; however, the pencil chambers in these scenarios are too short to completely measure the radiation.

The AAPM Task Group Report No. 111[10] outlined a new method of measurement derived from CTDI using a small volume ionization chamber in a cylindrical water phantom that is long enough to determine dose equilibrium. With this dose equilibrium measurement, we acquire a value sufficiently equivalent to both the primary and scatter radiation present from the beam.

The initial proof of concept phase from this thesis was to perform a new dose estimation of the CT scanner system, based on the D_{Eq} method. This methodology allows measurements of the accumulated dose for any clinical scan length, thus providing measurement of the equilibrium dose. Using the new methodology, it was determined that the CTDI approach can underestimate the dose by 25% to 35%; furthermore, all of the dose values from the water phantom and Farmer chamber were independently verified with TLD measurements.

 The second phase of the research used the D_{Eq} and CTDI methods to estimate organ dose values indirectly and the Alderson Rando phantom embedded with TLDs to directly estimate organ dose. Both indirect methods were compared against the direct method. The results indicated D_{Eq} provided estimations of organ dose that varied less than CTDI when compared to direct TLD organ dose measurements in anatomical regions, by 22% in both regions (thoracic and abdominopelvic)

In the final phase, the retrospective correction was applied to patient CTDIs by characterising the specific D_{Eq} profile of the system scans, and the effective doses of 20 anonymous patients were retrospectively corrected. The results showed that the effective dose summed across the affected organs was underestimated between 24 % to 31% by CTDI when compared to the D_{Eq} estimate. This updated data set reflected that the effective dose to patients was up to 6 mSv greater than previously estimated through CTDI.

The results of the three phases illustrated that continued use of the CTDI method in quality assurance of modern CT could result in greater patient risk. The AAPM TG111 [10] presents a more accurate, safer method to estimate dose and its adoption is paramount.

7.2 Future plan

This thesis, which focused on the CTDI and D_{Eq} methods, required the construction of a special phantom for measurements using D_{Eq}. The results of the study showed that the CTDI method underestimated the absorbed dose when compared to the D_{Eq} method, which is in agreement with previous studies that were reviewed. The research presented in this thesis has led to the identification of several areas of future study in which developments are likely to be beneficial in CT dosimetry.

The D_{Eq} phantom can be used with different CT scanner models to characterise various CT scanning modes and models. Each CT scanner model could be characterised by calculating the D_{Eq} and $CTDI_{vol}$ at different kV and mA settings and creating a lookup table by fitting a bilinear regression to extrapolate a standard fit to estimate D_{Eq} measurements for any given $CTDI_{vol}$.

In addition, software to estimate the organ dose using the D_{Eq} method instead of the CTDI method could be developed or used as an update for the existing predictor software for the CTDI method, e.g., IMPACT [86], CT Imaging and CT-EXPO. [87]

Furthermore, future phantom development will be focused on incorporating automatic exposure control (AEC) measurement capabilities into the phantom design. An AEC system for CT allows for adjustment of the x-ray current to compensate for various attenuation levels

of the scanner's beam, which then reduces variation in radiation doses due to different sized patients. Presently, this is achieved by controlling the current to reduce image noise. Therefore, a phantom is being designed to test patient size and z-axis aspects of AEC systems.

The phantom is being planned with two chambers, as shown in figure 7.1, to allow for both D_{Eq} and AEC measurements in one phantom. A cylinder chamber will provide the D_{Eq} measurement, and an oval chamber will provide the AEC measurement inside the cylinder chamber
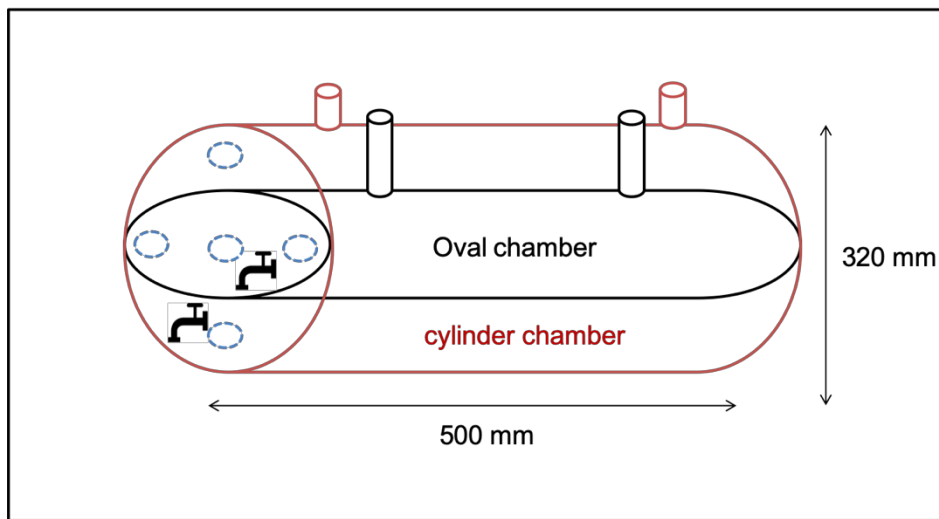
Figure 7. 1: Diagram of AEC and D_{Eq} phantom

This design will allow the use of a Farmer chamber for both measurements, and both chambers can be filled with water. Therefore, when the D_{Eq} is being measured, both the cylinder chamber and the oval chamber will be filled with water, but when the AEC is being measured, only the oval chamber will be filled.

Appendix 1

First Code

This code was used to find the Relationship of D_{Eq}, $CTDI_{vol}$ and scanning length. Furthermore, the code was used to show the error bar for D_{Eq} values (The error bars for all D_{Eq} values are difficult to see in the graph, so they were all multiplied by 5 to improve visibility)

```matlab
% x= CTDIv
x=[2.6,5.2,14,23.3,28.3,2.6,5.2,14,23.3,28.3,2.6,5.2,14,23.3,28.3 ];
% y= planar average equilibrium dose (DEq)
y=[3.5,6.9,17.7,29.1,35.2,3.5,6.8,17.5,28.7,34.8,3.4,6.6,16.9,27.6,33.5 ];
% z= scanning length
z=[450,450,450,450,450,350,350,350,350,350,250,250,250,250,250];
% ysd= DEq standard deviation
ysd = [0.047140452, 0.047140452, 0.047140452, 0.124721913, 0.047140452,
0.047140452, 0.047140452, 0.047140452, 0.124721913, 0.124721913,
0.047140452, 0.047140452, 0.047140452, 0.124721913, 0.124721913];

xr = reshape(x, [], 3);
yr = reshape(y, [], 3);
zr = reshape(z, [], 3);
ysdr = reshape(ysd, [], 3)*5;

%for visualisation
figure
hold on
for k1 = 1:size(xr,2)
    for k2 = 1:size(xr,1)
    plot3((xr(k2,k1)*[1 1]), (yr(k2,k1)+ysdr(k2,k1)*[-1 1]), (zr(2,k1)*[1
1]), '-r', 'LineWidth',1.7)
    plot3((xr(k2,k1)), (yr(k2,k1)), (zr(2,k1)), '.r', 'MarkerSize',15)
    end
end
hold off
view(-60,30)
grid on
```

Second Code

This code was used to find the D_{Eq} for 20 patients who were already associated with different $CTDI_v$ and scanning length. This code was also used to estimate the error bar for D_{Eq} values for each patient (The error bars for all D_{Eq} values are difficult to see in the graph, so they were all multiplied by 5 to improve visibility)

Patient 4 , scan 1

```
% x= CTDIv
x=[2.6,5.2,14,23.3,28.3,2.6,5.2,14,23.3,28.3,2.6,5.2,14,23.3,28.3 ];
% y= planar average equilibrium dose (DEq)
y=[3.5,6.9,17.7,29.1,35.2,3.5,6.8,17.5,28.7,34.8,3.4,6.6,16.9,27.6,33.5 ];
% z= scanning length
z=[450,450,450,450,450,350,350,350,350,350,250,250,250,250,250];
% ysd= DEq standard deviation
ysd = [0.047140452, 0.047140452, 0.047140452, 0.124721913, 0.047140452,
0.047140452, 0.047140452, 0.047140452, 0.124721913, 0.124721913,
0.047140452, 0.047140452, 0.047140452, 0.124721913, 0.124721913];

xr = reshape(x, [], 3);
yr = reshape(y, [], 3);
zr = reshape(z, [], 3);
ysdr = reshape(ysd, [], 3)*5;

%calculate y knowing x and z
YfromXZ = scatteredInterpolant(x(:), z(:), y(:));
queryx = 2.9;
queryz = 269;
YfromXZ.ExtrapolationMethod = 'linear';
matchingy = YfromXZ(queryx, queryz);
figure;scatter3(x, y, z); hold('on'); plot3(queryx, matchingy, queryz,
'r*');
errYfromXZ = scatteredInterpolant(x(:), z(:), y(:)+ysd(:));
errYfromXZ.ExtrapolationMethod = 'linear';
matchingyerr = errYfromXZ(queryx, queryz);
errY = (matchingyerr - matchingy)

%for visualisation
figure
hold on
for k1 = 1:size(xr,2)
    for k2 = 1:size(xr,1)
    plot3((xr(k2,k1)*[1 1]), (yr(k2,k1)+ysdr(k2,k1)*[-1 1]), (zr(2,k1)*[1
1]), '-r', 'LineWidth',1.7)
    plot3((xr(k2,k1)), (yr(k2,k1)), (zr(2,k1)), '.r', 'MarkerSize',15)
    end
end
plot3(queryx*[1 1], matchingy+errY*[-1 1]*5, queryz*[1 1], '-g',
'LineWidth',3.4)
plot3(queryx, matchingy, queryz, '.g', 'MarkerSize',30)
hold off
view(-60,30)
grid on
```

Patient 4 , scan 2

```matlab
% x= CTDIv
x=[2.6,5.2,14,23.3,28.3,2.6,5.2,14,23.3,28.3,2.6,5.2,14,23.3,28.3 ];
% y= planar average equilibrium dose (DEq)
y=[3.5,6.9,17.7,29.1,35.2,3.5,6.8,17.5,28.7,34.8,3.4,6.6,16.9,27.6,33.5 ];
% z= scanning length
z=[450,450,450,450,450,350,350,350,350,350,250,250,250,250,250];
% ysd= DEq standard deviation
ysd = [0.047140452, 0.047140452, 0.047140452, 0.124721913, 0.047140452,
0.047140452, 0.047140452, 0.047140452, 0.124721913, 0.124721913,
0.047140452, 0.047140452, 0.047140452, 0.124721913, 0.124721913];


xr = reshape(x, [], 3);
yr = reshape(y, [], 3);
zr = reshape(z, [], 3);
ysdr = reshape(ysd, [], 3)*5;

%calculate y knowing x and z
YfromXZ = scatteredInterpolant(x(:), z(:), y(:));
queryx = 6.2;
queryz = 252;
YfromXZ.ExtrapolationMethod = 'linear';
matchingy = YfromXZ(queryx, queryz);
figure;scatter3(x, y, z); hold('on'); plot3(queryx, matchingy, queryz,
'r*');
errYfromXZ = scatteredInterpolant(x(:), z(:), y(:)+ysd(:));
errYfromXZ.ExtrapolationMethod = 'linear';
matchingyerr = errYfromXZ(queryx, queryz);
errY = (matchingyerr - matchingy)

%for visualisation
figure
hold on
for k1 = 1:size(xr,2)
    for k2 = 1:size(xr,1)
    plot3((xr(k2,k1)*[1 1]), (yr(k2,k1)+ysdr(k2,k1)*[-1 1]), (zr(2,k1)*[1
1]), '-r', 'LineWidth',1.7)
    plot3((xr(k2,k1)), (yr(k2,k1)), (zr(2,k1)), '.r', 'MarkerSize',15)
    end
end
plot3(queryx*[1 1], matchingy+errY*[-1 1]*5, queryz*[1 1], '-g',
'LineWidth',3.4)
plot3(queryx, matchingy, queryz, '.g', 'MarkerSize',30)
hold off
view(-60,30)
grid on
```

Patient 4 , scan 3

```matlab
% x= CTDIv
x=[2.6,5.2,14,23.3,28.3,2.6,5.2,14,23.3,28.3,2.6,5.2,14,23.3,28.3 ];
% y= planar average equilibrium dose (DEq)
y=[3.5,6.9,17.7,29.1,35.2,3.5,6.8,17.5,28.7,34.8,3.4,6.6,16.9,27.6,33.5 ];
% z= scanning length
z=[450,450,450,450,450,350,350,350,350,350,250,250,250,250,250];
% ysd= DEq standard deviation
ysd = [0.047140452, 0.047140452, 0.047140452, 0.124721913, 0.047140452,
0.047140452, 0.047140452, 0.047140452, 0.124721913, 0.124721913,
0.047140452, 0.047140452, 0.047140452, 0.124721913, 0.124721913];


xr = reshape(x, [], 3);
yr = reshape(y, [], 3);
zr = reshape(z, [], 3);
ysdr = reshape(ysd, [], 3)*5;

%calculate y knowing x and z
YfromXZ = scatteredInterpolant(x(:), z(:), y(:));
queryx = 24.1;
queryz = 407;
YfromXZ.ExtrapolationMethod = 'linear';
matchingy = YfromXZ(queryx, queryz);
figure;scatter3(x, y, z); hold('on'); plot3(queryx, matchingy, queryz,
'r*');
errYfromXZ = scatteredInterpolant(x(:), z(:), y(:)+ysd(:));
errYfromXZ.ExtrapolationMethod = 'linear';
matchingyerr = errYfromXZ(queryx, queryz);
errY = (matchingyerr - matchingy)

%for visualisation
figure
hold on
for k1 = 1:size(xr,2)
    for k2 = 1:size(xr,1)
    plot3((xr(k2,k1)*[1 1]), (yr(k2,k1)+ysdr(k2,k1)*[-1 1]), (zr(2,k1)*[1
1]), '-r', 'LineWidth',1.7)
    plot3((xr(k2,k1)), (yr(k2,k1)), (zr(2,k1)), '.r', 'MarkerSize',15)
    end
end
plot3(queryx*[1 1], matchingy+errY*[-1 1]*5, queryz*[1 1], '-g',
'LineWidth',3.4)
plot3(queryx, matchingy, queryz, '.g', 'MarkerSize',30)
hold off
view(-60,30)
grid on
```

Patient 4 , scan 4

```matlab
% x= CTDIv
x=[2.6,5.2,14,23.3,28.3,2.6,5.2,14,23.3,28.3,2.6,5.2,14,23.3,28.3 ];
% y= planar average equilibrium dose (DEq)
y=[3.5,6.9,17.7,29.1,35.2,3.5,6.8,17.5,28.7,34.8,3.4,6.6,16.9,27.6,33.5 ];
% z= scanning length
z=[450,450,450,450,450,350,350,350,350,350,250,250,250,250,250];
% ysd= DEq standard deviation
ysd = [0.047140452, 0.047140452, 0.047140452, 0.124721913, 0.047140452,
0.047140452, 0.047140452, 0.047140452, 0.124721913, 0.124721913,
0.047140452, 0.047140452, 0.047140452, 0.124721913, 0.124721913];


xr = reshape(x, [], 3);
yr = reshape(y, [], 3);
zr = reshape(z, [], 3);
ysdr = reshape(ysd, [], 3)*5;

%calculate y knowing x and z
YfromXZ = scatteredInterpolant(x(:), z(:), y(:));
queryx = 10.4;
queryz = 436;
YfromXZ.ExtrapolationMethod = 'linear';
matchingy = YfromXZ(queryx, queryz);
figure;scatter3(x, y, z); hold('on'); plot3(queryx, matchingy, queryz,
'r*');
errYfromXZ = scatteredInterpolant(x(:), z(:), y(:)+ysd(:));
errYfromXZ.ExtrapolationMethod = 'linear';
matchingyerr = errYfromXZ(queryx, queryz);
errY = (matchingyerr - matchingy)

%for visualisation
figure
hold on
for k1 = 1:size(xr,2)
    for k2 = 1:size(xr,1)
    plot3((xr(k2,k1)*[1 1]), (yr(k2,k1)+ysdr(k2,k1)*[-1 1]), (zr(2,k1)*[1
1]), '-r', 'LineWidth',1.7)
    plot3((xr(k2,k1)), (yr(k2,k1)), (zr(2,k1)), '.r', 'MarkerSize',15)
    end
end
plot3(queryx*[1 1], matchingy+errY*[-1 1]*5, queryz*[1 1], '-g',
'LineWidth',3.4)
plot3(queryx, matchingy, queryz, '.g', 'MarkerSize',30)
hold off
view(-60,30)
grid on
```

Appendix 2

Absorbed Dose for all patients

Patient 1

(Prostate , 3 scan)

Patient number	Scan	Scan length(mm)	CTDI volume (mGy)	D_{Eq} (mGy)	$(CTDI_v, D_{Eq})$ (Diff %)
Patient 1	1	254	3.1	4	29%
	2	420	12.4	15.7	27%
	3	359	10.9	13.8	27%
Total			**26.4**	**33.5**	**27%**

Table 7. 1:Patient 1 absorbed dose updated

Patient 2

(Rectum , 2 scan)

Patient number	Scan	Scan length(mm)	CTDI volume (mGy)	D_{Eq} (mGy)	$(CTDI_v, D_{Eq})$ (Diff %)
Patient 2	1	446	25.6	31.9	25%
	2	449	23.7	29.6	25%
Total			**49.3**	**61.5**	**25%**

Table 7. 2:Patient 2 absorbed dose updated

Patient 3

(Breast , 2 scan)

Patient number	Scan	Scan length(mm)	CTDI volume (mGy)	D_{Eq} (mGy)	$(CTDI_v, D_{Eq})$ (Diff %)
Patient 3	1	424	7.9	10.1	28%
	2	390	8.1	10.3	27%
Total			16	20.4	28%

Table 7. 3: Patient 3 absorbed dose updated

Patient 4

(Prostate , 4 scan)

Patient number	Scan	Scan length(mm)	CTDI volume (mGy)	D_{Eq} (mGy)	$(CTDI_v, D_{Eq})$ (Diff %)
Patient 4	1	269	2.9	3.8	31%
	2	252	6.2	7.8	26%
	3	407	24.1	29.9	24%
	4	436	10.4	13.3	28%
Total			43.6	54.8	26%

Table 7. 4: Patient 4 absorbed dose updated

Patient 5

(Breast, 2 scan)

Patient number	Scan	Scan length(mm)	CTDI volume (mGy)	D_{Eq} (mGy)	$(CTDI_v, D_{Eq})$ (Diff %)
Patient 5	1	447	7.4	9.4	27%
	2	423	7.5	9.6	28%
Total			14.9	19	28%

Table 7. 5: Patient 5 absorbed dose updated

Patient 6

(Pelvis , 2 scan)

Patient number	Scan	Scan length(mm)	CTDI volume (mGy)	D_{Eq} (mGy)	($CTDI_v$, D_{Eq}) (Diff %)
Patient 6	1	254	18	21.5	19%
	2	386	9	11.5	28%
Total			**27**	**33**	**22%**

Table 7. 6: Patient 6 absorbed dose updated

Patient 7

(Pelvis, 2 scan)

Patient number	Scan	Scan length(mm)	CTDI volume (mGy)	D_{Eq} (mGy)	($CTDI_v$, D_{Eq}) (Diff %)
Patient 7	1	449	16.7	21	26%
	2	380	15.4	19.2	25%
Total			**32.1**	**40.2**	**25%**

Table 7. 7: Patient 7 absorbed dose updated

Patient 8

(Breast, 2 scan)

Patient number	Scan	Scan length(mm)	CTDI volume (mGy)	D_{Eq} (mGy)	($CTDI_v$, D_{Eq}) (Diff %)
Patient 8	1	401	9.4	11.9	27%
	2	381	9.6	12.2	27%
Total			**19**	**24.1**	**27%**

Table 7. 8: Patient 8 absorbed dose updated

Patient 9

(Breast, 1 scan)

Patient number	Scan	Scan length(mm)	CTDI volume (mGy)	D_{Eq} (mGy)	(CTDI$_v$, D_{Eq}) (Diff %)
Patient 9	1	391	15.8	19.8	25%
Total			**15.8**	**19.8**	**25%**

Table 7. 9: Patient 9 absorbed dose updated

Patient 10

(Breast, 2 scan)

Patient number	Scan	Scan length(mm)	CTDI volume (mGy)	D_{Eq} (mGy)	(CTDI$_v$, D_{Eq}) (Diff %)
Patient 10	1	450	20.2	25.3	25%
	2	432	19.4	24.2	25%
Total			**39.6**	**49.5**	**25%**

Table 7. 10: Patient 10 absorbed dose updated

Patient 11

(Pancreas, 2 scan)

Patient number	Scan	Scan length(mm)	CTDI volume (mGy)	D_{Eq} (mGy)	(CTDI$_v$, D_{Eq}) (Diff %)
Patient 11	1	445	9	11.6	29%
	2	362	9	11.4	27%
Total			**18**	**23**	**28%**

Table 7. 11: Patient 11 absorbed dose updated

Patient 12

(Prostate, 4 scan)

Patient number	Scan	Scan length(mm)	CTDI volume (mGy)	D_{Eq} (mGy)	($CTDI_v$, D_{Eq}) (Diff %)
Patient 12	1	258	3.1	4	29%
	2	256	3.1	4	29%
	3	392	10	12.7	27%
	4	385	9.5	12.1	27%
Total			**25.7**	**32.8**	**28%**

Table 7. 12: Patient 12 absorbed dose updated

Patient 13

(Breast, 2 scan)

Patient number	Scan	Scan length(mm)	CTDI volume (mGy)	D_{Eq} (mGy)	($CTDI_v$, D_{Eq}) (Diff %)
Patient 13	1	410	7.5	9.6	28%
	2	416	7.4	9.4	27%
Total			**14.9**	**19**	**28%**

Table 7. 13: Patient 13 absorbed dose updated

Patient 14

(Prostate, 3 scan)

Patient number	Scan	Scan length(mm)	CTDI volume (mGy)	D_{Eq} (mGy)	($CTDI_v$, D_{Eq}) (Diff %)
Patient 14	1	260	3	3.9	30%
	2	384	16.5	20.6	25%
	3	404	16.8	20.9	24%
Total			**36.3**	**45.4**	**25%**

Table 7. 14: Patient 14 absorbed dose updated

Patient 15

(Prostate, 3scan)

Patient number	Scan	Scan length(mm)	CTDI volume (mGy)	D_{Eq} (mGy)	$(CTDI_v, D_{Eq})$ (Diff %)
Patient 15	1	256	3.1	4	29%
	2	449	10.9	13.9	28%
	3	253	25.4	30.1	19%
Total			**39.4**	**48**	**22%**

Table 7. 15: Patient 15 absorbed dose updated

Patient 16

(Prostate, 4 scan)

Patient number	Scan	Scan length(mm)	CTDI volume (mGy)	D_{Eq} (mGy)	$(CTDI_v, D_{Eq})$ (Diff %)
Patient 16	1	264	2.9	3.8	31%
	2	450	9.8	12.5	28%
	3	254	2.9	3.7	28%
	4	443	9.5	12.2	28%
Total			**25.1**	**32.2**	**28%**

Table 7. 16: Patient 16 absorbed dose updated

Patient 17

(Anus, 2 scan)

Patient number	Scan	Scan length(mm)	CTDI volume (mGy)	D_{Eq} (mGy)	$(CTDI_v, D_{Eq})$ (Diff %)
Patient 17	1	447	9.6	12.3	28%
	2	339	9.2	11.6	26%
Total			**18.8**	**23.9**	**27%**

Table 7. 17: Patient 17 absorbed dose updated

Patient 18

(Breast, 2 scan)

Patient number	Scan	Scan length(mm)	CTDI volume (mGy)	D_{Eq} (mGy)	$(CTDI_v, D_{Eq})$ (Diff %)
Patient 18	1	405	8.3	10.6	27%
	2	429	8.5	10.8	27%
Total			**16.8**	**21.4**	**27%**

Table 7. 18: Patient 18 absorbed dose updated

Patient 19

(Breast, 2 scan)

Patient number	Scan	Scan length(mm)	CTDI volume (mGy)	D_{Eq} (mGy)	$(CTDI_v, D_{Eq})$ (Diff %)
Patient 19	1	361	14.7	18.4	25%
	2	384	14.7	18.4	25%
Total			**29.4**	**36.8**	**25%**

Table 7. 19: Patient 19 absorbed dose updated

Patient 20

(Breast, 1 scan)

Patient number	Scan	Scan length(mm)	CTDI volume (mGy)	D_{Eq} (mGy)	$(CTDI_v, D_{Eq})$ (Diff %)
Patient 20	1	447	18.2	22.8	25%
Total			**18.2**	**22.8**	**25%**

Table 7. 20: Patient 20 absorbed dose updated

Effective Dose for all patients

Patient 1

(Prostate , 3 scan)

Organs	WT	Organ dose (CTDI)	Contribution to effective dose (CTDI)	Organ dose (D_{Eq})	Contribution to effective dose (D_{Eq})
Scan 1 (254 mm)					
Gonads	0.08	2.8	0.2	3.7	0.3
Bladder	0.04	3.5	0.1	4.5	0.2
Prostate	0.00923	3.5	0.03	4.5	0.04
Colon	0.12	0.87	0.1	1.1	0.1
Spleen	0.00923	0.0045	0.00004	0.0058	0.0001
Kidney	0.00923	0.012	0.0001	0.015	0.0001
Pancreas	0.00923	0.0056	0.0001	0.073	0.001
Effective dose			**0.4**		**0.6**
Scan 2 (420 mm)					
Gonads	0.08	18	1.4	23	1.7
Bladder	0.04	20	0.8	25	1
Prostate	0.00923	20	0.2	25	0.2
Colon	0.12	15	1.8	19	2.3
Spleen	0.00923	0.76	0.01	0.96	0.01
Kidney	0.00923	1.9	0.02	2.5	0.02
Pancreas	0.00923	0.8	0.01	1	0.01
Effective dose			**4.2**		**5.2**
Scan 3 (359 mm)					
Gonads	0.08	15	1.2	20	1.6
Bladder	0.04	17	0.7	22	0.9
Prostate	0.00923	17	0.2	22	0.2
Colon	0.12	8.2	0.9	10	1.2
Spleen	0.00923	0.17	0.001	0.21	0.002
Kidney	0.00923	0.41	0.003	0.51	0.005
Pancreas	0.00923	0.2	0.002	0.25	0.002
Effective dose			**3**		**4**
Total scans			**7.6**		**9.8**

Table 7. 21: Patient 1 effective dose updated

Patient 2

(Rectum , 2 scan)

Organs	WT	Organ dose (CTDI)	Contribution to effective dose (CTDI)	Organ dose (D_{Eq})	Contribution to Effective Dose (D_{Eq})
Scan 1 (446 mm)					
Gonads	0.08	38	3	47	3.7
Bladder	0.04	42	1.7	52	2.1
Prostate	0.00923	42	0.4	52	0.5
Colon	0.12	32	3.8	40	4.8
Spleen	0.00923	2.5	0.02	3.1	0.02
Kidney	0.00923	8.1	0.1	10	0.1
Pancreas	0.00923	2.5	0.02	3.1	0.02
Effective dose			**9**		**11.2**
Scan 2 (449 mm)					
Gonads	0.08	35	2.8	44	3.5
Bladder	0.04	38	1.5	48	1.9
Prostate	0.00923	38	0.4	48	0.4
Colon	0.12	31	3.7	38	4.6
Spleen	0.00923	2.8	0.03	3.6	0.03
Kidney	0.00923	11	0.1	13	0.1
Pancreas	0.00923	2.8	0.03	3.5	0.03
Effective dose			**8.6**		**10.6**
Total scans			**17.6**		**21.8**

Table 7. 22: Patient 2 effective dose updated

Patient 3

(Breast , 2 scan)

Organs	WT	Organ dose (CTDI)	Contribution to effective dose (CTDI)	Organ dose (D_{Eq})	Contribution to effective dose (D_{Eq})
Scan 1 (424mm)					
Lung	0.12	12	1.4	16	1.9
Liver	0.04	8.7	0.3	11	0.4
Breast	0.12	9.7	1.2	12	1.4
Stomach	0.12	7.6	0.9	9.8	1.2
Oesophagus	0.04	14	0.6	18	0.7
Heart	0.00923	13	0.1	16	0.2
Effective dose			**4.5**		**5.8**
Scan 2 (390 mm)					
Lung	0.12	13	1.6	16	1.9
Liver	0.04	7.1	0.3	8.9	0.4
Breast	0.12	9.9	1.2	13	1.6
Stomach	0.12	5.4	0.7	6.8	0.8
Oesophagus	0.04	15	0.6	18	0.7
Heart	0.00923	13	0.1	16	0.2
Effective dose			**4.5**		**5.6**
Total scans			**9**		**11.4**

Table 7. 23: Patient 3 effective dose updated

Patient 4

(Prostate , 4 scan)

Organs	WT	Organ dose (CTDI)	Contribution to effective dose (CTDI)	Organ dose (D_{Eq})	Contribution to effective dose (D_{Eq})
Scan 1 (269 mm)					
Gonads	0.08	2.9	0.2	3.7	0.3
Bladder	0.04	4	0.2	5.2	0.2
Prostate	0.00923	4	0.04	5.2	0.1
Colon	0.12	1	0.1	1.3	0.2
Spleen	0.00923	0.0068	0.0001	0.0088	0.0001
Kidney	0.00923	0.017	0.0002	0.022	0.0002
Pancreas	0.00923	0.0081	0.0001	0.011	0.0001
Effective dose			**0.5**		**0.8**
Scan 2 (252 mm)					
Gonads	0.08	5.8	0.5	7.3	0.6
Bladder	0.04	7.1	0.3	8.9	0.4
Prostate	0.00923	7.1	0.1	8.9	0.1
Colon	0.12	1.8	0.2	2.2	0.3
Spleen	0.00923	0.0091	0.0001	0.011	0.0001
Kidney	0.00923	0.023	0.0002	0.03	0.0003
Pancreas	0.00923	0.011	0.0001	0.014	0.0001
Effective dose			**1.1**		**1.4**
Scan 3(407 mm)					
Gonads	0.08	35	2.8	44	3.5
Bladder	0.04	39	1.6	48	1.9
Prostate	0.00923	39	0.4	48	0.44
Colon	0.12	27	3.2	33	3.9
Spleen	0.00923	1.2	0.01	1.5	0.01
Kidney	0.00923	2.9	0.03	3.6	0.03
Pancreas	0.00923	1.2	0.01	1.5	0.01
Effective dose			**8.1**		**9.8**
Scan 4 (436 mm)					
Gonads	0.08	15	1.2	20	1.6
Bladder	0.04	17	0.7	22	0.9
Prostate	0.00923	17	0.2	22	0.2
Colon	0.12	13	1.6	17	2
Spleen	0.00923	1	0.01	1.3	0.01
Kidney	0.00923	3.3	0.03	4.2	0.04
Pancreas	0.00923	1	0.01	1.3	0.01
Effective dose			**3.7**		**4.7**
Total scans			**13.4**		**16.7**

Table 7. 24: Patient 4 effective dose updated

Patient 5

(Breast , 2 scan)

Organs	WT	Organ dose (CTDI)	Contribution to effective dose (CTDI)	Organ dose (D_{Eq})	Contribution to effective dose (D_{Eq})
			Scan 1 (447 mm)		
Lung	0.12	12	1.4	15	1.8
Liver	0.04	9.5	0.4	12	0.5
Breast	0.12	9.1	1.1	12	1.4
Stomach	0.12	9.3	1.1	12	1.4
Oesophagus	0.04	13	0.5	17	0.7
Heart	0.00923	12	0.1	15	0.1
Effective dose			**4.6**		**5.9**
			Scan 2 (423 mm)		
Lung	0.12	12	1.4	15	1.8
Liver	0.04	8.3	0.3	11	0.4
Breast	0.12	9.2	1.1	12	1.4
Stomach	0.12	7.3	0.9	9.3	1.1
Oesophagus	0.04	13	0.5	17	0.7
Heart	0.00923	12	0.1	15	0.1
Effective dose			**4.3**		**5.5**
Total scans			**8.9**		**11.4**

Table 7. 25: Patient 5 effective dose updated

Patient 6

(Pelvis , 2 scan)

Organs	WT	Organ dose (CTDI)	Contribution to effective dose (CTDI)	Organ dose (D_{Eq})	Contribution to effective dose (D_{Eq})
		Scan 1 (254 mm)			
Gonads	0.08	17	1.4	21	1.7
Bladder	0.04	23	0.9	28	1.1
Prostate	0.00923	23	0.2	28	0.3
Colon	0.12	5.6	0.7	6.8	0.8
Spleen	0.00923	0.033	0.0003	0.039	0.0004
Kidney	0.00923	0.083	0.001	0.1	0.001
Pancreas	0.00923	0.038	0.0004	0.046	0.0004
Effective dose			**3.2**		**4**
		Scan 2 (386 mm)			
Gonads	0.08	13	1	17	1.4
Bladder	0.04	15	0.6	19	0.8
Prostate	0.00923	15	0.1	19	0.2
Colon	0.12	8.6	1	11	1
Spleen	0.00923	0.28	0.003	0.36	0.003
Kidney	0.00923	0.68	0.01	0.86	0.01
Pancreas	0.00923	0.3	0.003	0.38	0.004
Effective dose			**2.7**		**3.4**
Total scans			**5.9**		**7.4**

Table 7. 26: Patient 6 effective dose updated

Patient 7

(Pelvis, 2 scan)

Organs	WT	Organ dose (CTDI)	Contribution to effective dose (CTDI)	Organ dose (D_{Eq})	Contribution to effective dose (D_{Eq})
			Scan 1 (449 mm)		
Gonads	0.08	25	2	31	2.5
Bladder	0.04	27	1.1	34	1.4
Prostate	0.00923	27	0.2	34	0.3
Colon	0.12	22	2.6	27	3.2
Spleen	0.00923	2	0.02	2.5	0.02
Kidney	0.00923	7.4	0.1	9.3	0.1
Pancreas	0.00923	2	0.02	2.5	0.02
Effective dose			**6**		**7.5**
			Scan 2 (380 mm)		
Gonads	0.08	22	1.8	28	2.2
Bladder	0.04	25	1	31	1.2
Prostate	0.00923	25	0.2	31	0.3
Colon	0.12	14	1.7	17	2.04
Spleen	0.00923	0.38	0.004	0.47	0.004
Kidney	0.00923	0.91	0.01	1.1	0.01
Pancreas	0.00923	0.41	0.004	0.51	0.005
Effective dose			**4.7**		**5.8**
Total scans			**10.7**		**13.3**

Table 7. 27: Patient 7 effective dose updated

Patient 8

(Breast, 2 scan)

Organs	WT	Organ dose (CTDI)	Contribution to effective dose (CTDI)	Organ dose (D_{Eq})	Contribution to effective dose (D_{Eq})
			Scan 1 (401 mm)		
Lung	0.12	15	1.8	18	2.2
Liver	0.04	9	0.4	11	0.4
Breast	0.12	11	1.3	14	1.7
Stomach	0.12	7.1	0.9	9	1.1
Oesophagus	0.04	17	0.7	21	0.8
Heart	0.00923	15	0.1	19	0.2
Effective dose			**5.2**		**6.4**
			Scan 2 (381 mm)		
Lung	0.12	15	1.8	19	2.3
Liver	0.04	7.5	0.3	9.6	0.4
Breast	0.12	12	1.4	15	1.8
Stomach	0.12	5.4	0.6	6.9	0.8
Oesophagus	0.04	17	0.7	22	0.9
Heart	0.00923	15	0.1	19	0.2
Effective dose			**4.9**		**6.4**
Total scans			**10.1**		**12.8**

Table 7. 28: Patient 8 effective dose updated

Patient 9 (Breast, 1 scan)

Organs	WT	Organ dose (CTDI)	Contribution to effective dose (CTDI)	Organ dose (D_{Eq})	Contribution to effective dose (D_{Eq})
		Scan 1 (391 mm)			
Lung	0.12	24	2.9	31	3.7
Liver	0.04	14	0.6	17	0.7
Breast	0.12	19	2.3	24	2.9
Stomach	0.12	10	1.2	13	1.6
Oesophagus	0.04	28	1.1	36	1.4
Heart	0.00923	25	0.2	31	0.3
Effective dose			**8.3**		**10.6**
Total scans			**8.3**		**10.6**

Table 7. 29: Patient 9 effective dose updated

Patient 10 (Breast, 2 scan)

Organs	WT	Organ dose (CTDI)	Contribution to effective dose (CTDI)	Organ dose (D_{Eq})	Contribution to effective dose (D_{Eq})
		Scan 1 (450 mm)			
Lung	0.12	33	3.9	41	4.9
Liver	0.04	19	0.8	24	0.9
Breast	0.12	25	3	31	3.7
Stomach	0.12	15	1.8	19	2.3
Oesophagus	0.04	37	1.5	47	1.8
Heart	0.00923	33	0.3	41	0.4
Effective dose			**11.3**		**14**
		Scan 2 (432 mm)			
Lung	0.12	30	3.6	38	4.6
Liver	0.04	23	0.9	28	1.1
Breast	0.12	24	2.8	30	3.6
Stomach	0.12	21	2.5	26	3.1
Oesophagus	0.04	35	1.4	43	1.7
Heart	0.00923	31	0.3	39	0.4
Effective dose			**11.5**		**14.5**
Total scans			**22.8**		**28.5**

Table 7. 30: Patient 10 effective dose updated

Patient 11

(Pancreas , 2 scan)

Organs	WT	Organ dose (CTDI)	Contribution to effective dose (CTDI)	Organ dose (D_{Eq})	Contribution to effective dose (D_{Eq})
			Scan 1 (445 mm)		
Gonads	0.08	5.2	0.4	6.6	0.5
Bladder	0.04	4.5	0.2	5.8	0.2
Prostate	0.00923	4.5	0.04	5.8	0.1
Colon	0.12	9.9	1.2	13	1.3
Spleen	0.00923	12	0.1	15	0.1
Kidney	0.00923	15	0.1	19	0.2
Pancreas	0.00923	11	0.1	14	0.1
Effective dose			**2.1**		**2.2**
			Scan 2 (380 mm)		
Gonads	0.08	0.85	0.1	1.1	0.1
Bladder	0.04	0.4	0.01	0.51	0.02
Prostate	0.00923	0.4	0.004	0.51	0.01
Colon	0.12	6.2	0.7	7.8	0.8
Spleen	0.00923	12	0.1	15	0.1
Kidney	0.00923	15	0.1	18	0.2
Pancreas	0.00923	11	0.1	14	0.1
Effective dose			**1.1**		**2**
Total scans			**3.2**		**4.2**

Table 7. 31: Patient 11 effective dose updated

Patient 12

(Prostate , 4 scan)

Organs	WT	Organ dose (CTDI)	Contribution to effective dose (CTDI)	Organ dose (D_{Eq})	Contribution to effective dose (D_{Eq})
Scan 1 (258 mm)					
Gonads	0.08	2.9	0.2	3.8	0.3
Bladder	0.04	3.9	0.2	5.1	0.2
Prostate	0.00923	3.9	0.04	5.1	0.1
Colon	0.12	0.69	0.1	1.3	0.2
Spleen	0.00923	0.0055	0.0001	0.0072	0.0001
Kidney	0.00923	0.014	0.0001	0.018	0.0002
Pancreas	0.00923	0.0065	0.0001	0.0085	0.0001
Effective dose			**0.5**		**0.8**
Scan 2 (256 mm)					
Gonads	0.08	2.9	0.2	3.9	0.3
Bladder	0.04	3.7	0.2	5	0.2
Prostate	0.00923	3.7	0.04	5	0.1
Colon	0.12	0.92	0.1	1.2	0.1
Spleen	0.00923	0.005	0.0001	0.006	0.0001
Kidney	0.00923	0.013	0.0001	0.017	0.0002
Pancreas	0.00923	0.006	0.0001	0.008	0.0001
Effective dose			**0.5**		**0.7**
Scan 3 (392 mm)					
Gonads	0.08	15	1.2	18	1.4
Bladder	0.04	16	0.6	20	0.8
Prostate	0.00923	16	0.2	20	0.2
Colon	0.12	9.4	1.1	12	1.4
Spleen	0.00923	0.31	0.003	0.39	0.004
Kidney	0.00923	0.75	0.01	0.95	0.01
Pancreas	0.00923	0.33	0.003	0.42	0.004
Effective dose			**3.1**		**3.8**
Scan 4 (385 mm)					
Gonads	0.08	14	1.1	18	1.4
Bladder	0.04	15	0.6	19	0.8
Prostate	0.00923	15	0.1	19	0.2
Colon	0.12	8.7	1	11	1.3
Spleen	0.00923	0.26	0.002	0.33	0.003
Kidney	0.00923	0.63	0.01	0.81	0.01
Pancreas	0.00923	0.28	0.003	0.36	0.003
Effective dose			**2.8**		**3.7**
Total scans			**6.9**		**9**

Table 7. 32: Patient 12 effective dose updated

Patient 13

(Breast, 2 scan)

Organs	WT	Organ dose (CTDI)	Contribution to effective dose (CTDI)	Organ dose (D_{Eq})	Contribution to effective dose (D_{Eq})
			Scan 1 (410 mm)		
Lung	0.12	12	1.4	15	1.8
Liver	0.04	7.7	0.3	9.8	0.4
Breast	0.12	9.2	1.1	12	1.4
Stomach	0.12	6.5	0.8	8.3	0.9
Oesophagus	0.04	13	0.5	17	0.7
Heart	0.00923	12	0.1	15	0.1
Effective dose			**4.2**		**5.3**
			Scan 2 (416 mm)		
Lung	0.12	12	1.4	15	1.8
Liver	0.04	8.2	0.3	10	0.4
Breast	0.12	9.1	1.1	12	1.4
Stomach	0.12	7.2	0.9	9.1	1.1
Oesophagus	0.04	13	0.5	17	0.7
Heart	0.00923	12	0.1	15	0.1
Effective dose			**4.3**		**5.5**
Total scans			**8.5**		**10.8**

Table 7. 33: Patient 13 effective dose updated

Patient 14

(Prostate , 3 scan)

Organs	WT	Organ dose (CTDI)	Contribution to effective dose (CTDI)	Organ dose (D_{Eq})	Contribution to effective dose (D_{Eq})
Scan 1 (260 mm)					
Gonads	0.08	2.9	0.2	3.7	0.3
Bladder	0.04	3.8	0.2	5	0.2
Prostate	0.00923	3.8	0.03	5	0.1
Colon	0.12	0.94	0.1	1.2	0.1
Spleen	0.00923	0.0054	0.0001	0.0071	0.0001
Kidney	0.00923	0.014	0.0001	0.018	0.0002
Pancreas	0.00923	0.0063	0.0001	0.0083	0.0001
Effective dose			**0.5**		**0.7**
Scan 2 (384 mm)					
Gonads	0.08	24	1.9	30	2.4
Bladder	0.04	26	1	33	1.3
Prostate	0.00923	26	0.2	33	0.3
Colon	0.12	14	1.7	18	2.2
Spleen	0.00923	0.4	0.004	0.5	0.01
Kidney	0.00923	0.98	0.01	1.2	0.01
Pancreas	0.00923	0.44	0.004	0.55	0.01
Effective dose			**4.8**		**6.2**
Scan 3 (404 mm)					
Gonads	0.08	25	2	31	2.5
Bladder	0.04	27	1.1	34	1.4
Prostate	0.00923	27	0.3	34	0.3
Colon	0.12	17	2	22	2.6
Spleen	0.00923	0.65	0.01	0.8	0.01
Kidney	0.00923	1.6	0.01	2	0.02
Pancreas	0.00923	0.69	0.01	0.87	0.01
Total			**5.4**		**6.8**
Total scans			**10.7**		**13.7**

Table 7. 34: Patient 14 effective dose updated

Patient 15

(Prostate , 3 scan)

Organs	WT	Organ dose (CTDI)	Contribution to effective dose (CTDI)	Organ dose (D_{Eq})	Contribution to effective dose (D_{Eq})
Scan 1 (256 mm)					
Gonads	0.08	2.9	0.2	3.8	0.3
Bladder	0.04	3.9	0.2	5.1	0.2
Prostate	0.00923	3.9	0.04	5.1	0.1
Colon	0.12	0.96	0.1	1.3	0.2
Spleen	0.00923	0.0055	0.0001	0.0072	0.0001
Kidney	0.00923	0.014	0.0001	0.018	0.0002
Pancreas	0.00923	0.0065	0.0001	0.0085	0.0001
Effective dose			**0.5**		**0.8**
Scan 2 (449 mm)					
Gonads	0.08	16	1.3	21	1.7
Bladder	0.04	18	0.7	23	0.9
Prostate	0.00923	18	0.2	23	0.2
Colon	0.12	14	1.7	18	2.2
Spleen	0.00923	1.3	0.01	1.7	0.02
Kidney	0.00923	4.8	0.04	6.2	0.1
Pancreas	0.00923	1.3	0.01	1.7	0.02
Effective dose			**4**		**5.1**
Scan 3 (253 mm)					
Gonads	0.08	23	1.8	28	2.2
Bladder	0.04	29	1.2	34	1.4
Prostate	0.00923	29	0.3	34	0.3
Colon	0.12	7.2	0.9	8.6	1.03
Spleen	0.00923	0.037	0.0003	0.044	0.0004
Kidney	0.00923	0.096	0.001	0.11	0.001
Pancreas	0.00923	0.046	0.0004	0.055	0.001
Effective dose			**4.2**		**5**
Total scans			**8.7**		**10.9**

Table 7. 35: Patient 15 effective dose updated

Patient 16

(Prostate , 4 scan)

Organs	WT	Organ dose (CTDI)	Contribution to effective dose (CTDI)	Organ dose (D_{Eq})	Contribution to effective dose (D_{Eq})
Scan 1(264 mm)					
Gonads	0.08	2.8	0.2	3.6	0.3
Bladder	0.04	3.8	0.2	4.9	0.2
Prostate	0.00923	3.8	0.03	4.9	0.1
Colon	0.12	0.92	0.1	1.2	0.1
Spleen	0.00923	0.0053	0.0001	0.0069	0.0001
Kidney	0.00923	0.014	0.0001	0.018	0.0002
Pancreas	0.00923	0.0062	0.0001	0.008	0.0001
Effective dose			**0.5**		**0.7**
Scan 2 (450 mm)					
Gonads	0.08	15	1.2	19	1.5
Bladder	0.04	16	0.6	20	0.8
Prostate	0.00923	16	0.2	20	0.2
Colon	0.12	13	1.6	16	1.9
Spleen	0.00923	1.2	0.01	1.5	0.01
Kidney	0.00923	4.4	0.04	5.6	0.1
Pancreas	0.00923	1.2	0.01	1.5	0.01
Effective dose			**3.7**		**4.5**
Scan 3 (254 mm)					
Gonads	0.08	2.7	0.2	3.4	0.3
Bladder	0.04	3.3	0.1	4.2	0.2
Prostate	0.00923	3.3	0.03	4.2	0.04
Colon	0.12	0.83	0.1	1.1	0.1
Spleen	0.00923	0.0043	0.00004	0.0055	0.0001
Kidney	0.00923	0.011	0.0001	0.014	0.0001
Pancreas	0.00923	0.0053	0.0001	0.0068	0.0001
Effective dose			**0.4**		**0.6**
Scan (443 mm)					
Gonads	0.08	14	1.1	18	1.4
Bladder	0.04	15	0.6	20	0.8
Prostate	0.00923	15	0.1	20	0.2
Colon	0.12	12	1.4	15	1.8
Spleen	0.00923	0.91	0.01	1.2	0.01
Kidney	0.00923	3	0.03	3.9	0.04
Pancreas	0.00923	0.93	0.01	1.2	0.01
Effective dose			**3.3**		**4.3**
Total scans			**7.9**		**10.1**

Table 7. 36: Patient 16 effective dose updated

Patient 17

(Anus , 2 scan)

Organs	WT	Organ dose (CTDI)	Contribution to effective dose (CTDI)	Organ dose (D_{Eq})	Contribution to effective dose (D_{Eq})
			Scan 1 (447 mm)		
Gonads	0.08	14	1.1	18	1.4
Bladder	0.04	16	0.6	20	0.8
Prostate	0.00923	16	0.2	20	0.2
Colon	0.12	12	1.4	16	1.9
Spleen	0.00923	1.1	0.01	1.5	0.01
Kidney	0.00923	4.3	0.04	5.5	0.1
Pancreas	0.00923	1.1	0.01	1.5	0.01
Effective dose			**3.4**		**4.4**
			Scan 2 (339 mm)		
Gonads	0.08	13	1	16	1.3
Bladder	0.04	14	0.6	18	0.7
Prostate	0.00923	14	0.1	18	0.2
Colon	0.12	5.9	0.7	7.5	0.9
Spleen	0.00923	0.093	0.001	0.12	0.001
Kidney	0.00923	0.22	0.002	0.28	0.003
Pancreas	0.00923	0.11	0.001	0.14	0.001
Effective dose			**2.4**		**3.1**
Total scans			**5.8**		**7.5**

Table 7. 37: Patient 17 effective dose updated

Patient 18

(Breast, 2 scan)

Organs	WT	Organ dose (CTDI)	Contribution to effective dose (CTDI)	Organ dose (D_{Eq})	Contribution to effective dose (D_{Eq})
Scan 1 (405 mm)					
Lung	0.12	13	1.6	17	2
Liver	0.04	8.5	0.3	11	0.4
Breast	0.12	10	1.2	13	1.6
Stomach	0.12	7.2	0.9	9.2	1.1
Oesophagus	0.04	15	0.6	19	0.8
Heart	0.00923	13	0.1	17	0.2
Effective dose			**4.7**		**6.1**
Scan 2 (429 mm)					
Lung	0.12	13	1.6	17	2
Liver	0.04	9.9	0.4	13	0.5
Breast	0.12	10	1.2	13	1.6
Stomach	0.12	9.1	1.1	11	1.3
Oesophagus	0.04	15	0.6	19	0.8
Heart	0.00923	14	0.1	17	0.2
Effective dose			**5**		**6.4**
Total scans			**9.7**		**12.5**

Table 7. 38: Patient 18 effective dose updated

Patient 19 (Breast, 2 scan)

Organs	WT	Organ dose (CTDI)	Contribution to effective dose (CTDI)	Organ dose (D_{Eq})	Contribution to effective dose (D_{Eq})
Scan 1 (361 mm)					
Lung	0.12	22	2.6	28	3.4
Liver	0.04	8.7	0.4	11	0.4
Breast	0.12	18	2.2	22	2.6
Stomach	0.12	5.6	0.7	7.1	0.9
Oesophagus	0.04	26	1	33	1.3
Heart	0.00923	23	0.2	29	0.3
Effective dose			**7.1**		**8.9**
Scan 2 (384 mm)					
Lung	0.12	23	2.8	28	3.4
Liver	0.04	12	0.5	14	0.6
Breast	0.12	18	2.2	22	2.6
Stomach	0.12	8.3	0.9	10	1.2
Oesophagus	0.04	26	1	33	1.3
Heart	0.00923	23	0.2	29	0.3
Effective dose			**7.6**		**9.4**
Total scans			**14.7**		**18.3**

Table 7. 39: Patient 19 effective dose updated

Patient 20 (Breast, 1 scan)

Organs	WT	Organ dose (CTDI)	Contribution to effective dose (CTDI)	Organ dose (D_{Eq})	Contribution to effective dose (D_{Eq})
Scan 1 (447 mm)					
Lung	0.12	29	3.5	36	4.3
Liver	0.04	23	0.9	29	1.2
Breast	0.12	22	2.6	28	3.4
Stomach	0.12	23	2.8	28	3.4
Oesophagus	0.04	33	1.3	41	1.6
Heart	0.00923	29	0.3	37	0.3
Effective dose			**11.4**		**14.2**
Total scans			**11.4**		**14.2**

Table 7. 40: Patient 20 effective dose updated

Appendix 3

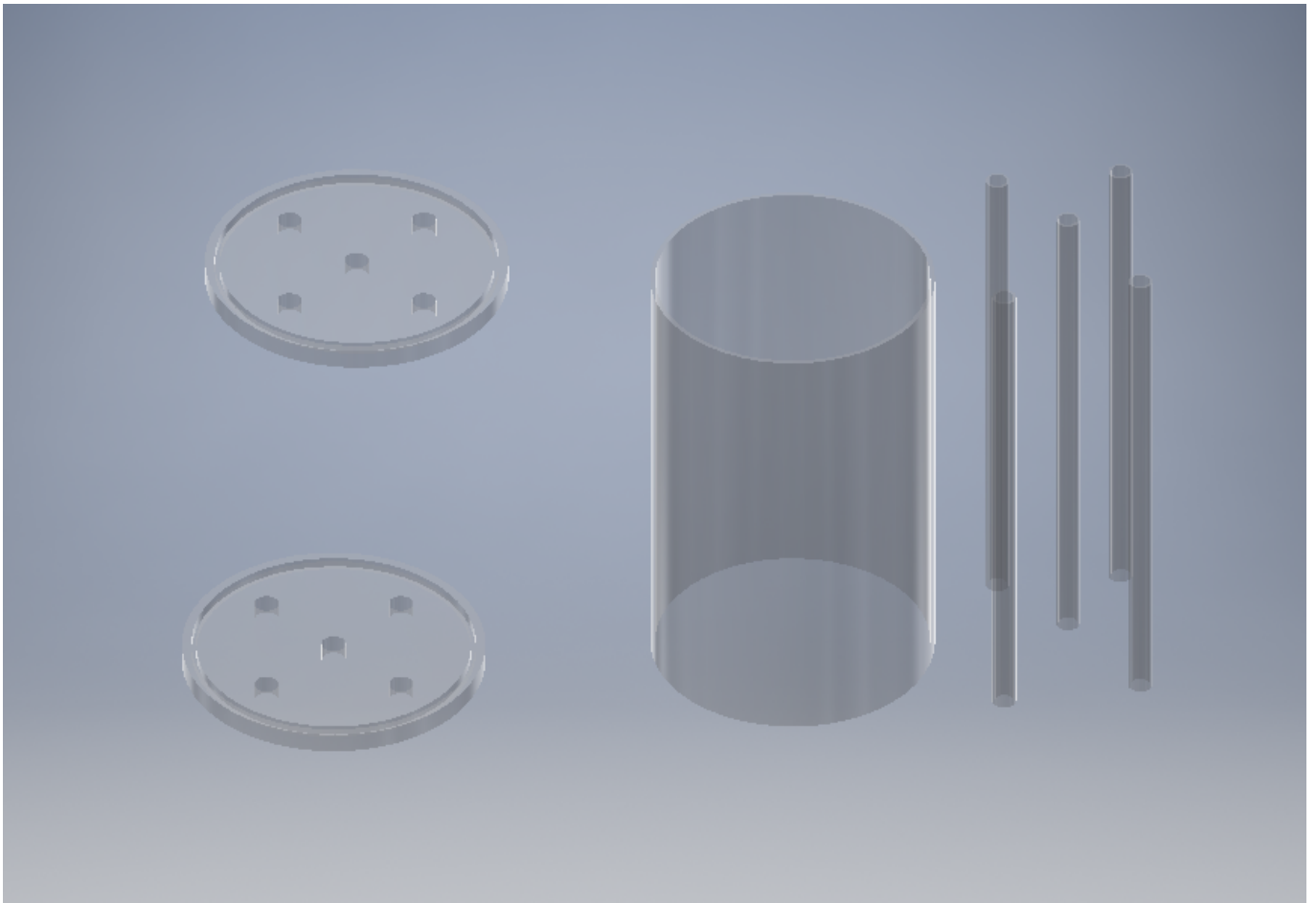**Dose Equilibrium phantom design (cut drawing)**

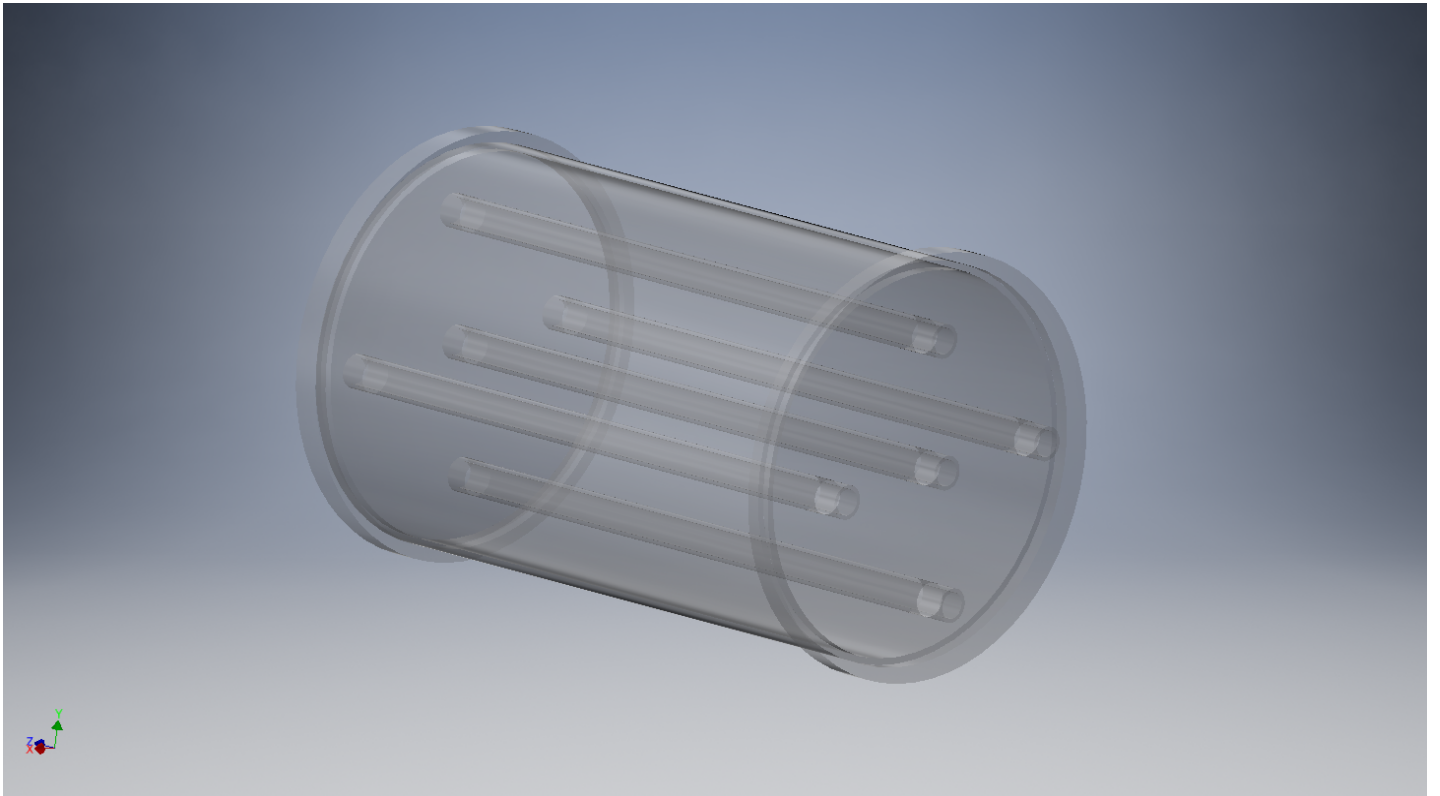*Figure 7. 2: Schematic image of all parts of the D_{Eq} phantom separately*

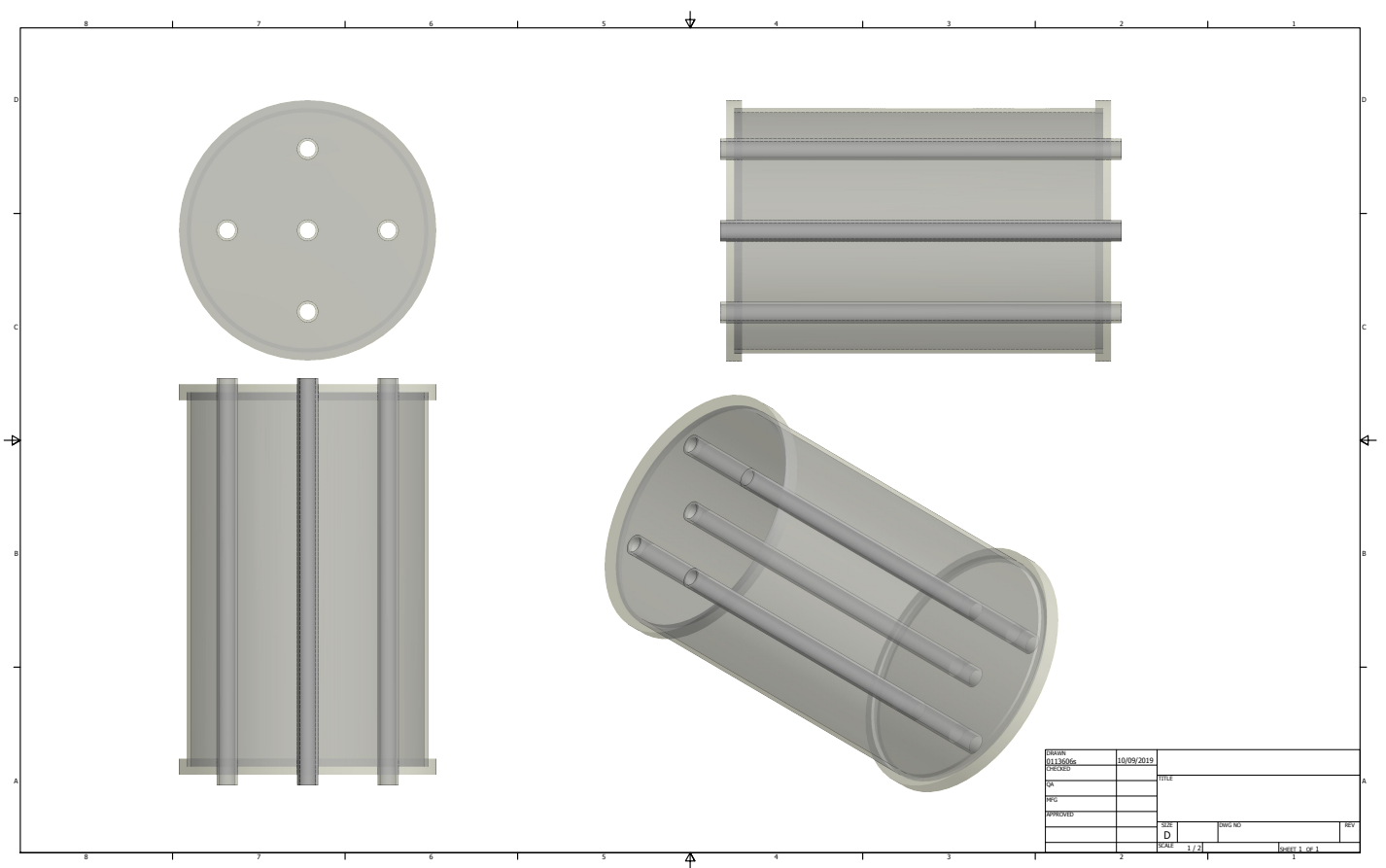*Figure 7. 3: Shematic image of all parts of the D_{Eq} phantom together*

Figure 7. 4: Schematic image of all parts of the D$_{Eq}$ phantom together from different angles

References

1.   Introduction to Dosimetry,Canadian Nuclear Safety Commission (CNSC). Ottawa; 2012.

2.   Schauer DA, Linton OW. NCRP report No.160, Ionizing Radiation Exposure of the Population of the United States, Medical Exposure-are we doing less with more, and is there a role for health physicists? Health Phys. 2009;97(1):1-5. doi:10.1097/01.HP.0000356672.44380.b7

3.   Boone JM, Brink JA, Edyvean S, et al. ICRU Report No. 87: Radiation dose and image-quality assessment in computed tomography. J ICRU. 2012;12(1):1-1. doi:10.1093/jicru/ndt007

4.   Radiation Doses Received by the Irish Population,Radiological Protection Institute of Ireland.; 2014.

5.   Dixon RL. A new look at CT dose measurement: Beyond CTDI. Med Phys. 2003;30(6):1272-1280. doi:10.1118/1.1576952

6.   Brenner DJ, McCollough CH, Orton CG. It is time to retire the computed tomography dose index (CTDI) for CT quality assurance and dose optimization. Med Phys. 2006;33(5):1189-1191. doi:10.1118/1.2173933

7.   Stern SH. NATIONWIDE EVALUATION OF X-RAY TRENDS (NEXT) TABULATION AND GRAPHICAL SUMMARY OF 2000 SURVEY OF COMPUTED TOMOGRAPHY. Frankfort; 2007. www.crcpd.org. Accessed August 9, 2019.

8.   Boone JM. The trouble with CTDI100. Med Phys. 2007;34(4):1364-1371. doi:10.1118/1.2713240

9.   Dixon RL. A new look at CT dose measurement: Beyond CTDI. Med Phys.

2003;30(6):1272-1280. doi:10.1118/1.1576952

10.   Comprehensive Methodology for the Evaluation of Radiation Dose in X-Ray
        Computed Tomography Report of AAPM Task Group 111: The Future of CT
        Dosimetry A New Measurement Paradigm Based on a Unified Theory for Axial,
        Helical, Fan-Beam, and Cone-Beam Scanning.; 2010.
        https://www.aapm.org/pubs/reports/rpt_111.pdf. Accessed April 11, 2019.

11.   Khan FM. The Physics of Radiation Therapy. Lippincott Williams & Wilkins; 2014.

12.   Parry RA, Glaze SA, Archer BR. The AAPM/RSNA Physics Tutorial for Residents.
        RadioGraphics. 1999;19(5):1289-1302. doi:10.1148/radiographics.19.5.g99se211289

13.   James R. Connolly. The Interaction of X-Rays with Matter and Radiation Safety.
        http://www.ehs.uiuc.edu/rss/xray/xrayintro.htm. Accessed August 9, 2019.

14.   Sandborg M. Computed Tomography: Physical principles and biohazards. Dep Radiat
        Phys Fac Heal Sci Linköping Univ Sweden. 1995. https://www.diva-
        portal.org/smash/get/diva2:327804/FULLTEXT01.pdf.

15.   Medical Image Characteristics and Quality Factors,sprawls educational foundation.
        http://www.sprawls.org/visuals/IMGCHAR/. Accessed June 12, 2020.

16.   CT scan, PhysicsCentral, American Physical Society Sites.
        https://www.physicscentral.com/explore/action/scans.cfm. Accessed June 12, 2020.

17.   Smith SW. The Scientist and Engineer's Guide to Digital Signal Processing.
        1997:pg423-450.

18.   Smith SW, Elsevier Science Publishers. Digital Signal Processing : A Practical Guide
        for Engineers and Scientists. Newnes; 2003.

19.   Brooks RA, Di Chiro G. Theory of Image Reconstruction in Computed Tomography.
        Radiology. 1975;117(3):561-572. doi:10.1148/117.3.561

20.   Bracewell RN, Riddle AC. Inversion of Fan-Beam Scans in Radio Astronomy.

Astrophys J. 1967;150:427. doi:10.1086/149346

21. Beister M, Kolditz D, Kalender WA. Iterative reconstruction methods in X-ray CT. Phys Medica. 2012;28(2):94-108. doi:10.1016/j.ejmp.2012.01.003

22. Beister M, Kolditz D, Kalender WA. Iterative reconstruction methods in X-ray CT. Phys Medica. 2012;28(2):94-108. doi:10.1016/J.EJMP.2012.01.003

23. Sznajder R. Kaczmarz Algorithm Revisited. 2015. doi:10.4467/2353737XCT.15.220.4425

24. Hounsfield GN. Computerized transverse axial scanning (tomography): Part 1. Description of system. Br J Radiol. 1973;46(552):1016-1022. doi:10.1259/0007-1285-46-552-1016

25. Gordon R, Bender R, Herman GT. Algebraic Reconstruction Techniques (ART) for three-dimensional electron microscopy and X-ray photography. J Theor Biol. 1970;29(3):471-481. doi:10.1016/0022-5193(70)90109-8

26. Bracewell R, N. R. Strip Integration in Radio Astronomy. Aust J Phys. 1956;9(2):198. doi:10.1071/PH560198

27. Gilbert P. Iterative methods for the three-dimensional reconstruction of an object from projections. J Theor Biol. 1972;36(1):105-117. doi:10.1016/0022-5193(72)90180-4

28. Computed Tomography , Radiology Key. https://radiologykey.com/computed-tomography-3/. Accessed August 23, 2019.

29. Bharath AA. Introductory Medical Imaging. Synth Lect Biomed Eng. 2008;3(1):1-186. doi:10.2200/S00165ED1V01Y200811BME026

30. Bushberg JT. The Essential Physics of Medical Imaging. Wolters Kluwer Health/Lippincott Williams & Wilkins; 2012.

31. Kalender WA. X-ray computed tomography. Phys Med Biol. 2006;51(13):R29-R43. doi:10.1088/0031-9155/51/13/R03

32. Kalender WA, Seissler W, Klotz E, Vock P. Spiral volumetric CT with single-breath-hold technique, continuous transport, and continuous scanner rotation. Radiology. 1990;176(1):181-183. doi:10.1148/radiology.176.1.2353088

33. Hu H. Multi-slice helical CT: Scan and reconstruction. Med Phys. 1999;26(1):5-18. doi:10.1118/1.598470

34. M. Prokop, M. Galanski, A. J. van der Molen CMS. Spiral and multislice computed tomography of the body. Clin Radiol. 2004;59(3):299. doi:10.1016/j.crad.2003.10.015

35. Curry TS, Dowdey JE, Murry RC, Christensen EE. Christensen's Physics of Diagnostic Radiology. Lea & Febiger; 1990.

36. Ketcham RA, Carlson WD. Acquisition, Optimization and Interpretation of X-Ray Computed Tomographic Imagery: Applications to the Geosciences. Vol 27.; 2001. http://citeseerx.ist.psu.edu/viewdoc/download?doi=10.1.1.330.3973&rep=rep1&type=pdf. Accessed August 9, 2019.

37. Goh YP, Lau KK, Low K, et al. Fine focal spot size improves image quality in computed tomography abdomen and pelvis. Eur Radiol. 2016;26(12):4545-4550. doi:10.1007/s00330-016-4313-7

38. Hsieh J. Computed Tomography : Principles, Design, Artifacts, and Recent Advances. SPIE Optical Engineering Press; 2003.

39. Seeram E. Computed Tomography : Physical Principles, Clinical Applications, and Quality Control. Saunders/Elsevier; 2009.

40. Schneider A, Feussner H, Schneider A, Feussner H. Diagnostic Procedures. Biomed Eng Gastrointest Surg. January 2017:87-220. doi:10.1016/B978-0-12-803230-5.00005-1

41. Multidetector Computed Tomography ,an overview ,ScienceDirect Topics. https://www.sciencedirect.com/topics/medicine-and-dentistry/multidetector-computed-

tomography. Accessed August 23, 2019.

42. Quality Assurance Programme for Computed Tomography: Diagnostic and Therapy Applications IAEA HUMAN HEALTH SERIES. VIENNA; 2012. http://www.iaea.org/Publications/index.html. Accessed April 11, 2019.

43. Quality Assurance in Diagnostic Radiology,WORLD HEALTH ORGANIZATION. Geneva; 1982.

44. Hendee WR, Ritenour ER. Medical Imaging Physics.; 2002.

45. Status of Computed Tomography Dosimetry for Wide Cone Beam Scanners, International Atomic Energy Agency IAEA. In: Vienna; 2011. http://www.iaea.org/Publications/index.html. Accessed April 11, 2019.

46. McCollough CH, Leng S, Yu L, Cody DD, Boone JM, McNitt-Gray MF. CT Dose Index and Patient Dose: They Are Not the Same Thing. Radiology. 2011;259(2):311-316. doi:10.1148/radiol.11101800

47. McCollough CH, Primak AN, Braun N, Kofler J, Yu L, Christner J. Strategies for reducing radiation dose in CT. Radiol Clin North Am. 2009;47(1):27-40. doi:10.1016/j.rcl.2008.10.006

48. Dixon RL, Ballard AC. Experimental validation of a versatile system of CT dosimetry using a conventional ion chamber: Beyond CTDI100. Med Phys. 2007;34(8):3399-3413. doi:10.1118/1.2757084

49. Descamps C, Gonzalez M, Garrigo E, Germanier A, Venencia D. Measurements of the dose delivered during CT exams using AAPM Task Group Report No. 111. J Appl Clin Med Phys. 2012;13(6):293-302. doi:10.1120/jacmp.v13i6.3934

50. Campelo MCS, Silva MC, Terini RA. CTDI versus New AAPM Metrics to assess Doses in CT: a case study. Brazilian J Radiat Sci. 2016;4(2). doi:10.15392/bjrs.v4i2.194

51. Tang K, Cui H, Fan H, Zhu H, Liu Z. Influence of sintering temperatures on LiF:Mg,Cu,P with various magnesium concentrations. Radiat Meas. 2014;69:7-11. doi:10.1016/j.radmeas.2014.07.016

52. Pagonis V, Kētēs G, Furetta C. Numerical and Practical Exercises in Thermoluminescence. Springer; 2006.

53. Tang K, Cui H, Zhu H, Fan Q. Study of a new Lif:Mg,Cu,P formulation with enhanced thermal stability and a lower residual TL signal. Radiat Meas. 2007;42(1):24-28. doi:10.1016/j.radmeas.2006.07.001

54. Ziying Z, Shoushan W, Fang W, Guolong C, Yuanfang L, Jianhuan Z. Measurement of Extremely Low Level Dose with LiF(Mg,Cu,P) TL Chips. Radiat Prot Dosimetry. 1986;17(1-4):415-418. doi:10.1093/oxfordjournals.rpd.a079850

55. Tang K. Thermal Loss and Recovery of Thermoluminescence Sensitivity in LiF:Mg,Cu,P. Radiat Prot Dosimetry. 2000;90(4):449-452. doi:10.1093/oxfordjournals.rpd.a033173

56. Meijvogel K, Bos AJJ. Influence of thermal treatments on glow curve and thermoluminescence emission spectra of LiF:Mg,Cu,P. Radiat Meas. 1995;24(3):239-247. doi:10.1016/1350-4487(95)00008-3

57. Horowitz Y, Moscovitch M. Invited Review Highlights and Pitfalls of 20 Years of Application of Computerised Glow Curve Analysis To Thermoluminscence Research And Dosimetry. Radiat Prot Dosimetry. 2013;153(1):1-22.

58. IAEA-TECDOC-897 Review of Data and Methods Recommended in the International Code of Practice IAEA Technical Reports Series No. 277, Absorbed Dose Determination in Photon and Electron Beams. VIENNA; 1992. https://www-pub.iaea.org/MTCD/publications/PDF/te_897_prn.pdf. Accessed April 15, 2019.

59. Li CL, Thakur Y, Ford NL. Comparison of the CTDI and AAPM report No. 111

methodology in adult, adolescent, and child head phantoms for MSCT and dental CBCT scanners. J Med Imaging. 2017;4(03):1. doi:10.1117/1.JMI.4.3.031212

60. Huda W, Mettler FA. Volume CT Dose Index and Dose-Length Product Displayed during CT: What Good Are They? Radiology. 2011;258(1):236-242. doi:10.1148/radiol.10100297

61. Paschoal CMM, Ferreira FCL, Souza DN, Santos LAP. Comparison of dose measurements in CT using a photodiode and a small ion chamber. Radiat Meas. 2016;91:50-53. doi:10.1016/J.RADMEAS.2016.05.002

62. Dixon RL. Restructuring CT dosimetry-A realistic strategy for the future Requiem for the pencil chamber. Med Phys. 2006;33(10):3973-3976. doi:10.1118/1.2336504

63. Matsubara K. Computed Tomography Dosimetry : From Basic to State-ofthe-art Techniques. 2017. https://www.semanticscholar.org/paper/Computed-Tomography-Dosimetry-%3A-From-Basic-to-Matsubara/72029a0920abaa6ae5b07cfe1b710d8006814125. Accessed April 11, 2019.

64. PC Electrometer™ - Sun Nuclear. https://www.sunnuclear.com/products/pc-electrometer. Accessed June 13, 2020.

65. Fearon T, Xie H, Cheng JY, Ning H, Zhuge Y, Miller RW. Patient-specific CT dosimetry calculation: a feasibility study. J Appl Clin Med Phys. 2011;12(4):196-209. doi:10.1120/jacmp.v12i4.3589

66. Zhou H, Boone JM. Monte Carlo evaluation of CTD(infinity) in infinitely long cylinders of water, polyethylene and PMMA with diameters from 10 mm to 500 mm. Med Phys. 2008;35(6):2424-2431. doi:10.1118/1.2921829

67. White DR. The formulation of tissue substitute materials using basic interaction data. Phys Med Biol. 1977;22(5):889-899. http://www.ncbi.nlm.nih.gov/pubmed/909925. Accessed April 11, 2019.

68. Particular Requirements for the Basic Safety and Essential Performance of X-Ray Equipment for Computed Tomography Committee Draft, International Electrotechnical Commission IEC, Amendment 1 to IEC 60601-2-44: 2009 Medical Electrical Equipment: Parts 2-44. Geneva; 2009. https://webstore.iec.ch/publication/2661. Accessed April 11, 2019.

69. Kalender W. Computed Tomography : Fundamentals, System Technology, Image Quality, Applications. Publicis Corporate Pub; 2011.

70. Alaraky R. Measurement of radiation dose for patients by CT scan and x-rays. October 2015. http://repository.sustech.edu/handle/123456789/11998?show=full. Accessed April 11, 2019.

71. Shope TB, Gagne RM, Johnson GC. A method for describing the doses delivered by transmission x-ray computed tomography. Med Phys. 1981;8(4):488-495. doi:10.1118/1.594995

72. Bakalyar D, Dm. A Critical Look at the Numerical Coefficients in CTDIVOL. Med Phys. 2006;33(6Part3):2003-2003. doi:10.1118/1.2240267

73. QADOS. Data Sheet for Harshaw TLD Model 3500 Materials and Assemblies.

74. Kalender WA. Dose in x-ray computed tomography. Phys Med Biol. 2014;59(3):R129-R150. doi:10.1088/0031-9155/59/3/R129

75. Brenner DJ, Elliston CD, Hall EJ, Berdon WE. Estimated Risks of Radiation-Induced Fatal Cancer from Pediatric CT. Am J Roentgenol. 2001;176(2):289-296. doi:10.2214/ajr.176.2.1760289

76. Mayo-Smith WW, Hara AK, Mahesh M, Sahani D V., Pavlicek W. How I Do It: Managing Radiation Dose in CT. Radiology. 2014;273(3):657-672. doi:10.1148/radiol.14132328

77. Managing Patient Dose in Computed Tomography Annals of International

Commission on Radiological Protection (ICRP) Publication 87. Published for the International Commission on Radiological Protection by Pergamon; 2000.

78.   Hidajat N, Mäurer J, Schröder RJ, et al. Relationships between physical dose quantities and patient dose in CT. Br J Radiol. 1999;72(858):556-561. doi:10.1259/bjr.72.858.10560337

79.   Hopper KD, Neuman JD, King SH, Kunselman AR. Radioprotection to the eye during CT scanning. AJNR Am J Neuroradiol. 22(6):1194-1198. http://www.ncbi.nlm.nih.gov/pubmed/11415918. Accessed April 11, 2019.

80.   Groves AM, Owen KE, Courtney HM, et al. 16-detector multislice CT: dosimetry estimation by TLD measurement compared with Monte Carlo simulation. Br J Radiol. 2004;77(920):662-665. doi:10.1259/bjr/48307881

81.   DeMarco JJ, Cagnon CH, Cody DD, et al. A Monte Carlo based method to estimate radiation dose from multidetector CT (MDCT): cylindrical and anthropomorphic phantoms. Phys Med Biol. 2005;50(17):3989-4004. doi:10.1088/0031-9155/50/17/005

82.   Akpochafor MO. Computed Tomography Organ dose determination using ImPACT simulation software: Our findings in South-West Nigeria. Eurasian J Med Oncol. 2018. doi:10.14744/ejmo.2017.75047

83.   Borras C, Cohen G, Jucius RA, et al. SPECIFICATION AND ACCEPTANCE TESTING OF COMPUTED TOMOGRAPHY SCANNERS Report of American Association of Physicists in Medicine AAPM Task Group 2 , Report No. 39. New York; 1993. https://www.aapm.org/pubs/reports/rpt_39.pdf. Accessed April 11, 2019.

84.   Recommendations of the International Commission on Radiological Protection, ICRP Publication 60.; 1990. http://www.icrp.org/publication.asp?id=icrp publication 60. Accessed April 11, 2019.

85.   The 2007 Recommendations of the International Commission on Radiological

Protection, ICRP Publication 103.; 2007.

86.   ImPACT Imaging Performance Assessments of CT. CT Patient Dosimetry
       Spreadsheet (version 1.0.4 27/05/2011). http://www.impactscan.org/. Accessed April
       11, 2019.

87.   Stamm G, Nagel HD. CT-expo--a novel program for dose evaluation in CT. RöFo -
       Fortschritte auf dem Gebiet der Röntgenstrahlen und der Bildgeb Verfahren.
       2002;174(12):1570-1576. doi:10.1055/s-2002-35937

88.   Tian X, Segars WP, Dixon RL, Samei E. Convolution-based estimation of organ dose
       in tube current modulated CT. Phys Med Biol. 2016;61(10):3935-3954.
       doi:10.1088/0031-9155/61/10/3935

89.   Shrimpton C, Jones G. NRPB-SR250 Normalised Organ Doses for X-Ray Computed
       Tomography Calculated Using Monte Carlo Techniques. London; 1991.
       https://webarchive.nationalarchives.gov.uk/20140714102318/http://www.hpa.org.uk/P
       ublications/Radiation/NPRBArchive/NRPBSoftware/. Accessed April 11, 2019.

90.   Albngali A, Shearer A, van der Putten W, Tuohy B, Colgan N. CT Output Dose
       Performance-Conventional Approach versus the Dose Equilibrium Method. Int J Med
       Physics, Clin Eng Radiat Oncol. 2018;07(01):15-26. doi:10.4236/ijmpcero.2018.71002

91.   The RANDO® phantom. The Phantom Laboratory. P.O. Box 511, Salem, NY 12865-
       0511 United States. https://www.phantomlab.com/contact. Accessed April 15, 2019.

92.   Alderson Radiation Therapy phantom (ART). Radiology Support Devices , Inc.
       http://pdf.medicalexpo.com/pdf/radiology-support-devices/alderson-radiation-therapy-
       phantom-art/97853-116993.html. Accessed April 15, 2019.

93.   Geleijns J, van Unnik JG, Zoetelief J, Zweers D, Broerse JJ. Comparison of two
       methods for assessing patient dose from computed tomography. Br J Radiol.
       1994;67(796):360-365. doi:10.1259/0007-1285-67-796-360

94. Shrimpton PC, Jones DG, Hillier MC, Wall BF, Le Heron JC, Faulkner K. Survey of CT Practice in the UK. Part 2: Dosimetric Aspects. London: National Radiological Protection Board; 1991.

95. Jessen KA, Shrimpton PC, Geleijns J, Panzer W, Tosi G. Dosimetry for optimisation of patient protection in computed tomography. Appl Radiat Isot. 1999;50(1):165-172. http://www.ncbi.nlm.nih.gov/pubmed/10028635. Accessed April 15, 2019.

96. Thomson JEM, Tingey DRC. Radiation doses from computed tomography in Australia. November 1997. https://inis.iaea.org/search/search.aspx?orig_q=RN:30003755. Accessed April 15, 2019.

97. Cakmak ED, Tuncel N, Sindir B, Cakmak ED, Tuncel N, Sindir B. Assessment of Organ Dose by Direct and Indirect Measurements for a Wide Bore X-Ray Computed Tomography Unit That Used in Radiotherapy. International Journal of Medical Physics, Clinical Engineering and Radiation Oncology. Int J Med Physics, Clin Eng Radiat Oncol. 2015;04(02):132-142. doi:10.4236/ijmpcero.2015.42017

98. Brenner DJ, Hall EJ. Computed Tomography — An Increasing Source of Radiation Exposure. N Engl J Med. 2007;357(22):2277-2284. doi:10.1056/NEJMra072149

99. Mathews JD, Forsythe A V, Brady Z, et al. Cancer risk in 680 000 people exposed to computed tomography scans in childhood or adolescence: Data linkage study of 11 million Australians. BMJ. 2013;346(7910):f2360. doi:10.1136/bmj.f2360

100. FDA. What are the Radiation Risks from CT ? Public Health. 2006:2005-2007. https://www.fda.gov/radiation-emitting-products/medical-x-ray-imaging/what-are-radiation-risks-ct. Accessed April 10, 2020.

101. Linet MS, Slovis TL, Miller DL, et al. Cancer risks associated with external radiation from diagnostic imaging procedures. CA Cancer J Clin. 2012;62(2):75-100.

doi:10.3322/caac.21132

102. Lin EC. Radiation risk from medical imaging. Mayo Clin Proc. 2010;85(12):1142-1146; quiz 1146. doi:10.4065/mcp.2010.0260

103. NCRP Report 160 | NCRP | Bethesda, MD. https://ncrponline.org/publications/reports/ncrp-report-160-2/. Accessed July 5, 2019.

104. AAPM Reports - The Measurement, Reporting, and Management of Radiation Dose in CT. https://www.aapm.org/pubs/reports/detail.asp?docid=97. Accessed July 5, 2019.